Correlation and Interference Experiments with Edge States

INAUGURALDISSERTATION
zur
Erlangung der Würde eines Doktors der Philosophie
vorgelegt der
Philosophisch-Naturwissenschaftlichen Fakultät
der Universität Basel
von

Erasmus Bieri

aus Luzern (LU)

Basel, 2009

Genehmigt von der Philosophisch-Naturwissenschaftlichen Fakultät
auf Antrag von:

Prof. Dr. C. Schönenberger
Prof. Dr. J. Faist
Prof. Dr. Ch. Strunk

Basel, den 18. September 2007

Prof. Dr. H.-P. Hauri, Dekan

creative commons

Namensnennung-Keine kommerzielle Nutzung-Keine Bearbeitung 2.5 Schweiz

---

Sie dürfen:

das Werk vervielfältigen, verbreiten und öffentlich zugänglich machen

Zu den folgenden Bedingungen:

Namensnennung. Sie müssen den Namen des Autors/Rechteinhabers in der von ihm festgelegten Weise nennen (wodurch aber nicht der Eindruck entstehen darf, Sie oder die Nutzung des Werkes durch Sie würden entlohnt).

Keine kommerzielle Nutzung. Dieses Werk darf nicht für kommerzielle Zwecke verwendet werden.

Keine Bearbeitung. Dieses Werk darf nicht bearbeitet oder in anderer Weise verändert werden.

- Im Falle einer Verbreitung müssen Sie anderen die Lizenzbedingungen, unter welche dieses Werk fällt, mitteilen. Am Einfachsten ist es, einen Link auf diese Seite einzubinden.
- Jede der vorgenannten Bedingungen kann aufgehoben werden, sofern Sie die Einwilligung des Rechteinhabers dazu erhalten.
- Diese Lizenz lässt die Urheberpersönlichkeitsrechte unberührt.

Quelle: http://creativecommons.org/licenses/by-nc-nd/2.5/ch/ Datum: 3.4.2009

Contents

1 Introduction

In this thesis experiments are presented which belong to the field of *mesoscopic physics* which is situated at the border between the macroscopic world with the laws of classical physics and the microscopic world where quantum mechanics rules. In quantum mechanics the properties of a physical system are described by a complex wave function. The length scale on which its phase is defined is called the *coherence length* L_ϕ which is a good measure in order to define the border mentioned above. Even though this description would also fit to optical measurement configurations with very large L_ϕ's, the notion mesoscopic physics is in general used for a sub-field of solid state physics dealing with small devices in the micron and nanometer range.

Mesoscopic physics is strongly related to the *technological development of processing techniques* which allows the controlled design of structures smaller than or in the range of the coherence length. This gives an additional possibility to study quantum mechanics by having a wider *control* over the parameters of the system. For instance the separation of the energy levels of a quantum dot can be controlled by varying its size. The base material used in this thesis are two-dimensional electron gases (2DEG) which are conducting planes that establish on the sharp interface between two semiconductors with different band gap. Applying a perpendicular magnetic field, the electron transport is governed by one-dimensional channels along the edge of the border. This 1D-channels can be considered as electron beams in a solid state environment. A description of sample preparation techniques is given in chapter 3.

Electronic transport measurements are an often used tool for the characterization of mesoscopic devices. Applying a voltage V and measuring the *mean current* $\langle I \rangle$ gives the mean transmission through the device and a first information about its electronic structure. The fluctuations of the current around its mean value $\Delta I(t) = I(t) - \langle I \rangle$ provide further information

as the quantization of the charge. They are characterized by the variance $\langle \Delta I^2 \rangle = \langle I^2 \rangle - \langle I \rangle^2$, which is called *noise*. In addition, in multi-terminal devices, the sign of the cross correlation of fluctuations between different terminals, $\langle \Delta I_1 \Delta I_2 \rangle$, can provide additional information as for instance the particle statistics. The basics of electron transport in mesoscopic systems are described in chapter 2.

In phase coherent systems, interference pattern develop. *Single particle* or *amplitude interference* arises from a superposition of single-particle processes and can be seen in the mean current $\langle I \rangle$ which is a function of the phase difference between the individual processes. It is also possible to probe the interference capability by *two-particle* or *intensity interference*. This is a consequence of a superposition of indistinguishable two-particle processes and appears in the cross correlation $\langle \Delta I_1 \Delta I_2 \rangle$ of the currents between two detectors and is as well a function of the phase difference between the two-particle processes. Textbook experiments concerning interference are mostly provided by the field of optics. An example for amplitude interference is a double slit experiment where the light passing the two slits is superposed and gives rise to an interference pattern on the screen behind. The first intensity interference experiments have been carried out by Hanbury Brown and Twiss in 1956 [1, 2] where they examined thermal light sources. In addition to an interference pattern they measured *positive* correlations, which is often labeled as *photon bunching* and was the starting point of the field of quantum optics [3–5]. It is interesting to compare such experiments with similar ones carried out with electrons. Because electrons interact much more with their surrounding environment, they loose their phase coherence much faster and therefore the length scales of such experiments are much smaller. However, the technical progress allows the production of such small structures, leading to realizations of electronic equivalents [6–9] with *negative* sign of the cross correlation (*electron anti-bunching*). A detailed discussion is given in chapter 4.

In chapter 5 the experiments of Henny et al. [6] and Oberholzer et al. [8],which used edge states as electron beams, are extended. Inspired by a proposal of Texier and Büttiker [10], which itself follows from a discussion of Refs. [6, 8], the impact of equilibration of current and current fluctuations between such edge states due to inelastic scattering is investigated. A beam

splitter experiment is presented where for *the first time* positive correlations have been measured in a normal-conducting Fermionic environment [11].

In the mentioned electron anti-bunching experiments [6–9] negative cross correlation have been shown but no interference pattern because the phase difference could not be changed in these experiments. In 2004, Samuelsson et al. [12] proposed a realization of a two-electron interferometer using again edge states as electron beams. This proposal was inspired by the electronic Mach-Zehnder interferometer reported by Ji et al. a year before [13]. While for an electronic Mach-Zehnder interferometer interference effects are seen in the conductance, for the two-electron interferometer they only show up in intensity correlations. Compared to conductance measurements, correlation measurements are much more complex. The signal is much smaller which leads to time consuming averaging processes. In order to produce such a two-source electron interferometer the same technical challenges have to be overcome as for a single-particle Mach-Zehnder interferometer. These are e. g. the small working Ohmic contacts in the middle of the sample or the free-standing bridges. Hence, in chapter 6 of this thesis a Mach-Zehnder interferometer has been produced and characterized in a first step in order to realize a two-source electron interferometer in a second step. Compared to other implementations of electronic Mach-Zehnder interferometers [13–16] the visibility has been investigated for a broad range of transmission values revealing an unexpected DC bias dependence.

Electronic Mach-Zehnder interferometer are very sensitive to a change of the phase difference between the two interferometer arms. Hence, as soon as they are understood good enough, they could be nice phase sensor devices to probe decoherence effects.

2 Electronic Transport in Mesoscopic Systems

2.1 Two-dimensional Electron Gas in a GaAs/AlGaAs-heterostructure

The starting wafer material for all samples in this thesis is a conventional GaAs / $Al_xGa_{1-x}As$-heterostructure with an aluminum portion of $x = 0.3$. Due to the similar lattice constants of GaAs and $Al_{0.3}Ga_{0.7}As$ (5.6533 Å / 5.6555 Å) they can be grown on top of each other by molecular beam epitaxy (MBE) [17] without strain (Sec. 3.1.1). Unlike the lattice constant, the band gap is different. For GaAs it is 1.42 eV and for $Al_{0.3}Ga_{0.7}As$ it is 1.8 eV. Connecting the two semiconductors leads to a bending of the bands in order to align the vacuum levels and the Fermi energy. The discontinuity of the conductance band ΔE_C is given by the difference in the electron affinity χ of the two materials $\Delta E_C = \chi_{\mathrm{II}} - \chi_{\mathrm{I}}$ (Fig. 2.1).

The layer sequence of a standard two-dimensional electron gas (2DEG) produced by MBE is shown in the upper part of Fig. 2.2. The substrate consist in undoped GaAs (small band gap material). Than a layer of undoped AlGaAs with a larger band gap is applied. The 2DEG forms at the interface of this two materials. Then a Si-doped layer of AlGaAs is added providing the electrons for the 2DEG. This separation of the donors (elastic impurities) and the electrons by an undoped *spacer layer* increases the mobility and is called *modulation doping* [18]. The electrons are are trapped in z-direction (perpendicular to the grow direction) and form quantized states with defined energy (Eq. 2.2), while they can move freely with high mobility in the xy-plane parallel to the interface. At low temperature only the lowest energy state, one subband, is occupied. A bit more quantitatively, we use an ansatz for the wave-function where the z- and xy-direction are separated:

$$\psi(\mathbf{r}) = \psi_j(z)e^{\mathrm{i}k_x x + \mathrm{i}k_y y} = \psi_k(z)e^{\mathrm{i}\mathbf{k}_\parallel \cdot \mathbf{r}}, \tag{2.1}$$

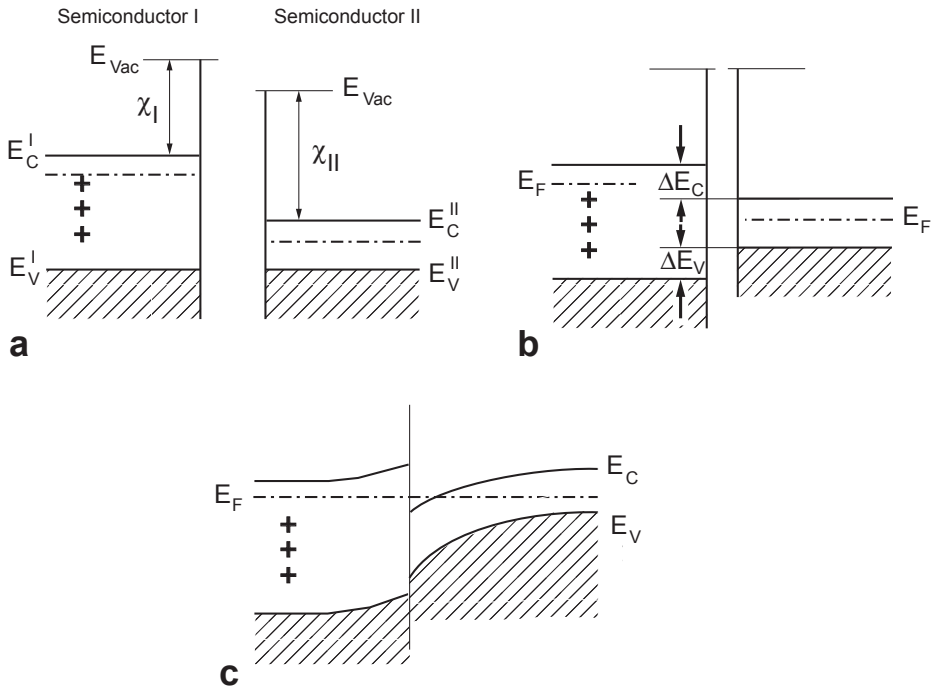

Figure 2.1: (a) Combining two semiconductors with different band gap. (b) The discontinuity of the conduction band ΔE_C is given by the difference in the electron affinity χ of the two materials $\Delta E_C = \chi_{II} - \chi_I$. (c) Finally, the bulk Fermi levels have to be aligned resulting in a bending of the bands. The conductance band at the interface of the small band gap semiconductor falls below the Fermi level and is filled with electrons from donors located in the large band gap semiconductor.

where $\mathbf{k}_\parallel$ stands for the wave-vector of the free movement in the xy-plane. Solving the Schrödinger equation we end up with "quasi"-continuous energy-eigenvalues in the xy-plane and discrete values ε_j for the quantum well in z-direction:

$$E_j(\mathbf{k}_\parallel) = \varepsilon_j + \frac{\hbar^2 k_\parallel^2}{2m_\parallel^*}. \tag{2.2}$$

These discrete energy-parabolas along x and y are so called *2D-subbands*. If the quantum well is narrow enough, only one subband is occupied. For

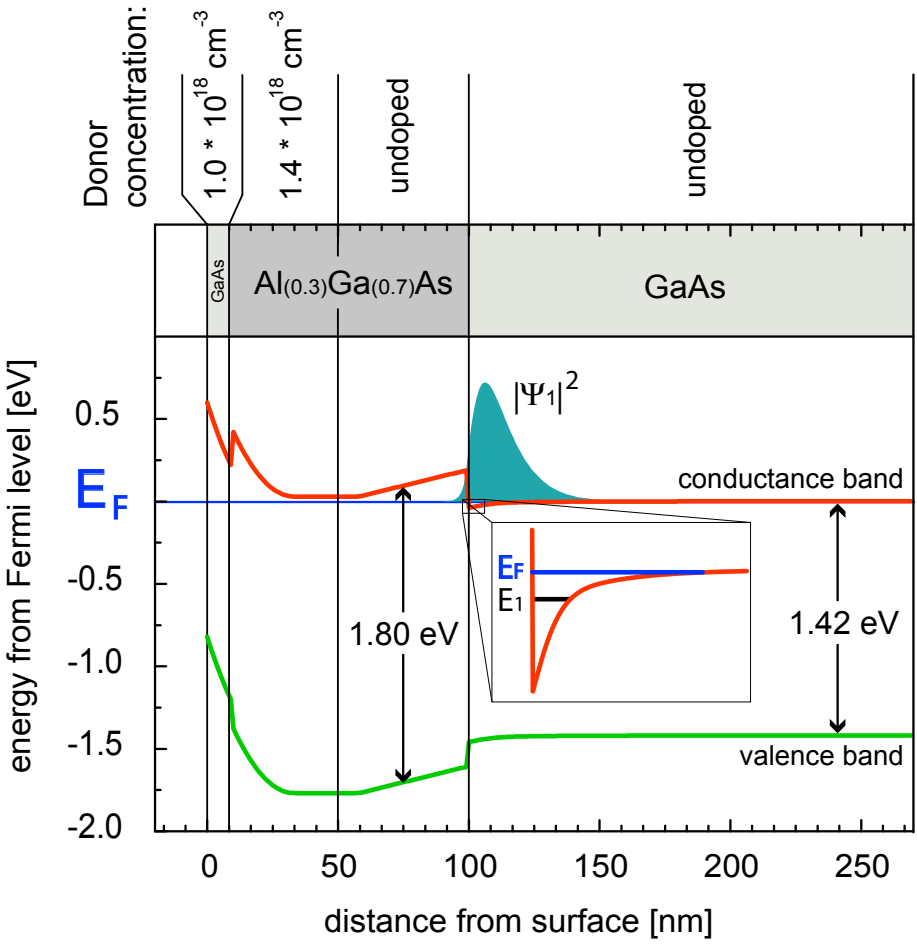

Figure 2.2: Band structure of a GaAs/$Al_{0.3}Ga_{0.7}As$ heterostructure calculated by a Poisson-Schrödinger solver [19, 20]. The growth direction of the MBE process is from right to the left. On the substrate undoped GaAs is applied with a thickness of around 1000 nm. Then 50 nm of undoped $Al_{0.3}Ga_{0.7}As$ are added. The 2DEG establishes at the interface between this two layers. 40 nm of n-doped $Al_{0.3}Ga_{0.7}As$ follow, providing the electrons for the 2DEG. Finally, a cap layer of 10 nm GaAs is applied.

the density of states $D_{2D}(E) = \partial N/(\partial V \partial E)$ of a 2D-subband we have first to know the number of occupied states N for a subband that is filled up

to the Fermi level ($k_BT = 0$). We get, spin degeneracy included,

$$N(k) = 2 \cdot \frac{\pi k^2}{(2\pi/L)^2} = \frac{k^2}{2\pi} \cdot V \qquad \text{with} \qquad V = L^2. \tag{2.3}$$

Hence the density of states for two dimensions $D_{2D}(E)$ is

$$D_{2D}(E) = \frac{\partial N}{\partial V \partial E} = \frac{\partial}{\partial E}(\frac{k^2}{2\pi}) = \frac{m^*}{\pi\hbar^2}, \tag{2.4}$$

with the dispersion relation $E(k) = (\hbar^2 k^2)/(2m^*)$. Hence the density of states in two dimensions is energy independent. This is in contrast to one dimension where the density of states is proportional to $1/\sqrt{E}$ while for three dimensions it is proportional to $\sqrt{E}$. The relation between the electron density n_e, the density of states D_{2D} and the Fermi energy E_F is as follows:

$$n_e = \int_0^{E_F} dE D_{2D}(E) = D_{2D} E_F = \frac{k_F^2}{2\pi}. \tag{2.5}$$

2.2 Length Scales in Mesoscopic Systems

A mesoscopic system itself is defined by length scales. It must be small enough to be influenced by quantum effects but it is still extended over several microscopic objects as atoms. The following length scales are often used to describe the physics in such systems: The de Broglie wavelength at the Fermi energy λ_F, and the mean free path L_m.

2.2.1 The Fermi Wavelength λ_F

Electron transport only takes place in an energy window of $2k_B\theta$ around the Fermi energy. With Eq. (2.5) the Fermi wavelength λ_F is related to the electron density n_e,

$$\lambda_F = \frac{2\pi}{k_F} = \frac{2\pi}{\sqrt{2\pi n_e}} = \sqrt{\frac{2\pi}{n_e}}. \tag{2.6}$$

For an electron density of $n_e = 2 \cdot 10^{15}\,\mathrm{m}^{-2}$ we get a Fermi wavelength of $\lambda_F = 56\,\mathrm{nm}$. This is much higher than the corresponding values of

metals. Gold for example has a Fermi wavelength of 0.5 nm. It might be an advantage that for constricting the dimensions of a system quantum effects develop faster for larger Fermi wavelengths (see also Sec. 2.3).

2.2.2 The Mean Free Path L_m

The mean free path is the distance that an electron travels before its initial momentum is altered by elastic scattering on impurities. This scattering process is described by scattering rate $1/\tau_m$, where τ_m denotes the momentum relaxation time. Thus, if the Fermi velocity v_F of the electrons is known, the mean free path is given by

$$L_m = v_F \tau_m. \tag{2.7}$$

The mobility μ is related to the momentum scattering time τ_m in the following way: $\tau_m = m^* \mu / e$. With the Fermi velocity $v_F = \hbar k_F / m^* = \hbar / m^* \cdot \sqrt{2\pi n_e}$ we get the following relation between mean free path and mobility: $L_m = \sqrt{2\pi n_e} \hbar \mu / e$.

2.3 Transverse Modes and Quantum Point Contacts

2.3.1 Transverse Modes

As already mentioned in Sec. 2.1, a 2DEG is a system strongly confined in one dimension (often labeled with z). This confinement leads to a quantization of the energy eigenvalues in the z-direction.

Constricting the 2DEG further along a second direction (y) leads to an additional quantization of the energy. Without knowing the details of the confining potential the number of *transmission channels* or *transverse modes* in a constriction with width W can be estimated. The k_y-vectors of electrons at the Fermi energy $E_F = \hbar^2 k_F^2 / (2m^*)$ can take values in the range of $2 \cdot k_F$. The quantized k_y-values are spaced by $2\pi/W$. This gives for the number M of transmission channels

$$M = \mathrm{Int}\left[\frac{2k_F}{2\pi/W}\right] = \mathrm{Int}\left[\frac{k_F W}{\pi}\right] = \mathrm{Int}\left[\frac{2W}{\lambda_F}\right]. \tag{2.8}$$

Hence in order to see quantization effects, a large Fermi wavelength is an advantage.

2.3.2 Quantum Point Contacts

A controllable constriction in a 2DEG can be realized by narrow gates, a so called *split gate* or *quantum point contact*. A negative voltage V_G applied to this gates lifts the conductance band underneath over the Fermi level and depletes the 2DEG. The depletion length l_d around the gates follows $l_d = 2\epsilon\epsilon_0 V_G/(\pi n_e e)$. This gives for $V_G = -1\,\mathrm{V}$, $n_e = 1.6 \cdot 10^{15}\,\mathrm{m}^{-2}$, $\epsilon_{\mathrm{GaAs}} = 13.1$ and the electric constant ϵ_0 a typical depletion length of 290 nm. For constrictions comparable to the Fermi wavelength the transport goes over discrete transport channels and the conductance as a function of the gate voltage shows a step like behavior every time a new channel open or closed. This conductance quantization relies on the fact that there is no mixing between the different transport channel which depends on the shape of the quantum point contacts. A smooth change of the width of the constriction provides an adiabatical coupling to the many-modes contacts [21].

2.4 Landauer-Büttiker Formalism and Scattering Approach

What is the resistance of a conductor if its length is smaller than the mean free path L_m? In this regime the transport is ballistic without any elastic scattering. One might expect that the measured resistance of this sample would go to zero. However this is not the case. Due to the small dimensions of the conductor a finite number of transport channels (or transverse modes) establish which can carry only a limited amount of current. The concept of transverse modes has been introduced in Sec. 2.3. The measured resistance results from a redistribution of the current transport from the huge amount of modes in the contact reservoirs to the few ones in the small conductor and is often called *contact resistance* [22].

2.4.1 Two-terminal conductor

The current transport through a conductor with a few M modes contacted to two terminals (with many modes) is is given by [22]:

$$I = GV \quad \text{where} \quad G = \frac{e^2}{h} \sum_{n=1..M} T_n. \tag{2.9}$$

$G = 1/R$ is the conductance and $V = \Delta\mu/e$ the applied bias. $\Delta\mu = \mu_1 - \mu_2$ is the difference in the electrochemical potentials of contacts 1 and 2. For the case of equal transmission T in every mode we can also write $G = e^2/h \cdot MT$. It is interesting to rewrite the corresponding resistance in the following way:

$$R = G^{-1} = \frac{h}{e^2 M}\frac{1}{T} = \underbrace{\frac{h}{e^2 M}}_{G_C^{-1}} + \underbrace{\frac{h}{e^2 M}\frac{1-T}{T}}_{\text{resistance of the modes}} . \tag{2.10}$$

The two-terminal resistance is a combination of the contact resistance G_C^{-1} due to the redistribution of the current on a small number of modes and a resistance due to *backscattering* ($T < 1$).

2.4.2 Multi-terminal conductor

We can expand this description to a multi-terminal configuration and non-zero temperature and bias. The current in contact α is given by ($\bar{T} = \sum_{n=1..M} T_n$)

$$I_\alpha = \int dE \frac{e}{h} \sum_\beta \bar{T}_{\alpha\beta}(E)[f_\alpha(E) - f_\beta(E)]. \tag{2.11}$$

In the linear response regime, i. e. in a energy window where the transmission is constant, we can linearize the formula above and get

$$I_\alpha = \sum_\beta G_{\alpha\beta}[V_\alpha - V_\beta] \qquad \text{with} \qquad G_{\alpha\beta} = \frac{e^2}{h} \int \bar{T}_{\alpha\beta}(E) \left(-\frac{\partial f_0}{\partial E}\right) dE. \tag{2.12}$$

f_0 is the equilibrium Fermi function. For low temperatures we get $-\frac{\partial f_0}{\partial E} \approx \delta(E_F - E)$ and for the conductance $G_{\alpha\beta} = \frac{e^2}{h}\bar{T}_{\alpha\beta}(E_F)$.

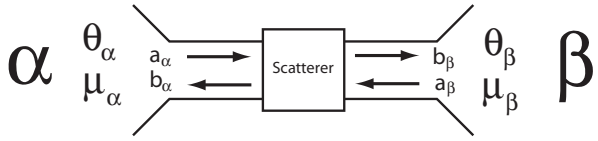

Figure 2.3: Schematics of the in- and outgoing scattering states in a two-terminal conductor with one channel.

2.4.3 Scattering Matrix

The elastic scattering process and its relation to the transmission probabilities can be described systematically with the help of the *scattering matrix* s and the incoming $\hat{a}^\dagger_{\alpha n}, \hat{a}_{\alpha n}$ and outgoing $\hat{b}^\dagger_{\alpha n}, \hat{b}_{\alpha n}$ scattering states of channel n and contact α. The scattering matrix elements and the transmission are connected as follows: $|s_{\alpha\beta;mn}(E)|^2 = T_{\alpha\beta;mn}(E)$. Each contact α that is connected to the sample has $N_\alpha(E)$ transverse channels and is described by a Fermi function $f_\alpha(E)$. The scattering matrix is unitary due to current conservation. The incoming and outgoing scattering states are related over the scattering matrix:

$$\hat{b}_{\alpha m}(E) = \sum_{\beta n} s_{\alpha\beta;mn}(E)\, \hat{a}_{\beta n}(E). \tag{2.13}$$

By subtracting the incoming and outgoing states in lead α the current operator can be written in the following form:

$$\hat{I}_\alpha(t) = \frac{e}{h} \sum_{\beta\gamma} \sum_{mn} \int dE dE' e^{i(E-E')t/\hbar} \hat{a}^\dagger_{\beta\gamma}(E) A^{mn}_{\beta\gamma}(\alpha; E, E') \hat{a}_{\beta\gamma}(E') \tag{2.14}$$

with the function

$$A^{mn}_{\beta\gamma}(\alpha; E, E') = \delta_{mn}\delta_{\alpha\beta}\delta_{\alpha\gamma} - \sum_k s^\dagger_{\alpha\beta;mk}(E) s_{\alpha\gamma;kn}(E'), \tag{2.15}$$

For the average current the quantum statistical average of the product of an electron creation and an annihilation operator of Fermions has to be calculated, i. e. $\langle \hat{a}^\dagger_{\alpha m}(E) \hat{a}_{\beta n}(E') \rangle = \delta_{\alpha\beta}\delta_{mn}\delta(E - E') f_\alpha(E)$.

With $G^*_{\alpha\beta} = d\langle I_\alpha \rangle / dV_\beta|_{V_\beta = 0}$ the average current is (which is equivalent to

Eq. 2.12):

$$\langle I_\alpha \rangle = \int dE \frac{1}{e} \sum_\beta G^*_{\alpha\beta}(E) f_\beta(E) = \sum_\beta G^*_{\alpha\beta} V_\beta \tag{2.16}$$

with $G^*_{\alpha\beta} = \frac{e^2}{h} \int dE \left(-\frac{\partial f}{\partial E}\right) [N_\alpha \delta_{\alpha\beta} - \mathrm{Tr}(s^\dagger_{\alpha\beta} s_{\alpha\beta})]$.

The equation for the current in the Landauer-Büttiker formalism is also used to calculated the current fluctuations around its mean value and their power spectral density (see Sec. 2.8.2).

2.5 2DEG in Perpendicular Magnetic Fields, IQHE

2.5.1 Low Magnetic Fields and Drude model

While a 2DEG is strongly confined in one direction (often labeled by z) (Sec. 2.1), in the other two dimensions there is no confinement in the order of magnitude of the Fermi wavelength. The 2DEG has an energy independent density of states and is characterized by the electron density n_e and the mobility $\mu \equiv |e|\tau_\mathrm{m}/m$ which is related to the elastic scattering time t_m, i. e. the average time it takes until the momentum is changed by an elastic collision (Sec. 2.2.2). Diffusive transport is described as a balance between elastic scattering processes that decrease the momentum and external electric and magnetic fields that drive it [22]:

$$\frac{m\mathbf{v}_D}{\tau_\mathrm{m}} = e[\mathbf{E} + \mathbf{v}_D \times \mathbf{B}]. \tag{2.17}$$

Rewriting this relation for a perpendicular magnetic field $B_z = B$ and an in-plane electric field E_x, E_y results in

$$\begin{pmatrix} E_x \\ E_y \end{pmatrix} = \begin{pmatrix} \rho_{xx} & \rho_{xy} \\ \rho_{xy} & \rho_{yy} \end{pmatrix} \begin{pmatrix} J_x \\ J_y \end{pmatrix}, \tag{2.18}$$

with the 2D-current density $\mathbf{J} = e\mathbf{v}_D n_e$. The components of the resistivity matrix are $\rho_{xx} = \rho_{yy} = \sigma^{-1} = 1/(|e|n_e\mu)$ with the conductivity $\sigma \equiv |e|n_e\mu$ and $\rho_{xy} = -\rho_{yx} = B/(|e|n_e)$. The longitudinal resistivity ρ_{xx} is

constant while the perpendicular, so called Hall resistivity ρ_{xy} increases with magnetic field. Assuming only a current flow in x-direction gives $E_x = \rho_{xx} J_x$ and $E_y = \rho_{xy} J_x$. With the voltage drops along and across the sample, $V_{xx} = E_x L$ and $V_{xy} = V_H = E_y W$ and the total current $I = W J_x$ we get

$$R_{xx} = \frac{V_x x}{I} = \rho_{xx} \frac{L}{W} \qquad \text{and} \qquad R_{xy} = \rho_{xy} = \frac{V_H}{I}, \tag{2.19}$$

i. e. the transverse resistance is independent of the width W while the longitudinal resistance depends on the aspect ratio L/W. This is the so called Drude model.

The Hall effect in bulk conductors discovered by Edwin Hall in 1879 [23] can be explained by the Drude model. For bulk conductors we just need to replace the 2D-current density by the bulk current density.

2.5.2 High magnetic fields

For higher magnetic fields the previously constant density of states changes to an energy level structure with a magnetic field dependent spacing. For a more detailed discussion see e. g. [22]. The transport of the quasi-particles in the xy-plane is described by the effective mass equation

$$\left[E_s + \frac{(i\hbar\nabla + e\mathbf{A})^2}{2m^*} + U(y) \right] \Psi(x,y) = E\Psi(x,y). \tag{2.20}$$

For a perpendicular magnetic field in z-direction the vector potential $\mathbf{A}$ is not unique. An often chosen gauge is such that solution has the form of plane waves in the x-direction, i. e. $\Psi(x,y) = 1/\sqrt{L} e^{ikx} \chi(y)$: $A_x = -By$ and $A_y = 0$. Eq. (2.20) reduces to

$$\begin{gathered} \left[E_s + \tfrac{p_y^2}{2m^*} + \tfrac{1}{2} m^* \omega_c^2 (y + y_k)^2 \right] \chi(y) = E\chi(y) \\ \text{with} \quad y_k = \tfrac{\hbar k}{eB} \quad \text{and} \quad \omega_c = \tfrac{|e|B}{m^*}, \end{gathered} \tag{2.21}$$

where ω_c is the cyclotron frequency. The eigenfunctions of this equation are Hermite polynomials and the eigenenergies

$$E(n,k) = E_s + (n + \frac{1}{2})\hbar\omega_c, \qquad n = 0, 1, 2, \ldots \tag{2.22}$$

Hence the density of states has split up in so called *Landau levels*, spaced by the energy $\hbar\omega_c$. Since the electron density has not changed, the same amount of electrons as before has now to be distributed to the $\hbar\omega_c$-spaced levels. The number of electrons per Landau level or its *degeneracy* are therefore $N_0 = \hbar\omega_c \times m^*/\pi\hbar^2 = 2eB/h$.

In order to measure effects that rely on the changed density of states as the integer quantum Hall effect (Sec. 2.5.4), the spacing of the levels should be bigger than their broadening through temperature and elastic scattering, i. e.

$$\hbar\omega_c \gg \hbar/\tau_m \qquad \Rightarrow \qquad B \gg \mu^{-1} \qquad \text{and} \tag{2.23}$$

$$\hbar\omega_c \gg k_B\theta \qquad \Rightarrow \qquad B \gg \frac{m^*}{\hbar}\frac{k_B\theta}{e}. \tag{2.24}$$

2.5.3 Edge States

Transport takes only place for electrons at the Fermi edge. Changing the perpendicular magnetic field changes the spacing $\hbar\omega_c = \hbar|e|B/m^*$ of the Landau levels. Hence the density of states at the Fermi energy is changing in an oscillating way between two completely different regimes. If we have occupied states on the Fermi edge transport is allowed while for a Fermi energy between two Landau levels, the DOS is zero and there is no transport at all.

However, every real 2DEG is also finite in the xy-plane either due to a removal of the heterostructure i. e. by etching or due to a confinement of the electrons in the xy-direction by depleting the 2DEG with a negatively biased gate. This situation can be described with a confining potential U. Assuming a confinement in y-direction: $U(y) = \frac{1}{2}m^*\omega_0^2 y^2$. Again starting with the effective mass equation (Eq. 2.20), it can be shown [22] that the dispersion relation has an additional parabolic term:

$$E(n,k) = (n+\frac{1}{2})\hbar\omega_{c0} + \frac{\hbar^2k^2}{2m^*}\frac{\omega_0^2}{\omega_{c0}^2} \qquad \text{where} \qquad \omega_{c0}^2 \equiv \omega_c^2 + \omega_0^2. \tag{2.25}$$

This so called *magnetic subbands* lead to a different situation for a bulk Fermi level between the Landau levels: Unlike in a infinite 2DEG there are

now still occupied states at the Fermi energy near the edges of the sample. Additionally the k^+- and k^--states are spatially separated to opposite sides of the sample, leading to a massive reduction of backscattering. This states are called *edge states* and behave as 1D ballistic channels. The number of channels is given by the number of Landau levels below Fermi energy and therefore decreases for higher magnetic fields. It is often called the *filling factor* ν.

2.5.4 Integer Quantum Hall Effect

In Sec. 2.5.1 we mentioned the classical Hall effect. In a 2DEG in a perpendicular magnetic field, magnetic subbands develop (Sec. 2.5.3). Their consequence is the spatial separation of the right and left moving carriers to opposite sides of the plane for magnetic fields for which the 2DEG-bulk Fermi niveau is between two Landau levels. The number of channels is given by the filling factor ν. In Fig. 2.4, upper part, a so called *Hall bar* is shown with a defined width W and length L. The current is injected at contact 1 and leaves the sample at contact 5. A constriction in the middle of the sample, e. g. a quantum point contact (Sec. 2.3.2), transmits M and reflects $\nu - M$ channels. Applying the Landauer-Büttiker formalism (Sec. 2.4) gives the following results for the voltage drops along $V_2 - V_3$ and perpendicular $V_4 - V_3$ to the current direction:

- longitudinal resistance $R_L = R_{xx} = R_{23} = \frac{V_2 - V_3}{I} = \frac{h}{e^2}(\frac{1}{M} - \frac{1}{\nu})$
- Hall resistance $R_H = R_{xy} = R_{34} = \frac{V_4 - V_3}{I} = \frac{h}{e^2}\frac{1}{\nu}$.

I. e. for all channels transmitted ($M = \nu$) by the constriction, there is no voltage drop along the ballistic edge states. The voltage drop between to opposite contacts only depends on the number of edge states and fundamental physical constants.

In Fig. 2.4, lower part, a typical measurement is shown. For integer filling factors the longitudinal resistance R_{xx} goes to zero while the Hall resistance shows up a plateau. In such an integer quantum Hall effect regime, where current flows along ballistic edge states, all experiments in this thesis have been carried out.

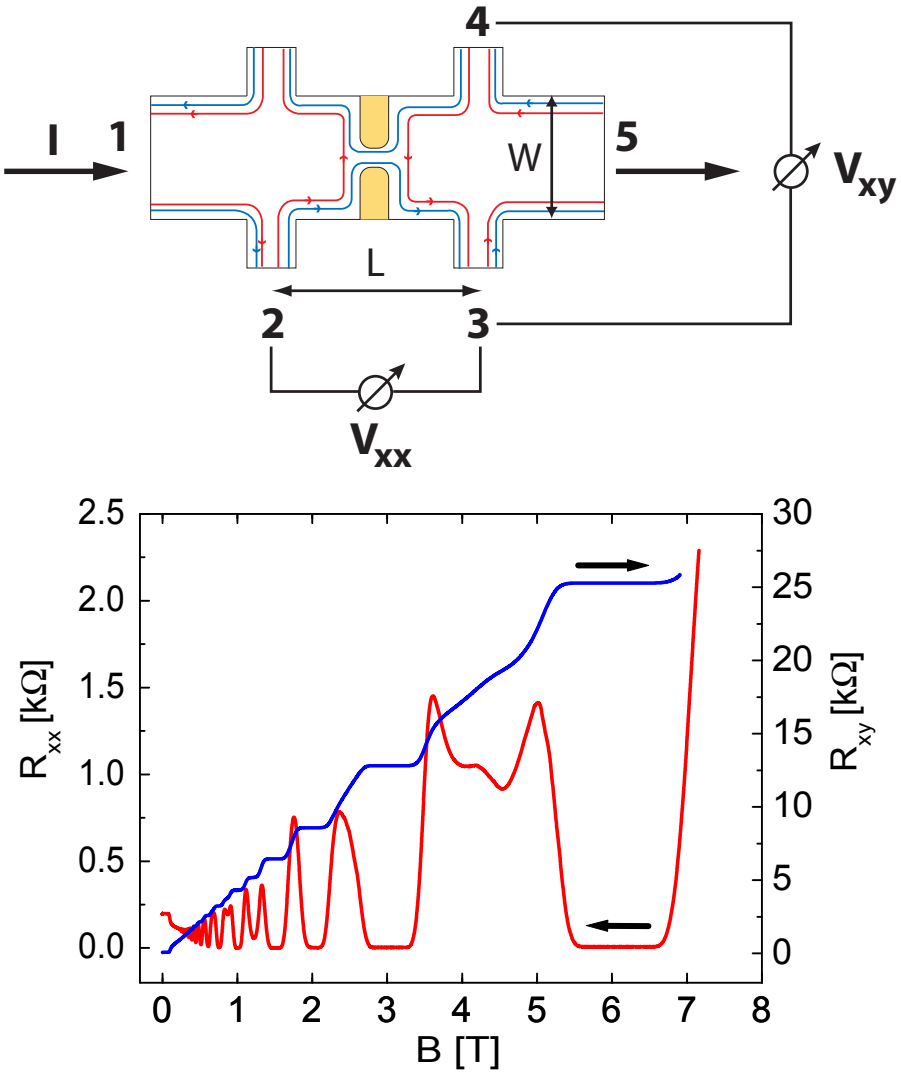

Figure 2.4: *Upper part*: A typical Hall bar configuration that allows to measure the voltage drop along and perpendicular to the current direction. *Lower part*: Corresponding measurement versus the magnetic field.

2.6 The Aharonov-Bohm-Effect

A certain magnetic field $\mathbf{B} = \operatorname{curl} \mathbf{A}$ belongs to different gauges of the vector potential $\mathbf{A}$, because adding a gradient of a scalar field $\nabla\Lambda$ to $\mathbf{A}$ does not affect $\mathbf{B}$: $\operatorname{curl}(\nabla\Lambda) = 0$. For a $\mathbf{B}$-field free region we can set:

$$\mathbf{A} = \nabla\Lambda \qquad \Rightarrow \qquad \Lambda(\mathbf{x}) = \int_{x_0}^{x} ds \cdot \mathbf{A}(\mathbf{s}) \tag{2.26}$$

The phase of the wave function is however affected by a change of the gauge: $\mathbf{A} = 0 \Rightarrow \mathbf{A} = \nabla\Lambda$:

$$\psi(\mathbf{x}) = \psi(\mathbf{x})_0 \exp\left\{i\frac{e}{\hbar}\Lambda\right\} = \psi(\mathbf{x})_0 \exp\left\{i\frac{e}{\hbar}\int_{\mathbf{x_0}}^{\mathbf{x}} d\mathbf{s}\, \mathbf{A}(\mathbf{s})\right\}. \tag{2.27}$$

In a double slit experiment, a wave is split up into two partial waves ψ_1 and ψ_2. The resulting wave after passing the slit is just their superposition $\psi_{\text{tot}} = \psi_1 + \psi_2$. For a defined relative phase an interference pattern is measured for $|\psi_{\text{tot}}|^2$. The additional phase due to the change of gauge gives

$$\begin{aligned} \psi_{\text{tot}}(\mathbf{x}) &= \psi_{1,0}(\mathbf{x}) \exp\left\{i\frac{e}{\hbar}\int_{\mathbf{1}} d\mathbf{s}\, \mathbf{A}(\mathbf{s})\right\} + \psi_{2,0}(\mathbf{x}) \exp\left\{i\frac{e}{\hbar}\int_{\mathbf{2}} d\mathbf{s}\, \mathbf{A}(\mathbf{s})\right\} \\ &= \left(\psi_{1,0}(\mathbf{x}) \exp\left\{i\frac{e}{\hbar}\Phi_B\right\} + \psi_{2,0}(\mathbf{x})\right) \exp\{\phi_2\}. \end{aligned} \tag{2.28}$$

with the total magnetic Φ_B flux through the area enclosed by the two paths and the phase ϕ_2 of path 2:

$$\begin{aligned} \Phi_B &= \int_{\mathbf{1}} d\mathbf{s}\, \mathbf{A}(\mathbf{s}) - \int_{\mathbf{2}} d\mathbf{s}\, \mathbf{A}(\mathbf{s}) = \oint d\mathbf{s}\, \mathbf{A}(\mathbf{s}) = \int d\mathbf{f} \operatorname{curl} \mathbf{A} = \int d\mathbf{f}\, \mathbf{B} \\ \phi_2 &= i\frac{e}{\hbar}\int_{\mathbf{2}} d\mathbf{s}\, \mathbf{A}(\mathbf{s}). \end{aligned} \tag{2.29}$$

Thus the interference pattern is periodic in a change of the magnetic flux by h/e. This can be reached by changing the area *or* the magnetic field and is known as the *Aharonov-Bohm-Effect* [24].

2.7 Fundamentals of Noise Measurements

A typical transport measurement of quasi-particles through mesoscopic devices with resistance R consists in the determination of its conductance $G = 1/R$. The conductance of a conductor with M channels is given by the Landauer-Büttiker formula $G = e^2/h \cdot \sum_n T_n$. In the linear response regime, i. e. for such small biases that the transmission is energy independent, the mean current corresponds to the conductance as follows: $\langle I \rangle = G\Delta\mu/e$ where $\Delta\mu/e$ is the applied bias. However, the mean current does only contain information about an average over the transmission eigenvalues T_n.

The transmission of the charge through a conductor is not a continuous process. It is carried by discrete particles. Their stochastic movement gives rise to fluctuations in the current around its mean value $\Delta I = I(t) - \langle I \rangle$. Since this fluctuations also depend on the transmission process they provide further information and an increased insight.

We will first give a short introduction in the basic definitions and expressions of noise measurements and than concentrate on shot noise in mesoscopic conductors.

Under the notion *noise* we will understand the variance of the fluctuations around its mean value $\langle I \rangle$:

$$\langle \Delta I^2 \rangle = \langle (I - \langle I \rangle)^2 \rangle = \langle I^2 \rangle - \langle I \rangle^2 \tag{2.30}$$

Its square root is also known as the standard deviation. Experimentally, the average is taken over time[1]. How can we describe and measure this fluctuations? In order to do this we will introduce the *correlation function* C_I and the *power spectral density* S_I of the fluctuations and their relation.

[1] Fluctuations which are described by its mean value and variance have a Gaussian distribution. This is often a good approximation and higher moments of noise will not be considered here.

2.7.1 Correlation function C_I

The correlation function is defined as follows [25]:

$$C_I(t_1,t_2) \equiv \langle \Delta I(t_1)\Delta I(t_2)\rangle = \langle I(t_1)I(t_2)\rangle - \langle I(t_1)\rangle\langle I(t_2)\rangle = \\ = \lim_{N\to\infty}\frac{1}{N}\sum_{i=1}^{N}\Delta I(t_1)\Delta I(t_2), \quad (2.31)$$

where average has been taken over an ensemble of identical samples. In a real experiment averaging is mostly done over a sufficient long time record t_m of the random process $I(t)$. For a stationary system with a time independent mean value the correlation function only depends on the time difference:

$$C_I(t_1-t_2) \equiv \lim_{t_m\to\infty}\frac{1}{t_m}\int_{-t_m/2}^{t_m/2} dt\Delta I(t_1+t)\Delta(t_2+t). \quad (2.32)$$

If the time difference is zero then the correlation function coincides with the variance, the average fluctuations squared: $C_I(t,t) = \langle(\Delta I)^2\rangle$. On the other side, if $|t_1-t_2| \to \infty \Rightarrow C_I(t_1-t_2) \to 0$ which means that the system "forgets" its initial fluctuation. This characteristic time of forgetting is the relaxation time.

The Fourier transform of the correlation function is given by

$$C_I(\omega) = \int_{-\infty}^{+\infty} d(t_1-t_2)e^{i\omega(t_1-t_2)}C_I(t_1-t_2) \quad (2.33)$$

2.7.2 Power Spectral Density S_I

The current fluctuations in the frequency domain are given by the Fourier transform

$$\Delta I(t) = \int_{-\infty}^{+\infty}\frac{d\omega}{2\pi}\Delta I(\omega)e^{-i\omega t}. \quad (2.34)$$

Regarding only the current fluctuations in a certain frequency window Δf around a central frequency $\overline{f}$, $\Delta I(t|\overline{f},\Delta f)$, one has to set the integration limits in Eq. 2.34 according to this frequency interval. This signal squared

is the *noise power*. Its mean value can be expressed by the *power spectral density* $S_I(\overline{f})$ at the central frequency times the considered frequency interval Δf:

$$\overline{[\Delta I(t)|\overline{f}, \Delta f]^2} \approx S_I(\overline{f})\Delta f. \tag{2.35}$$

2.7.3 Wiener-Khintchine Theorem

Basically by using the Fourier transform of the current fluctuations as well as the one of the correlation function (Eqs. 2.33 / 2.34), a very important relation between the power spectral density can shown, the *Wiener-Khintchine theorem*:

$$S_I(f) = 2\int_{-\infty}^{\infty} d(t_1 - t_2)\, e^{i\omega(t_1-t_2)} C_I(t_1 - t_2) \equiv 2C_I(\omega). \tag{2.36}$$

Implying a frequency independent, "white", spectrum, which is indeed the case for equilibrium and shot noise (Sec. 2.8.2.1 and 2.8.2.2), opens the possibility to measure current auto- and cross-correlations via a spectrum analyzer in a finite frequency interval.

2.8 Noise in Mesoscopic Devices

We now concentrate on devices which are small enough that dephasing and inelastic effects can be neglected and the equilibrium and shot noise is described in terms of its elastic properties.

2.8.1 Poissonian Noise

First we calculate the noise of independently emitted particles as it has been done by Walter Schottky in 1918 for a vacuum tube [26]. With τ we denote the mean time between two tunneling event, t stands for the measurement time. The probability for N transmitted particles in the time t is given by

$$P_N(t) = \frac{t^N}{\tau^N N!} e^{-t/\tau} = \frac{\langle N\rangle^N}{N!} e^{\langle N\rangle}, \tag{2.37}$$

with $\langle N\rangle = t/\tau$. This Poisson distribution has the following property: $\langle N^2\rangle - \langle N\rangle^2 = \langle N\rangle$. So we can write for the mean current $\langle I\rangle = e\langle N\rangle/t = e/\tau$ and the final result for the power spectral density is

$$S_I = e^2(\langle N^2\rangle - \langle N\rangle^2)/t = e\langle I\rangle. \tag{2.38}$$

With this formula we can describe a tunneling situation with small transmission T. It depends on the charge e of the quasi-particle and is used to compare the strength of the noise as we see later.

2.8.2 Scattering Approach to Noise

A systematic procedure is the so called scattering approach to noise which has been generalized to multichannel, multi-terminal conductors by Büttiker [27, 28]. In Fig. 2.3 a schematics of a two-terminal scatterer is shown.

The power spectral density is defined as two times the Fourier transformation of the correlation function of the current fluctuations (Eq. 2.36),

$$2\pi\delta(\omega+\omega')S_{I,\alpha\beta}(\omega) \equiv \langle \Delta\hat{I}_\alpha(\omega)\Delta\hat{I}_\beta(\omega') + \hat{I}_\beta(\omega')\Delta\hat{I}_\alpha(\omega)\rangle. \tag{2.39}$$

In this calculation the quantum statistical expectation value of the product of four creation and annihilation operator goes in. The result for zero-frequency noise is

$$\begin{aligned} S_{I,\alpha\beta} \equiv S_{I,\alpha\beta}(\omega=0) &= \frac{e^2}{h}\sum_{\gamma\delta}\sum_{mn}\int dE A^{mn}_{\gamma\delta}(\alpha;E,E)A^{nm}_{\delta\gamma}(\beta;E,E)\times \\ &\times \{f_\gamma(E)[1-f_\delta(E)] + [1-f_\gamma(E)]f_\delta(E)\}, \end{aligned} \tag{2.40}$$

where the $A^{mn}_{\gamma\delta}$ are given by Eq. 2.15. Rewriting this basis invariant formula in the right basis of *eigen-channels* gives (where the T_n denote the corresponding transmission *eigen-values*)

$$\begin{aligned} S_I(\omega=0) &= \frac{e^2}{h}\int dE[\sum_n T_n(E)\,[f_1(1-f_1)+f_2(1-f_2)] + \\ &+ \sum_n T_n(E)[1-T_n(E)](f_1-f_2)^2]. \end{aligned} \tag{2.41}$$

In the next two subsections we discuss Eq. (2.41) for different temperature and bias limits.

2.8.2.1 Equilibrium Noise

For a bias much smaller than the temperature $|\mu_1 - \mu_2| \ll k_B\theta$, the first two terms on the right-hand side of Eq. (2.41) dominate. With $f_i(1-f_i) = -k_B\theta\partial f_i/\partial E = k_B\theta\delta(E_i - E)$ and assuming spin degeneracy we get the Johnson-Nyquist formula [29–32] for the thermal equilibrium power spectral density of the current fluctuations:

$$S_I(\omega = 0) = 2 \cdot 2\frac{e^2}{h}\sum_n T_n k_B\theta = 4Gk_B\theta. \tag{2.42}$$

Experimentally, mostly the induced voltage fluctuations over a resistor R are measured, $\Delta V = R\Delta I$. This gives for the thermal equilibrium power spectral density of the voltage fluctuations:

$$S_V = R^2 S_I = 4R^2/Rk_B\theta = 4Rk_B\theta. \tag{2.43}$$

2.8.2.2 Shot Noise

In the opposite limit, $|\mu_1 - \mu_2| \gg k_B\theta$, the first two terms of Eq. (2.41) vanish and the third term reduces to (assuming $T(E)$ constant in the range of integration)

$$\begin{aligned} S_I(\omega = 0) &= \sum_n T_n(1-T_n)\frac{e^2}{h}\int_{\mu_1}^{\mu_2} dE(f_1 - f_2)^2 = \\ &= \frac{e^2}{h}\Delta\mu\sum_n T_n(1-T_n). \end{aligned} \tag{2.44}$$

In order to quantify the shot noise, its power spectral density is often compared to the one of Poissonian noise (Sec. 2.8.1), this ratio is called the *Fano factor* F:

$$F \equiv \frac{S_I(\omega=0)}{e\langle I\rangle} = \frac{\frac{e^2}{h}\Delta\mu\sum_n T_n(1-T_n)}{e\frac{\Delta\mu}{e}\frac{e^2}{h}\sum_n T_n} = \frac{\sum_n T_n(1-T_n)}{\sum_n T_n}. \tag{2.45}$$

Hence for a single channel with transmission T the Fano factor is given by $F = 1 - T$. The full Poissonian noise is recovered for small transmissions

$T \ll 1$. On the other side, a channel with transmission $T = 1$ shows no current fluctuations, e. g. a ballistic edge state.

What is gained by a noise measurement respect to the measurement of the average current? The average current gives information about an average over the transmission eigenvalues $\sum_n T_n$. However, the low-frequency shot noise at low temperatures is an average over the expression $\sum_n T_n(1-T_n)$. Hence, one gets more information about the distribution of the transmission eigenvalues. Going to even higher orders of the fluctuations the picture of the transmission would become even more complete. However in this thesis a noise measurement is always restricted to the determination of the second moment of the current fluctuations.

As seen from Eqs. (2.38) and (2.45) the power spectral density is proportional to the charge of the electron. In a more general treatment it is proportional to the charge q of the quasi-particles involved in transport. This could be shown for the charge $2e$ of Cooper pairs in superconducting transport through an SNS-junction [33] and for the fractional charge $e/3$ in the fractional quantum Hall regime [34, 35].

Dealing with mesoscopic conductors with a large number of transmission eigenvalues T_n, the expression $\sum_n T_n(1-T_n)$ in the power spectral density can be replaced by $\int_0^1 \rho(T)T(1-T)$ where $\rho(T)$ is the distribution of the transmission eigenvalues, which has been calculated for a chaotic cavity [36] and diffusive wires [37]. The result is, which has also experimentally shown, that for chaotic cavities the Fano factor of $1/4$ [38] while for diffusive wires it is $1/3$ [39–41].

The power spectral density is also sensitive to the Fermi distribution function f of the reservoirs (Eq. 2.41), which can deviate from the degenerated step-function in the case of relaxation processes due to interactions. This changes e. g. the Fano factor for diffusive wires in the case of hot electrons from $1/3$ to $\sqrt{3}/4$.

3 Sample Preparation and Low-Temperature Measurements

⇒ ***For detailed process parameters see appendix B.*** ⇐

3.1 Sample Preparation Techniques

3.1.1 Molecular Beam Epitaxy

The GaAs / $Al_xGa_{1-x}As$-heterostructures used in this thesis were grown by molecular beam epitaxy (MBE) [17]. In the MBE process, the materials are heated up in effusion cells and fly by thermal activation through the ultra-high vacuum (UHV) of 10^{-10} mbar onto the substrate. This vacuum corresponds to mean free paths of meters. The different material sources are controlled by shutters. This gives the possibility to build up new semiconductors where the composition can be controlled on a monolayer scale. By evaporating materials on top of each other with a similar lattice constant but different band gap, one has a mean to design the bandstructure of the new material. A model system is the combination of GaAs and AlAs which have approximately the same lattice constant, 5.6533 Å for GaAs and 5.6605 Å for AlAs. The lattice constant a of the ternary compound $Al_xGa_{1-x}As$ is generally calculated by $a(Al_xGa_{1-x}As) = a(GaAs) + x \cdot (a(AlAs) - a(GaAs))$ resulting in a lattice constant of 5.6555 Å for $x = 0.3$. Due to the different band gap of GaAs and $Al_{0.3}Ga_{0.7}As$ (1.42 / 1.8 eV) the bands are bend at the interface in order to align the vacuum levels and the Fermi energy resulting in a conducting layer at the interface as described in Sec. 2.1.

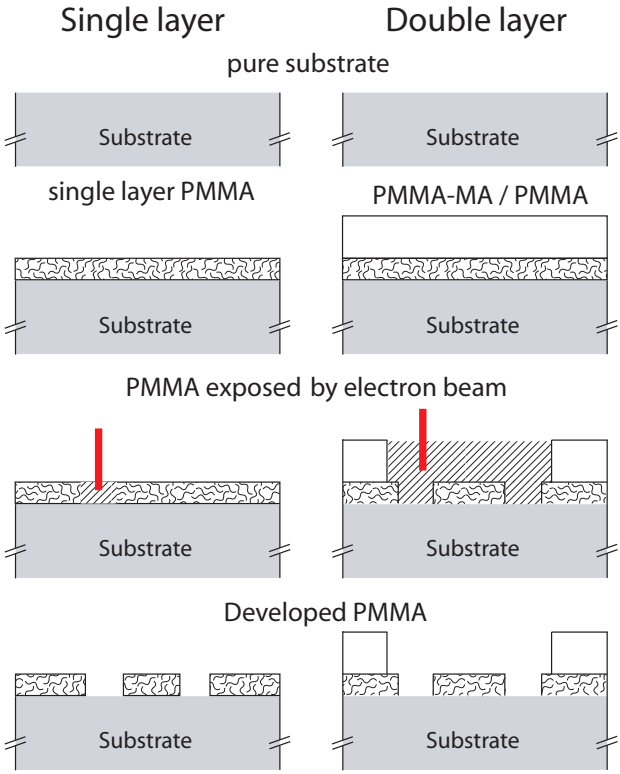

Figure 3.1: Processing a positive resist as PMMA by electron beam lithography. The electron beam breaks bonds in the long polymer chains of the resist and hence reduces their molecular weight. Therefore they are washed out more easily by the developer. For more complex structures as free standing metal bridges, double layer techniques are used.

3.1.2 Electron Beam Lithography

In mesoscopic physics devices on a sub micron scale are fabricated and studied. An appropriate means of fabrication is *electron beam lithography (EBL)*. Lithography stems from old-Greek and means actually a simple printing technique with stones as a stamp. Nowadays, the notion of lithography is extended to techniques which use some kind of mask to treat and form the subject of interest.

In EBL, a resist which is sensitive to electrons with energies in the range of keV, is structured by a beam of accelerated electrons. In our case the electron source is an electron microscope with appropriate control software. The limiting factor for small structures in the range of tens of nanometers is in general not the beam size of the electron microscope ($\cong$ nm) but the backscattered electrons from the resist and substrate that broaden the exposed area (proximity effect). This makes it challenging but not impossible to write structures below 50 nm.

A frequently used resist for EBL is the polymer *polymethyl methacrylat* (PMMA). It is applied onto the substrate as a thin film by fast spinning. The height of the film is typically several hundreds of nanometer and can be controlled by tuning spin time and velocity and by diluting the PMMA with *chlorobenzene*. In order to remove the solvents, the samples are baked out in an oven after spinning.

PMMA consists of long polymer chains. The accelerated electrons from the electron microscope break bonds and reduce therefore the molecular weight M of the molecules. This results in a better solubility in an appropriate developer. A resist where the *exposed* areas are washed out by the developer is called *positive*. As a developer a mixture of *4-Methyl-2-pentanone (MiBK)* and *2-propanol / isopropanol (IPA)* is used. More complicated structures as free standing bridges can be produced by using more than one layer and a combination of resists with different sensitivity. For more details see section 3.4.2.

Such a mask produced by EBL is finally used to structure the sample by different methods as, *reactive ion etching*, *metalization* or *wet-etching* which are described in more detail in sections 3.1.3 - 3.1.5 and Figs. 3.1 - 3.3.

3.1.3 Reactive Ion Etching

After developing and washing out the exposed resist there might still be some residual PMMA left. Especially for the production of good Ohmic contacts to a 2DEG this can be a limiting factor, because it would prevent or disturb the delicate annealing process (Sec. 3.3).

Therefore, the samples have always been cleaned in a weak oxygen plasma after EBL and before metalization. The method is also called *reactive ion etching*. After pumping out the sample chamber and filling it with oxygen, the plasma is produced by a strong radio frequency (RF) electromagnetic field which is applied between two capacitor plates in order to ionize the gas molecules. The surface of the sample is structured both by chemical reaction and accelerated ions that kinetically take away material.

The etching rate depends on many process parameters which also shift with time. Hence, before every delicate sample preparation, a test of the etching rate has been performed.

3.1.4 Metalization

In order to deposit metals with an accuracy in the micron to nanometer scale on a substrate, a thin film of PMMA is applied onto the latter and then structured by electron beam lithography (see Fig. 3.2). In a next step substrate and resist are covered with a thin metal film. Then a strong organic solvent as acetone is used to remove the mask (*lift-off*) and to wash away the metal covering the resist. Only the metal in direct contact with the substrate remains and hence the pattern of the structured resist is transferred onto the sample.

The application of a thin film of metals is done in an electron gun evaporation system. It works by heating up a metal source in a vacuum chamber and letting the metal evaporate onto the sample covered with the mask. For a ballistic flight of the evaporated material, for purity and in order to prevent oxidation a good vacuum is needed. It depends on material and is generally below 10^{-6} mbar. The material source is heated up by bombarding it with accelerated electrons of an energy of 10 keV. With shutters between source and sample the evaporation process can be started when a constant deposition rate is established. The rate is controlled by a calibrated piezo-electric quartz crystal. Its resonant frequency is shifted the more material is evaporated onto it.

For our samples that are based on a two dimensional electron gas at the interface of a GaAs/AlGaAs-heterostructure, we apply either materials for

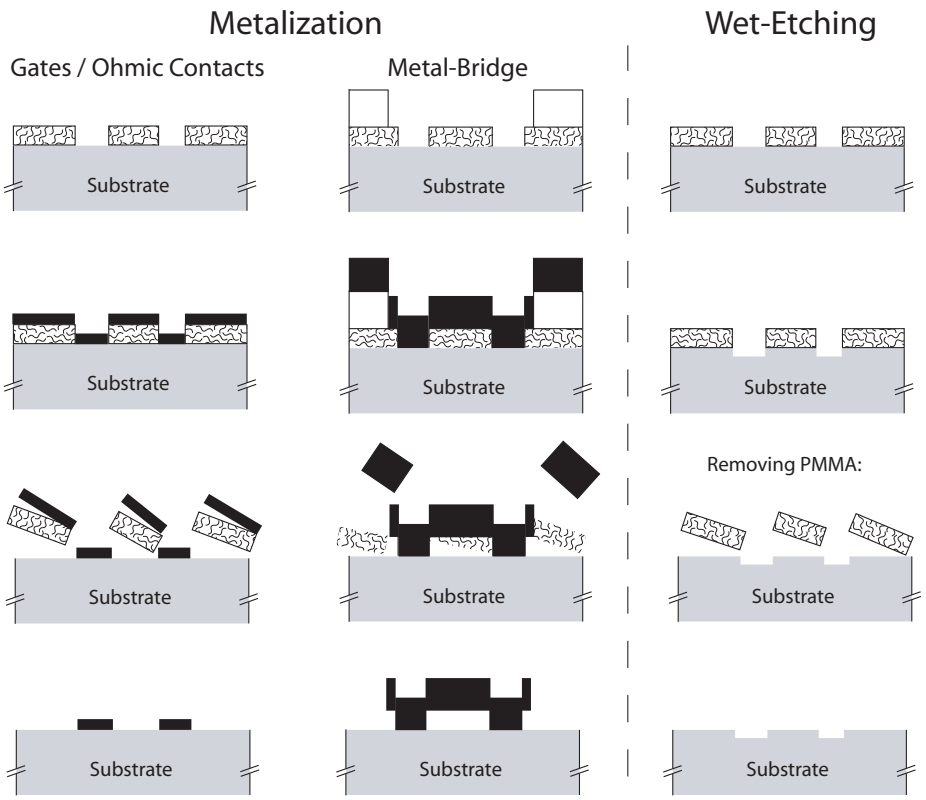

Figure 3.2: Transferring the pattern of the structured resist onto the sample either by metalization or wet-etching. In order to produce more complicated structures, as e. g. free-standing bridges, a double layer process was used.

Schottky contacts, i. e. the gates in order to control the electron density of the 2DEG (Sec. 3.2), for Ohmic contacts, i. e. the contacts for an electrical transport measurement (see Sec. 3.3) or for free standing metallic bridges (see Sec. 3.4.2).

3.1.5 Wet-Etching

The 2DEG can be structured by etching away the interface or at least the donor layer between surface and interface (shallow etching). The part where

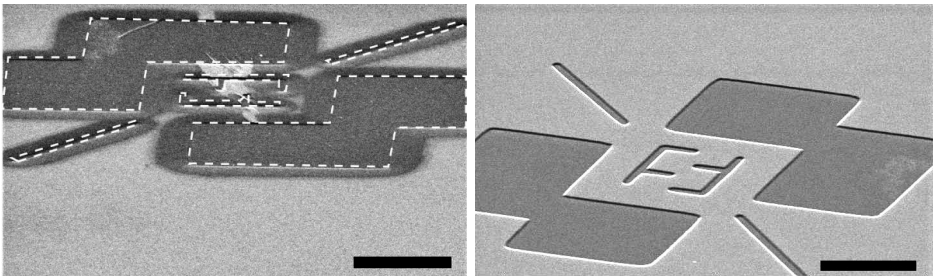

Figure 3.3: Two times the same test structure etched in a dummy GaAs wafer. *Left*: Standard cleaning treatment of the wafer with eventually ultrasonic, rinsing with acetone and IPA/ethanol before spinning resist. The PMMA mask got under-etched in a range of 1 μm. *Right*: Improved fine etching process by cleaning the wafer for several hours in a remover for optical resist (see appendix B.2). The scaling bar indicates 5 μm.

the 2DEG is finally defined is called *mesa*[1]. Again a PMMA based resist, structured by EBL, acts as a protection layer. For the etching process a diluted mixture of sulfuric acid and hydrogen peroxide is used.

A difficulty that occurred while wet-etching fine structures ($< 1\,\mu$m) into the 2DEG was the adhesion of the hydrophobic PMMA in the water-diluted acid. By using a standard cleaning process with eventually ultrasonic, acetone, IPA/ethanol the etching of fine structures was not satisfying. The result is shown in Fig. 3.3, left side. It seems as if the PMMA is slightly lifted and the mask got under-etched. For defining a mesa i. e. for a Hall bar this is not a limiting problem while for defining small structures in the range of μm we need a better process. This has been reached by cleaning the sample for several hours in a remover for optical resist (see appendix B.2). In addition, the resist thickness has been reduced from 600 to 200 nm in order to minimize the undercut. A test etched with this improved procedure is shown in Fig. 3.3 on the right side.

[1] *mesa* is the Spanish and Portuguese word for *table* and is used for elevated areas of land with a flat top and sides that are usually steep cliffs, similar to etched structures on a semiconductor substrate

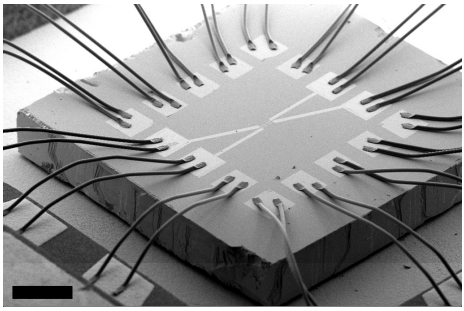

Figure 3.4: For an electrical transport measurement the sample is glued into and contacted to the chip carrier using an ultrasonic bonding-machine. The chip carrier has standard dimensions and fits into the measurement setup. e. g. a cryostat. The scaling bar indicates 500 μm.

3.1.6 Bonding

Ohmic contacts and gates on a wafer mounted in a chip carrier are contacted to the measurement setup by bonding. In this procedure a 20 μm thick aluminum-wire is attached to chip carrier and wafer by an ultrasonic pulse. This method is limited to bonding pads in the size of 150 μm. Smaller contacts have to be contacted lithografically by defining a metal stripe that connects the contacts and ends up in a bonding pad, as it has been done for the small inner contacts of the MZ-interferometer (Ch. 6).

3.2 Schottky Contacts / Gates

The interface between a metal and a semiconductor is called a Schottky contact resp. barrier [42]. The bending of the bands due to the alignment of the electrochemical potential results in a barrier and a diode-like behavior of this interface. Applying negative voltages to the metal in respect to the grounded semiconductor increases the barrier whereas for a positive voltage a leakage current is flowing. Due to this property the electron density and hence the conductance in the underlying 2DEG can be controlled respect to a negative bias. Therefore, these contacts are often called *gates*.

Gates are produced by metalization. Usually gold is used due to its chemical inertia. In order to enhance the adhesion of gold, titanium is evaporated in a first, thin layer. For detailed process parameters see appendix B.4. Evaporating a metal over a wet-etched step of the mesa can be problematic. If the height of the evaporated gates is smaller than the height of the step,

there might be no continuous film and contact problems to the gates. This has to be overcome either by angle evaporation or by a second evaporation step at the critical point.

3.3 Ohmic Contacts

In order to perform transport experiments with 2DEGs in a GaAs/AlGaAs-heterostructure they have to be electronically contacted. Combining a semiconductor and a metal results in the already mentioned Schottky barrier. However, for transport measurements at low temperatures, low, Ohmic-like contact resistances are preferable. The barrier can be reduced by n-doping the semiconductor. This way the depletion width is decreased and the electron tunneling enhanced. For more information, see i. e. [43]. Very often *Ni*, *Au* and *Ge* are used to establish Ohmic contacts, *Ge* as a dopant and *Ni* to improve the diffusion process. These materials are evaporated onto the heterostructure and then annealed in order to diffuse in. The exact mechanisms of the diffusion process are still not understood in detail. We used different recipes, see appendix B.5.

For the positive cross-correlation experiment (Ch. 5) we used the standard cleaning process, recipe M1 for metalization and A1 for annealing. The contacts had side lengths around 300 μm and contact resistances of the order 0.5 - 3 kΩ.

For the second project, the electronic MZ-interferometer in the edge state regime (see Ch. 6 and Fig. 3.6), a small, reliably working, Ohmic contact (in the range of 1 μm side length) is needed. On the way of making them we started again with metalization recipe M1. After severe difficulties with contacts freezing out at low temperatures, we used recipe M2 (from [44]), where the germanium amount was increased compared to gold and the layer sequence had been changed. Using recipe M2 the contact resistances could be decreased by an order of magnitude. For contacts down to side lengths of 200 μm we used annealing recipe A2. However, by *reducing the size* of the contacts to the range of μm the contacts got very high resistive at low temperatures and mostly froze out.

A big improvement in reducing the contact resistances for small contacts at low temperatures was using metalization recipe M3 and additional cleaning after the oxygen plasma with a strong alkaline solvent[2]. In recipe M3 the ratio of Au and Ge layer was chosen such that it corresponds to that of the eutectic mixture $Au{:}Ge = 88\%{:}12\%$ (weight percent). For the amount of Ni the ratio $(Au+Ge)/Ni = 4$ gave good results. Recipe M3 is for contacting a 2DEG 120 nm below the surface. For 2DEG closer or further away from surface, the corresponding standard layer thickness for $Au/Ge/Ni$ has to be adjusted. With this recipe, contacts down to $1 \times 1\,\mu$m have been realized with contact resistances of several hundreds of Ohms at 4.2 K.

3.4 Bridges

Usually Ohmic contacts are designed in a size which is suitable to bond on, i. e. between 150 and 300 μm. The central part of the electrical MZ-interferometer (Ch. 6) has dimensions of about 5x5 μm^2 with a small Ohmic contact inside. This contact has a side length in the order of 1-2 μm. The connection of the small contact to the chip carrier and the measurement setup is established by a lithographically defined metal strip which links the small contact to a bonding pad. In the specific geometry of the electronic MZ-Interferometer, this metal strip has always to lead over a part of the 2DEG without influencing its density. A bridge-like structure over the 2DEG has to be produced. Two possible solutions have been tested. First we tried to hold the bridge by overexposed PMMA, finally we made completely freestanding bridges.

3.4.1 Bridges held by over-exposed PMMA

A realization of a metal bridge that has no direct contact with the wafer is shown in Fig. 3.5. The bridge is supported by a layer of over-exposed PMMA. The dose was increased gradually up to 10 times the dose used for "conventional" lithography in order to get rather a smooth than an abrupt slope. Although the metal-bridge was now several hundreds of nanometers

[2]Many thanks to Oktay Göktas and Jürgen Weis from the Max Planck Institut in Stuttgart for the fruitful discussions.

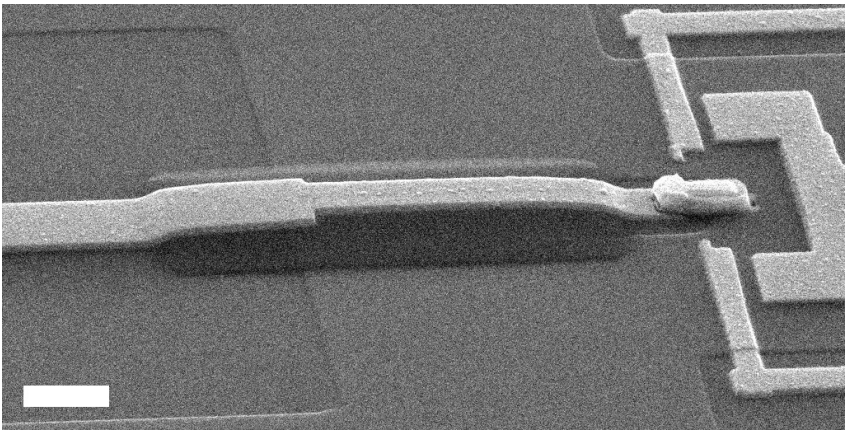

Figure 3.5: A small Ohmic contact to a 2DEG is connected by a metallic strip to a bonding pad. In order to prevent a direct contact of the metallic strip and the underlying 2DEG close to the semiconductor surface, a support layer of over-exposed PMMA has been fabricated. The over-exposition has been increased gradually in order to have a smooth slope. The scaling bar indicates 1 μm.

away from the 2DEG, the density of the 2DEG under the bridge was smaller than the 2D-"bulk"-density. The high dose used for the over-exposure might have modified the heterostructure. Another disadvantage could be the direct contact with the GaAs cap layer which influences the surface states and therefore the density. However, we cannot exclude that such PMMA-supported bridge technique would work with a 2DEG with higher mobility, since wet-etched structures with a lateral dimension of microns never showed ballistic transport in the edge state regime.

So we changed the 2DEG and decided to make completely free-standing bridges.

3.4.2 Free-standing Bridges

Simply dissolving the over-exposed PMMA in hot acetone was not possible. Methods as RIE cannot be used because of the delicate GaAs/GaAlAs-heterostructure.

Another idea was to use a a combination of negative and positive resists. The negative resist in order to produce a support layer for the bridge which will be removed afterwards. Tests either with UV-resist or with deep UV-resist exposed with the electron microscope, resulted in the similar problem as with the overexposed PMMA: It was impossible to dissolve it without damaging the heterostructure or the metal-bridge.

Finally, a technique was used to produce completely free-standing metal-bridges[3]. The basic idea is shown in Fig. 3.2 in the middle column. Instead of a single layer a double layer technique is used with two layers of different sensitivity. The first layer was PMMA with molecular weight of 950 K and the second the more sensitive PMMA-MA. The support layer as well as the pillars for the bridge can be written in a single exposure step. For the pillar the double layer structure is exposed such that all the resist is removed in the development process. Using half of the dose only the more sensitive PMMA-MA is washed out, while the underlying PMMA remains, the support layer for the bridge. In a subsequent metalization step an adhesion layer of titanium and a thick layer of gold were evaporated. PMMA and PMMA-MA are easily soluble in acetone and hence the following lift-off process is very unproblematic resulting in a free-standing gold bridge. This bridges have been used for contacting the small Ohmic contacts over the surrounding 2DEG as well as for the split-gates which can only be contacted from one side (see also Fig. 3.6).

3.5 Low Temperature Measurement Techniques

3.5.1 Why measuring at low temperatures?

Physical properties are usually related to a characteristic energy scale E_c. Hence in order to resolve the effect of interest, it should not be washed out by higher energies corresponding to temperature $k_B\theta$ or voltage bias eV. The characteristic energy one has to consider depends on the effect that is studied. In order to measure the quantum Hall effect in a two-dimensional electron gas, the temperature has to be smaller that the spacing of the

[3]Many thanks again to Oktay Göktas and Jürgen Weis from the Max Planck Institut in Stuttgart for the fruitful discussions.

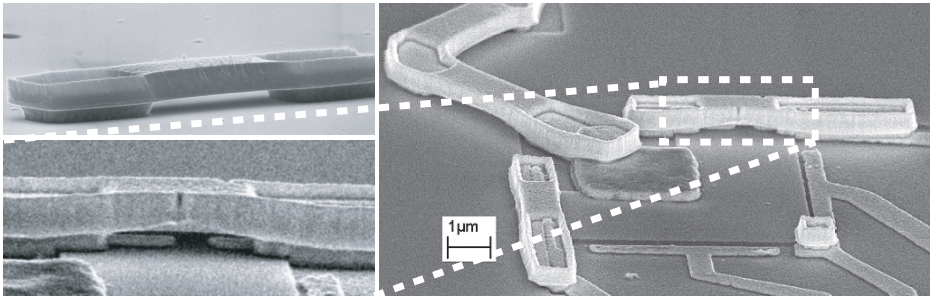

Figure 3.6: Realization of free standing gold bridges with the help of a double layer technique. *Upper left*: It is clearly visible that this bridges are free-standing. *Lower left*: In order to apply the same voltage on both sides of the split gates, they are connected by a free-standing bridge. *Right*: An electronic version of a Mach-Zehnder interferometer. Bridges are used for the connection of the small inner Ohmic contact as well as for the split gates.

Landau levels $\hbar\omega_c$ (sec. 2.5.2). In order to resolve the spin-splitting of the edge states, the temperature has to be consequently smaller than the Zeeman energy, super-conductivity takes only place for temperatures smaller than the binding energy of the Cooper pairs, etc.

A decrease of temperature also reduces the vibration in the lattice, i. e. the mobility of the electrons is increased by the reduction of phonon scattering.

The following description of cooling techniques follows the book of Pobell [45] where the reader is referred to for more details.

3.5.2 Evaporation Refrigerators

Evaporation cooling bases on the fact that energy is needed to overcome the intermolecular interactions in a liquid in order to transfer a molecule from the liquid to the gas phase. It is called the latent heat of evaporation L or the enthalpy of evaporation. Decreasing the pressure of the gas phase by a pump, leads to an enhanced evaporation of molecules out of the liquid in order to reach the saturation vapor pressure of equilibrium. The relation of vapor pressure p_{vap}, latent heat L and temperature θ is given

by $p_{vap} \propto \exp(-L/R\theta)$, where R is the universal gas constant [45]. I. e. the vapor pressure decreases rapidly with lower temperatures and higher latent heat. Additionally, the cooling power P_c is proportional to the amount of particles n leaving the liquid in a certain time which is proportional to the vapor pressure: $P_c \propto \exp(-1/\theta)$. I. e. a reduction of the vapor pressure decreases the temperature but the cooling power as well. This gives practical lower limits for temperatures reached by lowering the vapor pressure. For materials with higher latent heat the vapor pressure goes to zero much faster. For temperatures below 10 K only the isotopes ^3He and ^4He are suitable.

3.5.2.1 N_2

With liquid nitrogen at 1 bar temperatures can be reached down to its boiling point of 77.35 K. It is also used to cool the outer radiation shield in He-cryostats (see below). This considerably reduces the consumption of the more expensive helium.

3.5.2.2 ^4He

The boiling point of ^4He at a pressure of 1 bar is 4.21 K. Reducing the pressure by pumping results in boiling points up to a practical lower limit of 1.3 K due to the decreasing cooling power with lower temperature. A system using the boiling point of ^4He at a decreased pressure is called a ^4He-cryostat. The evaporated helium is collected by a recovery system and liquefied again.

3.5.2.3 ^3He

The other isotope of helium, ^3He, is much more rare and expensive and only used in completely closed systems. Its boiling point at a pressure of 1 bar is 3.19 K. The practical lower limit for a reduced pressure by pumping is 250 mK. This is used in a combination of a ^3He and ^4He-system, a so called ^3He-cryostat. It consist in a combination of a ^4He-system as described above which provides its lowest temperature at the 1K-pot. A

closed ^3He-system which is thermally decoupled from the helium reservoir at 4.2 K is thermally in contact with the 1K-pot at less than 2 K where the ^3He-gas condenses and fills the ^3He-pot. When all the ^3He of the closed system is condensed, it is pumped by a adsorption pump. It consists in a large cold area in the ^3He-system that adsorbs the ^3He-atoms in order to keep the pressure at a low value. Often charcoal is used. When the ^3He-pot is empty the system warms up to the temperature of the 1K-pot. Hence, this process is called a *single shot*. By heating up the adsorption pump to 40 K the ^3He-atoms are released and can be condensed again.

3.5.3 Dilution Refrigerator, $^3He/^4He$-mixture

As mentioned in the previous section, reaching lower temperatures than 250 mK by evaporation is limited by the rapidly decreasing cooling power for lower temperature which follows from the small vapor pressure at low temperatures due to the finite heat of evaporation.

Another technique, the so called dilution cooling, is used to enter the temperature range below 250 mK. It bases on the behavior of a mixture of $^3He/^4He$ at low temperatures. As shown in the phase diagram of a mixture of liquid ^3He and ^4He for a saturated vapor pressure (Fig. 3.7), below 867 mK the mixture starts to split in a ^3He-rich (concentrated) and ^3He-poor (diluted) phase. For temperatures below 100 mK the concentrated phase consist in almost 100 % ^3He while the diluted phase has a concentration of 6.6 %^3He[4]. The value of 6.6 % comes from an interplay of different effects. An *increase* of the binding energy of ^3He in ^4He is induced by magnetic interactions due to the nuclear magnetic moments of ^3He and density effects due to the larger zero-point motion of ^3He. A *decrease* of the binding energy comes from the Pauli principle the ^3He atoms have to obey. This finally results in an equal chemical potential of the concentrated and the diluted phase with 6.6 % ^3He.

The specific heat *per* ^3He *atom* is higher in the diluted phase, resulting in a heat of mixing or an enthalpy of mixing $\Delta H = H_d(\theta) - H_c(\theta)$. I. e. transferring ^3He atoms from the ^3He-rich to the ^3He-poor side leads to

[4]The concentration x_3 of ^3He is defined as $x_3 = \frac{n_3}{n_3+n_4}$, where n_a stands for the corresponding number of ^aHe atoms.

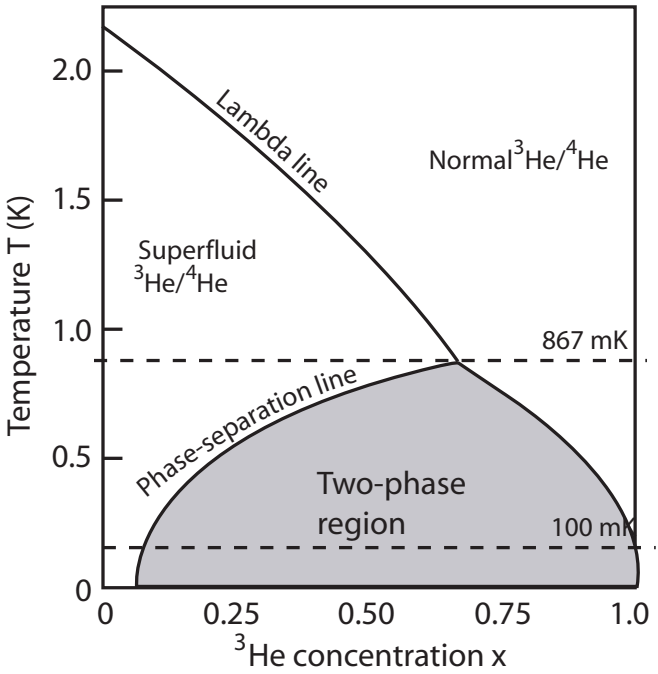

Figure 3.7: Phase diagram of a mixture of liquid ^3He and ^4He for saturated vapor pressure [45]. For temperatures below 867 mK the mixture starts to split in a ^3He-rich (concentrated) and ^3He-poor (diluted) phase. For temperatures below 100 mK the concentrated phase consist in almost 100 % ^3He while the diluted phase has a concentration of 6.6 %^3He. Because the specific heat *per* ^3He *atom* is higher in the diluted phase, transfering ^3He atoms from the concentrated to the diluted phase reduces the temperature of the system.

a cooling of the system which supplies the heat of mixing. This is similar to cooling by evaporation where the corresponding quantity is the latent heat of evaporation. The cooling power of dilution cooling is proportional to the product of the ^3He concentration in the diluted phase and the heat of mixing. Due to the finite concentration of ^3He in the diluted phase even at zero temperature the rate is not limited by the temperature as for the evaporation cooling. Secondly, the enthalpy of mixing is proportional to the temperature squared, i. e. $P_c \propto x_3\theta^2$. The cooling power of evaporation cooling is proportional to $\exp(-1/\theta)$. Comparing these two dependencies

it is clear that the dilution cooling is much more efficient for lower temperatures.

3.6 Setups

Two different types of setups in two different cryostats have been used for the two experiments. They will be described separately.

3.6.1 Cross Correlation measurement

The experiment described in Ch. 5 is a cross-correlation measurement carried out in a ^{3}He-cryostat at 290 mK. A schematics of the measurement setup is shown in Fig. 3.8. The sample is biased with a small current I injected at contact 1, provided by a DC-voltage source[5] and a high Ohmic resistor R ($\approx 1\,\mathrm{M}\Omega$) in series at 1.7 K close to the 1K-pot. The DC-voltage is stabilized by a RC-low-pass filter with a cut-off frequency of 1.85 Hz. All connections to the measurement rack are additionally filtered by LC-low-pass filters (π-*filters*). The current is divided by a beam-splitter geometry into two parts leaving the sample at the contacts 2 and 3. The time dependent current fluctuations $\Delta I_{\tilde{\alpha}}(t)$ ($\alpha = 2, 3$) are converted into voltage fluctuations $\Delta V_{\tilde{\alpha}}(t)$ over a resistor $R_{\tilde{\alpha}\alpha}$, $\Delta V_{\tilde{\alpha}}(t) = R_{\tilde{\alpha}\alpha}\Delta I_{\tilde{\alpha}}(t)$. Since the sample is a 2DEG in the edge state regime (Sec. 2.5.4), the current transport is chiral along the borders of the sample and the resistor $R_{\tilde{\alpha}\alpha}$ is realized in our experiment *on chip* by introducing additional Ohmic contacts $2, \tilde{2}$ and $3, \tilde{3}$: Contacts 2 and 3 are set to ground while the voltage fluctuations at contact $\tilde{\alpha}$, $\Delta V_{\tilde{\alpha}}(t)$, are recorded with respect to ground over the resistor $R_{\tilde{\alpha}\alpha}$, which is a combination of the *quantum resistance* at filling factor $\nu = 4$ and the contact resistance $R_{0,\alpha}$ in the range of 0.5 - 3 kΩ: $R_{\tilde{\alpha}\alpha} = h/4e^2 + R_{0,\alpha}$. In this measurement configuration no external resistors are used. This has the advantage that both of the potentials μ_2 and μ_3 are identically zero and that no current is re-injected from these contacts. The measured voltage fluctuations are detected by two low-noise

[5] Hewlett-Packard 3245A

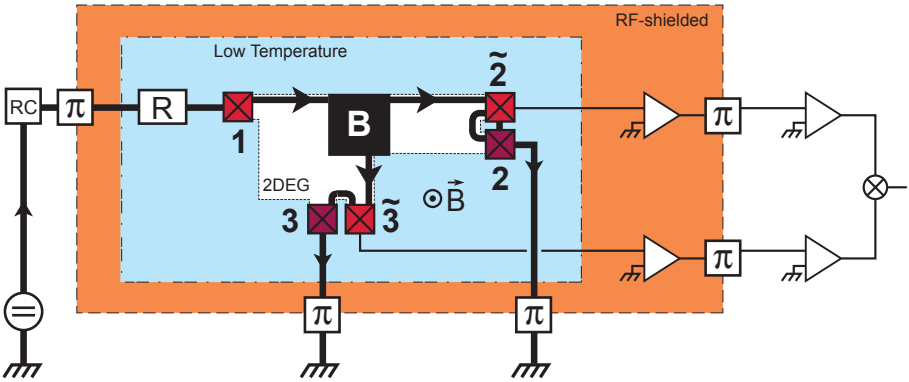

Figure 3.8: Schematics of the cross correlation measurement setup. A DC-current is injected in contact 1 and and split up to the leads 2 and 3. All connections to the RF-shielded regions are filtered with LC-low pass filters (π-filters). The current fluctuations are converted into voltage fluctuations over a resistor which is basically given by the quantum resistance of two spin-degenerate edge states. The voltage signal is amplified twice with a factor of 100 each, before read in a spectrum analyzer in oder to calculate the spectrum of the cross correlations of the voltage fluctuations.

amplifiers[6] in series, both fed by batteries. In each step the signal was amplified by a factor of 100 and finally read into a spectrum analyzer[7] that calculates the spectrum of the cross correlations of the voltage fluctuations at low frequencies.

The measurement lines are shielded and have a non-zero capacitance ($\approx$ 490 pF). This leads to a damping of the voltage fluctuations. In addition, we have an offset noise S_0 related to the current noise of the amplifiers. Both, the damping and the offset noise are determined by a *temperature calibration*: The power spectral density of the autocorrelation of the voltage fluctuations over a resistor R at temperature θ in equilibrium is $S_V = 4k_B\theta R$ (see also Eq. 2.43). Hence, S_V of a known resistor R is measured for different frequencies ν and temperatures θ. Plotting S_V for a fixed frequency against the temperature gives the offset S_0 (Fig. 3.9, upper part).

[6] NF Corporation LI-75A and Stanford Research Systems 560
[7] Vector Signal Analyzer Hewlett-Packard 89410A

Plotting $S_V/4k_B\theta R$ against frequency and fitting into the data the formula for the RC-damping of the amplitude $U_{\text{out}}/U_{\text{in}} = a/(1+(2\pi\nu RC)^2)$ with fitting parameter k and C gives the attenuation factor and the capacitance C (Fig. 3.9, lower part).

The correlation measurements have been performed at frequencies in the range from 20 to 70 kHz with typical bandwidths of 5 kHz. For lower frequencies $1/f$-noise is a limiting factor while for higher frequencies one is limited by the RC-cut-off (see Fig. 3.9).

The total offset of the current noise we measured was $S_I^{\text{offset}} = 3.13 \cdot 10^{-27}\,\text{A}^2\text{s}$. The current noise of the amplifiers was $S_{I,\theta=0}^{\text{offset}} = 3.91 \cdot 10^{-27}\,\text{A}^2\text{s}$ which we obtained from several temperature calibrations. From these two values the thermal cross correlation between the contacts 2 and 3 in equilibrium can be calculated $S_{I,23}(I=0) = S_I^{\text{offset}} - S_{I,\theta=0}^{\text{offset}} = -7.9 \cdot 10^{-28}\,\text{A}^2\text{s}$. This value is negative as one always would expect for thermal correlations (Eq. 3.6 in [28]) which are not related to the statistics of the charge carriers but follow from charge conservation. I. e. a charged particle emitted from reservoir α to reservoir β due to thermal activation, gives rise to an anti-correlated change of the corresponding potentials. The measured result is in quite good agreement with the theoretical value in Ref. [10][8]: $-k_B\theta G_0(3-T^2) = -8.8 \cdot 10^{-28}\,\text{A}^2\text{s}$ with $T_B^{\text{ii}} = 0$, $T_A^{\text{ii}} = T = 0.5$ and $\theta = 290\,\text{mK}$.

3.6.2 Electronic Mach-Zehnder interferometer

The measurement configuration of the experiment presented in Ch. 6 is shown in Fig. 3.10. The perpendicular magnetic field is set such that the electron transport is governed by one or two spin-polarized edge states. A current is injected by applying an AC bias of 1 to 5 μV at source $S1$ and setting the detectors $D3$ and $D4$ to ground. In order to measure the current at $D3$ we used a similar technique as in the correlation experiment (Ch. 5), i. e. we measured the voltage drop over the edge state between the contacts $\widetilde{D3}$ and D3. The resistance between these two contacts consists in the contact resistances in the range of $100\,\Omega$ and the quantum

[8] Eq. 13 therein with $R_1 = 1 - T_1 = 1 - T$

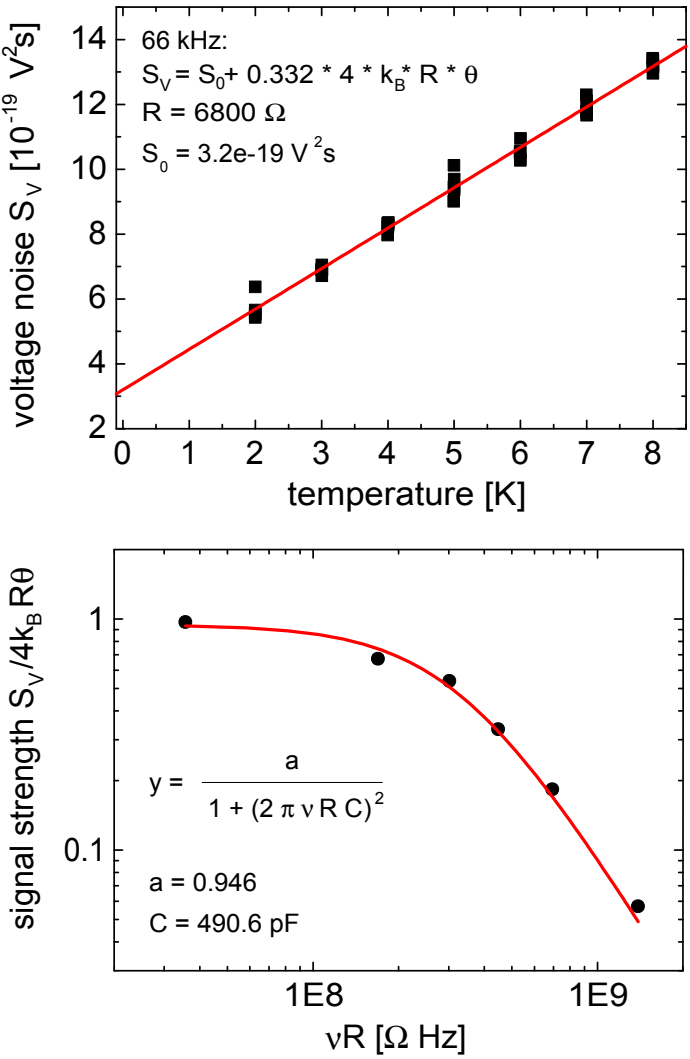

Figure 3.9: Temperature calibration: *Upper part*: From the measurement of the equilibrium voltage noise ($S_V = 4k_B\theta R$) of a known resistor R at different temperatures the offset noise of the amplifiers can be extracted. *Lower part*: Plotting the signal of the equilibrium voltage noise versus the product of frequency and resistance gives the capacitance C.

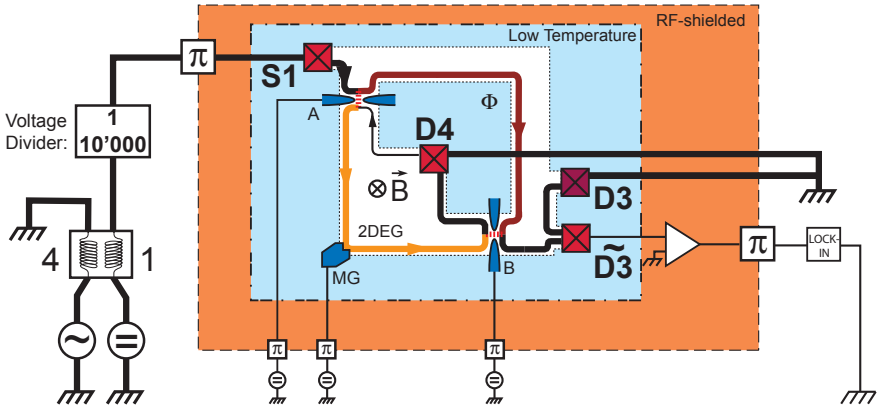

Figure 3.10: Schematics of the measurement setup. The current is induced by applying a bias eV at source $S1$ and setting the detectors $D3$ and $D4$ to ground. A negative DC bias is applied to the two beam splitters A and B and the side and modulation gates (SG/MG). The current flowing into $D3$ is detected by measuring the voltage drop over the edge state from $\widetilde{D3}$ to ground.

resistance of one ($25.8\,\mathrm{k\Omega}$) respectively two ($12.9\,\mathrm{k\Omega}$) spin polarized edge channels. Experimentally this has been realized by setting contact D3 to ground and measuring the potential at $\widetilde{D3}$ with respect to ground. The square root of the equilibrium noise power spectral density of the voltage fluctuations (Eq. 2.43) of a resistor $R = 13\,\mathrm{k\Omega}$ at temperature $\theta = 50\,\mathrm{mK}$ is smaller ($0.189\,\mathrm{nV}/\sqrt{\mathrm{Hz}}$) than the input noise of the voltage-amplifiers ($0.8\,\mathrm{nV}/\sqrt{\mathrm{Hz}}$). Additionally, for low contacts resistances, this technique has the advantage that there is only a small back-reflection of current from $D3$ to $S1$. By measuring the voltage drop over an external resistor attached to $D3$ this has to be taken into account. The signal is amplified by a factor of 1000 by an in-house build low-noise voltage amplifier (Fig. 3.11) at room temperature and read out with a lock-in detector[9].

[9]Stanford Research Systems 830

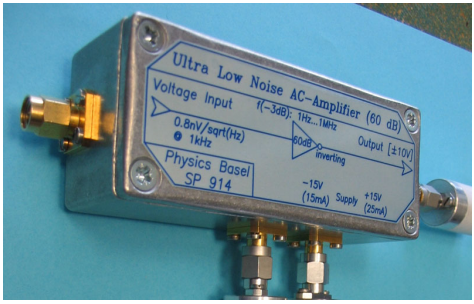

Figure 3.11: In-house build ultra low noise ac voltage amplifier with an input voltage noise of $0.85\,\mathrm{nV}/\sqrt{\mathrm{Hz}}$ and a gain of 1000.

4 Amplitude and Intensity Interferometry

This chapter is intended to introduce some concepts used in both of the next two chapters. We will focus on amplitude and intensity interferometry and their relations. The notion of interferometry is for many people connected with amplitude interferometry. As we will see in this chapter, there are possibilities of higher order interference.

However, any interferometry has the same basic concept: The *superposition principle* which follows from the Schrödinger equation for quantum mechanical wave functions as well as from the Maxwell equations for electromagnetic waves. It simply states that if we have two solutions of these equations then the sum of them is a solution as well. On the other hand this principle is not that visible in our daily life. Throwing stones onto a wall with two holes ends up with two hills of stones behind every hole. The only possible "transmission" processes for stones are *either* through hole 1 *or* through hole 2 but never through hole 1 *and* hole 2 at the same time. The question where the border is which allows to use the superposition principle or not led to famous cats as the one from Schrödinger[46–48]. The important point is the indistinguishablility of the two (or more) processes which is strongly related to the question of detection resp. interaction processes [49].

So let us consider a process[1] ψ_{12} which consist in two *indistinguishable* sub-processes ψ_1 and ψ_2 with a defined phase. The classical intensity or the quantum mechanical detection probability are obtained by $|\psi_{12}|^2$. As we will see, this quantity depends on the phase difference of the two sub-processes.

In the following two sections the argumentation will be along [50].

[1] The complex quantity ψ describes in the following either an electro-magnetic wave or a quantum mechanical wave function.

4.1 Amplitude Interferometry

In amplitude interferometry, a beam of incoming electro-magnetic waves or particles is split up into two possible paths described by their wave functions ψ_1 and ψ_2. If we do not make an experiment in order to determine which path has been taken, the wave function describing the process is the sum of both indistinguishable paths, $\psi_{12} = \psi_1 + \psi_2$. The intensity resp. probability I_{12} related to this process shows an interference pattern I_{int}:

$$I_{12} = |\psi_{12}|^2 = |\psi_1|^2 + |\psi_2|^2 + \underbrace{\psi_1^*\psi_2 + \psi_1\psi_2^*}_{I_{\text{int}}}. \tag{4.1}$$

For well defined phases of $\psi_1 = \alpha_1 e^{i\phi_1}$ and $\psi_2 = \alpha_2 e^{i\phi_2}$, the last two terms can be written as $I_{\text{int}} = 2\alpha_1\alpha_2\cos(\phi_2 - \phi_1)$, i. e. an interference pattern results as a function of the phase difference. The amplitudes are given by $\alpha_{1,2}$. If there is no defined phase relation, these two terms are averaged over the phase and we end up with the classical result, $I_{12} = |\psi_{12}|^2 = |\psi_1|^2 + |\psi_2|^2$, i. e. the sum of the probabilities of the processes 1 and 2.

An example of such an amplitude interferometer is the Michelson stellar interferometer. We will not focus on the not at all trivial experimental implementation, but concentrate on a simplified version (Fig. 4.1). Such interferometers are widely used in astronomy as e. g. the Very Large Array (VLA) in New Mexico, USA . In this simplified version the interferometer is just a double slit geometry with two slits 1 and 2 which let interfere the light of two point sources (e. g. stars) a and b. We are interested in their angular separation ρ. The amplitude of the electromagnetic waves of the two point sources in slit 1 is the sum of the contributions of both stars: $\psi_1 \propto \alpha e^{ikr_{1a}+i\phi_a} + \beta e^{ikr_{1b}+i\phi_b}$. The wave in the other slit 2 is correspondingly: $\psi_2 \propto \alpha e^{ikr_{2a}+i\phi_a} + \beta e^{ikr_{2b}+i\phi_b}$. The distance between star a and detector 1 is r_{1a} and due to the fact that both sources a and b are incoherent, i. e. there is no defined relation between their phases, we have to add a random phase ϕ_a. The wave number is given by $k = 2\pi/\lambda$. For the interference term $I_{\text{int}} = \psi_1^*\psi_2 + \psi_1\psi_2^*$ we get after averaging over the random phases:

$$\langle I_{\text{int}}\rangle = 2|\alpha|^2\cos(ik\Delta r_a) + 2|\beta|^2\cos(ik\Delta r_b), \tag{4.2}$$

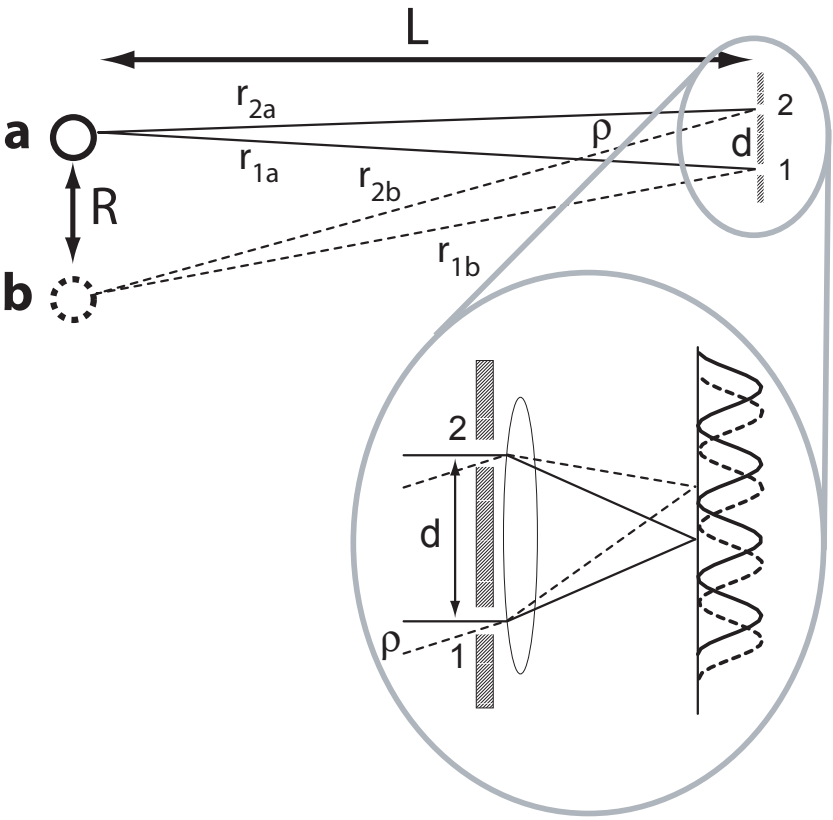

Figure 4.1: *Left*: Measurement configuration with two incoherent point sources (stars) spaced by R. The distance between the point sources and the detectors is $L \gg R$. *Right*: Simplified version of a Michelson stellar interferometer.

i. e. we have a sum of two independent interference pattern of two incoherent sources. Without loss of generality let us assume that source a is exactly in the axis of the interferometer, i. e. $\Delta r_a = r_{2a} - r_{1a} = 0$ and the angle separation between the sources is ρ. The distance between the two stars is R and the distance between stars and detector is $L \gg R$. Then the difference in the distances of source b to both slits is $\Delta r_b = r_{2b} - r_{1b} = \tan(\rho)d = R/L \cdot d = \rho \cdot d$. By altering the distance between the two detectors d, Δr_b is changed. This leads to a mutual shift of the two interference

pattern and a periodical decrease of contrast. For $k\Delta r_b = \pi = 2\pi/\lambda\Delta r_b$ they wash out maximally the first time. This corresponds to a separation of the two detectors of $d = \Delta r_b/\rho = \lambda/2\rho$. Increasing d further the two interference pattern are again "in phase" before washing out again.

With this technique the angular separation ρ can be determined between two point sources just by increasing the separation between the two interferometer slits d and observing the corresponding relative shift of the two interference pattern. This technique is also expanded to a detection of the angular diameter of one single source which can be treated as a sum of several point sources. In this case there is an overlap of much more interference pattern and the first time they all wash out and the contrast goes zero is for $d = 1.22\lambda/\rho$.

4.2 Intensity Interferometry

4.2.1 Electro-magnetic Waves

In the following the slit geometry is replaced by two detectors 1 and 2 at the former position of the slits. We still have two sources a and b far away from the detectors as in the previous section. For each detector the intensity is measured, for detector 1 we get

$$I_1 = |\psi_1|^2 = \underbrace{|\alpha|^2 + |\beta|^2}_{\langle I_1\rangle} + X \cdot e^{i(\phi_b - \phi_a)} + X^* \cdot e^{-i(\phi_b - \phi_a)}, \tag{4.3}$$

with $X = \alpha\beta^* \cdot e^{ik(r_{1a} - r_{1b})}$. Averaging over the random phases of the two incoherent sources a and b, we end up with the mean current $\langle I_1\rangle = \langle I_2\rangle = \langle|\alpha|^2\rangle + \langle|\beta|^2\rangle$ which is independent of any *geometrical* phases, i.e. independent of the distance of the detectors.

However, correlating the intensities of both detectors first and then averaging over the random phases gives the following interesting result:

$$\langle I_1 I_2\rangle \propto |\alpha|^4 + |\beta|^4 + 2|\alpha|^2|\beta|^2(1 + \cos(k(\Delta r_a - \Delta r_b))) \tag{4.4}$$

The same argumentation as in the discussion of the amplitude interferometer (Eq. 4.2) can be used again. The correlator of the intensities is

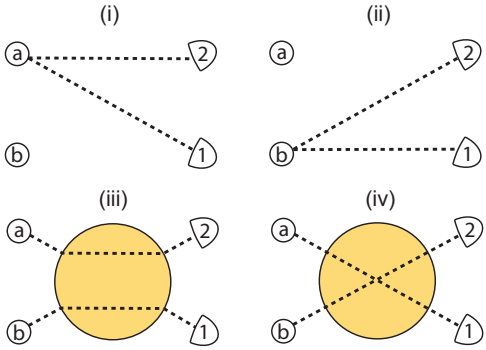

Figure 4.2: Four different different processes that contribute to a simultaneous detection of two photons at detectors 1 and 2. Processes (i) and (ii) can be distinguished, no interference pattern establishes and their contribution to a correlation measurement corresponds to the two first terms in Eq. 4.4. The processes (iii) and (iv) are quantum mechanically indistinguishable and contribute both with an amplitude proportional to $\propto e^{ik(r_{1a}+r_{2b})}$ resp. $\propto e^{ik(r_{1b}+r_{2a})}$.

varying if the two detectors are separated on the same length scale of $d = \Delta r_b/\rho = \lambda/2\rho$. Or in other words: The same information obtained by the amplitude interferometer is now obtained by a correlation measurement. This is not astonishing since the square root of interfering part I_{int} in Eq. 4.1 (averaged over the random phases) is proportional to the correlator $\langle I_1 I_2 \rangle$:

$$\langle I_{\text{int}}^2 \rangle \propto \underbrace{2\langle |\psi_1|^2 |\psi_2|^2 \rangle}_{2\langle I_1 I_2 \rangle} + \underbrace{\langle \psi_1^{*2} \psi_2^2 \rangle + \langle \psi_1^2 \psi_2^{*2} \rangle}_{\Rightarrow 0}. \tag{4.5}$$

4.2.2 Quantum Mechanical Particles

Up to now the interference in the intensity-intensity correlator has been treated for electro-magnetic waves. Quantum mechanical properties as the behavior of a many-particle wave function under exchange of two indistinguishable particles have not been used.

Let us have a look at Fig. 4.2. The simultaneous detection of two photons at detectors 1 and 2 can be divided in four different processes (i)-(iv) at the sources a and b: (i) and (ii): Two photons are emitted at source a or b and

detected at each detector. (iii) source a emits a photon detected in detector 2 and source b emits a photon detected in detector 1. (iv) source a emits a photon detected in detector 1 and source b emits a photon detected in detector 2. The first two processes can be distinguished, no interference pattern establishes and their contribution to a correlation measurement corresponds to the two first terms in Eq. 4.4. For the processes (iii) and (iv) it is different, they are quantum mechanically indistinguishable and contribute both with an amplitude proportional to $\propto e^{ik(r_{1a}+r_{2b})}$ resp. $\propto e^{ik(r_{1b}+r_{2a})}$. The superposition of this two possible processes gives rise to an interference term which corresponds to the cosine term in Eq. 4.4. The behavior of the many-particle wave function has also an influence on the distribution function of the occupied states $f(E)$. For particles that have a Fermionic distribution function as electrons an interference term is expected as well, however the signal in the two detectors will be anti-correlated. We will come back to this point in Sec. 4.4.

4.3 The Experiments by Hanbury Brown and Twiss

The Michelson stellar interferometer introduced in Sec. 4.1 has the drawback that it is very sensitive on processes as fluctuations of the atmosphere that strongly affect the phase relation of the waves at the two mirrors. Hanbury Brown and Twiss replaced the mirrors by photon detectors, measured the intensities at each detector and correlated them as described in the previous section. This way they determined in 1950 the angular size of radio wave sources as Cassiopeia A and Cygnus A. Intensity interferometry with radio waves which were understood as classical electro-magnetic fields was accepted at this time with an argumentation along Sec. 4.2.1. However, if this technique was also working for light sources which send out photons and where the particle picture has to be taken into account was not clear at this moment.

Hence before measuring the angular size of the star Sirius, Hanbury Brown and Twiss carried out a tabletop experiment where they used the light of a thermal light source, a mercury vapor lamp, and separated it into two beams by a half-silvered mirror [1]. With this technique they simply placed the two detectors at different places in the beam and by varying the distance between the detectors and the mirror the time separation τ was changed. They found for times smaller than the coherence time $\tau \ll \tau_c$ an enhanced correlation while for $\tau \gg \tau_c$ the events where completely uncorrelated. They measured a "bunching of photons", i.e. the fact that for photons emitted from an uncorrelated thermal source and measured at two close-by detectors, the probability to measure a photon in the second detector is enhanced when another one has been detected in the first one (within the coherence time resp. length). Both the photon bunching and the interference pattern stem from the same underlying fact, i.e. the symmetry of the many-particle bosonic wave-function which is symmetric under exchange of two particles, see also Sec. 4.4.

This fact was not very much accepted in the physical community and several experiments were carried out to disprove them, e. g. [51]. Aware that their tabletop experiment was working, Hanbury Brown and Twiss used their correlation technique to determine the angular size of a natural light source, the star Sirius, with a result of $0.0068'' \pm 0.0005''$ [2].

4.4 Hanbury Brown and Twiss Experiments with Electrons

As we have seen above, the Hanbury Brown and Twiss effect for particles emitted from a thermal light source can be derived in a classical electromagnetic wave picture or quantum mechanically as an interference of indistinguishable two-particle processes. In the quantum mechanical treatment the symmetry of the many-particle wave function goes in. As already mentioned by Feynman [52] one would expect a negative sign of the intensity-intensity correlations for fermionic particles.

Indeed, the correlation of the incoming events in two detectors is governed by the quantum statistical behavior of undistinguishable particles[28, 53], when not considering interactions. For particles with occupation numbers following Bose-Einstein-statistics as photons, the detection events are "in time" and the correlation is positive (*Photon Bunching*). For electrons, on the other side, the occupation is governed by Fermi-Dirac statistics and no two electrons are detected at the same time. Hence, the correlation of the signals is negative (*Electron Anti-Bunching*).

Let us have a closer look at the table top version of the Hanbury-Brown and Twiss experiment [1] and the outcome of similar experiments with electrons [6–9]. The basic configuration of such a device is shown in Fig. 4.3. The particles are provided by a thermal light source or a degenerate electron reservoir. The cross-correlation of the events in the two detectors, taking into account the Fermionic resp. Bosonic aspects, is (Eq. (1.6) of Ref. [28]):

$$\langle \Delta n_T \Delta n_R \rangle = \mp 2T(E)(1 - T(E))f^2(E) \tag{4.6}$$

The upper resp. lower sign stands for particles following Fermionic resp. Bosonic statistics, $T(E)$ is the transmission of the beam splitter at energy E and $f(E)$ is the corresponding distribution function of the mean occupation numbers in the incident beam. The energy dependent probability distribution of the occupation numbers is given by:

$$f(E) = \langle n \rangle = \frac{1}{\exp(\frac{E-\mu}{k_B\theta}) + a}, \tag{4.7}$$

where μ is the electro-chemical potential and the parameter a depends on the type of particles. $a = 0$ stands for classical particles while $a = \pm 1$ de-

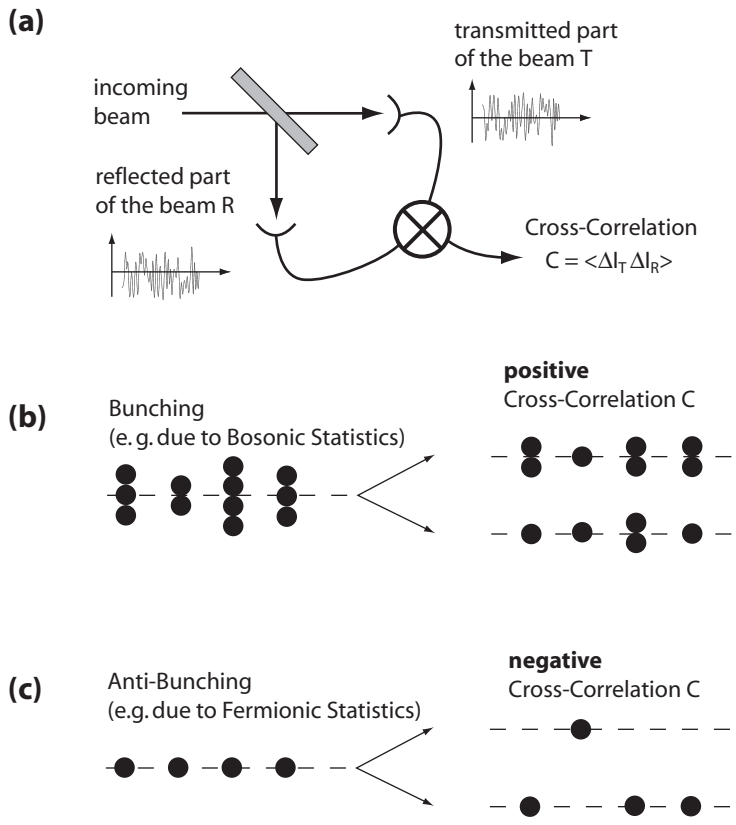

Figure 4.3: Basic setup for a correlation measurement with two detectors in a beam with small transverse coherence length. (a) Incoming beam is split up in a transmitted and reflected part. The fluctuations in both partial beams are recorded and correlated. (b, c): The sign of correlation depends on the statistics of the incoming particles.

scribes indistinguishable particles with Fermionic (upper sign) and Bosonic statistics (lower sign). The anti-symmetric Fermionic wave function leads to the Fermi-Dirac-distribution and the Pauli exclusion principle, i. e. zero probability to find two Fermions with the same quantum numbers. For Bosons, on the other hand, we get the Bose-Einstein distribution with an enhanced probability to find more than one particle in the same state.

The different statistics also show up in the fluctuations of the incoming beam. For the variance we get:

$$\langle \Delta n^2 \rangle \equiv \langle n^2 \rangle - \langle n \rangle^2 = \langle n \rangle (1 - a\langle n \rangle) = f(1 - af). \tag{4.8}$$

Hence, for a Fermi distribution the variance is smaller than the mean value: $\langle \Delta n^2 \rangle = \langle n \rangle - \langle n \rangle^2$ and goes to zero for a fully occupied stream at low temperatures with $\langle n \rangle = 1$. For Bosons, on the other hand, the variance is higher than the mean value: $\langle \Delta n^2 \rangle = \langle n \rangle + \langle n \rangle^2$. This is summarized in

$$\langle n \rangle^2 = f^2 = \mp(\langle \Delta n^2 \rangle - \langle n \rangle). \tag{4.9}$$

Combining equations (4.6) and (4.9) we get following dependence of the cross correlations of the transmitted and reflected beam on the fluctuations of the incoming beam:

$$\langle \Delta n_R \Delta n_T \rangle = T(E)R(E) \cdot (\langle \Delta n^2 \rangle - \langle n \rangle). \tag{4.10}$$

For an incoming stream of Fermions at low temperatures with no fluctuations, $\langle \Delta n^2 \rangle = 0$, we expect negative correlations, for a beam of Bosons positive ones. Finally, for an incoming beam of particles that are emitted completely independently, the occupation numbers follow Poissonian statistics, i. e. the variance is equal to the mean value and the correlation of transmitted and reflected part is zero.

In other words: For particles with Fermionic statistics in the incoming beam the simultaneous detection of a particle in any transmitted and reflected beam is *reduced in respect of an accidental coincidence* while for Bosonic statistics it is enhanced. Fermions *anti bunch* while Bosons *bunch*.

The dependence of the sign of the cross-correlation has also been measured experimentally. In the already mentioned table top experiment of HBT [1] positive correlations have been shown for photons. Corresponding experiments for electrons have been realized decades later in 1999 [6, 7] showing negative cross-correlations for electrons in a solid state environment. For free electrons this has been shown in 2002 [9]. The experiment of Henny et al. [6] uses a 2DEG in the edge state regime to implement electronic beams in a solid state environment. The occupation probability for an occupied state is 1 and 0 for an empty state. In an additional experiment, Oberholzer et al. [8] diluted the incoming stream ending up with a Poissonian

distribution of the electrons for small transmission. As expected by Eq. (4.10) the cross correlation went to zero.

4.5 Electron "Bunching" and Two-electron Interferometry

A general result of Ref. [28] is that for only taking into account the quantum statistical behavior, the cross-correlations of the current fluctuations in a multi-terminal Fermionic conductor are always negative. In this consideration no interactions between the particles have been taken into account. It is therefore interesting to ask which mechanisms could change the sign of the cross-correlations. In chapter 5 the first measurement of positive cross-correlation in a Fermionic environment is presented [11].

There are two effects in the intensity-intensity correlation experiments based on the same fundamental background which is the symmetry of a multi-particle wave function under exchange of indistinguishable identical particles [12]: (i) The sign of the correlation depends on the statistics the particles obey. This has been experimentally shown [1, 6–9, 54]. (ii) There is a two-particle *interference* effect in the intensity-intensity correlations which is not seen in the intensity itself. This has been experimentally shown for photons e. g. by measuring the angular size of Sirius by Hanbury Brown and Twiss [2] and meanwhile for electrons as well by Neder et al. [55].

The production of such a two-electron-interferometer along the lines of Ref. [12] was the original goal of this thesis. A building block of such a two-particle interferometer is a single-particle electronic Mach-Zehnder interferometer. Measurement on such a device [56] are presented in chapter 6.

5 Positive Cross Correlations in a Normal-Conducting Fermionic Beam Splitter

5.1 Introduction

5.1.1 Photon Bunching and Electron Antibunching

In the previous chapter it has been discussed that the cross correlations of the particle fluctuations in the out-going leads of a beam splitter configuration depend on the fluctuations in the incoming lead. These fluctuations are related to the distribution function f of the occupied states. The distribution function depends directly on the behavior of indistinguishable quantum particles under exchange. Furthermore it can be changed "manually" as shown in Ref. [8], i. e. by diluting the occupation of an incoming edge state by an additional gate. For photons the bunching effect is only measured for thermal sources, while for lasers the distribution function is Poissonian which corresponds to uncorrelated events at the beams splitter. For single photon sources the cross correlations are even negative.

5.1.2 Electron "Bunching"

The discussion in the previous chapter led to Eq. (4.6) which is a consequence of the exchange of indistinguishable quantum particles. Very often, transport can indeed be described by interaction free quasi-particles. Through interactions between the electrons, however, transport in different channels can become correlated in a positive way as well.

A beam splitter configuration to study such positive correlations in a normal-conducting environment has been proposed by Texier and Büttiker [10]. Two spin degenerate edge states serve as transport channels. Fluctuations in one channel are distributed on both channels by a controlled mixing

of the channels by inelastic scattering. This mixing can be switched on and off. In the following we will discuss the implementation of this proposal [11, 57].

Meanwhile, there are other experiments in normal-conducting devices showing positive cross correlations due to super-poissonian noise sources [58] or capacitive interaction between the electrons [59].

Furthermore, in beam splitter configurations with spin-selective detection, positive cross-correlations are expected as well. Electrons with opposite spins are not affected by exchange effects. Spin-selective correlation measurements should therefore be much more sensitive to interactions. Sauret et al. [60] discuss spin bunching for a normal-superconducting-junction and Cottet et al. [61] a three-terminal quantum dot with ferro-magnetic leads where a spin dependent bunching of electrons leads to positive cross correlations (dynamical spin blockade).

5.2 Sample

A simple sketch of the experimental setup is shown in Fig. 3.8. The samples act as a beam splitter that splits up the incoming beam from contact 1 into two beams exiting to contacts 2 and 3. A detailed overview over the realization of the beam splitter configuration as well as a scanning electron microscope picture is given in Fig. 5.1.

The samples are based on a 2DEG in a $GaAs/Al_{0.3}Ga_{0.7}As$ heterostructure 100 nm below the surface[1]. The 2DEG is contacted by four Ohmic contacts (1-4) and the electron transport is controlled by three gates. Gates A and B are quantum-point contacts (QPC) formed by metallic split gates (Fig. 5.1(c)). With gate C the contact to reservoir 4 can be tuned. For the experiment two conduction channels are required. With an electron density n_e of $1.5 \cdot 10^{11}\,\mathrm{cm}^2$, two spin-degenerate edge states (filling factor $\nu = 4$) correspond to a magnetic field of 1.6 T. The mobility at zero magnetic field was 380'000 $\mathrm{Vs/cm}^2$. The outer edge state is denoted with subscript (i), the

[1] The heterostructures have been grown by M. Giovannini from the group of J. Faist, University of Neuchâtel, Switzerland

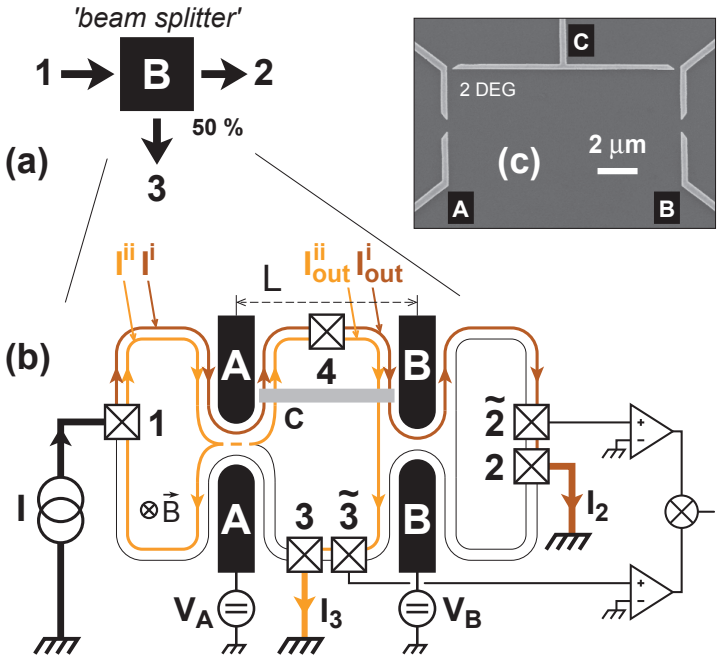

Figure 5.1: (a): The entire sample can be seen as a beam splitter: The injected current is split up in two parts with 50 % each. (b): Detailed schematics of the sample and measurement setup. (c) Scanning electron mircoscope picture of sample.

inner one with with (ii). Edge state (ii) will be pinched off first by applying a negative voltage to the gates A,B or C.

In former experiments with only one single spin-degenerate edge state and no additional reservoir 4, it has been shown that the partitioning of such a beam of Fermionic particles leads always to negative correlations between the transmitted and reflected beam [6, 8]. As we show below, inelastic scattering between the two transport channels in reservoir 4, can lead to positive correlations between the current fluctuations in contacts 2 and 3.

Working with two edge states, the QPC's are used for two different purposes. The transport in an edge state with transmission $T = 1$ is ballistic

and the current shows no fluctuations. Such a fully occupied transport channel is "noise free". By tuning the QPC's to transmission $T < 1$ we introduce current fluctuations by partitioning the current of the fully occupied incident beam from contact 1 in a transmitted beam with probability T and in a reflected beam with probability $1-T$. The power spectral density of the resulting current fluctuations ΔI is given by (see also Eq. 2.44) $\langle(\Delta I)^2\rangle_\omega = 2G_0T(1-T)\mu_1$. $G_0 = 2e^2/h$ is the conductance quantum of a spin-degenerate transmission mode and μ_1 is the potential of contact 1 while contacts 2 and 3 are set to ground ($\mu_2 = \mu_3 = 0$). Secondly, the QPC's can be adjusted such that exactly one of the two edge states is *completely* transmitted while the the other one is *completely* reflected which adds no noise to each beam. The main settings of the gates used in the experiment and their impact on the behavior of the edge states are shown in the left part of Fig. 5.2. They will be discussed below in more detail.

Adjusting gate B has been done in the following way (see Fig. 5.2(e)): Gate A is open and a current I is injected at contact 1 while the contacts 2 and 3 are set to ground. Hence for the total current one gets $I = I_2 + I_3 = (T_B^{\mathrm{i}} + T_B^{\mathrm{ii}})/2 + I_3$. The current in contact 3, $I_3/I = 1 - (T_B^{\mathrm{i}} + T_B^{\mathrm{ii}})/2$, is measured as a function of gate B and plotted in the inset. A plateau at $I_3/I = 1/2$ is clearly visible indicating that the second edge state (ii) is fully reflected ($T_B^{\mathrm{ii}} = 0$) while the first edge state (i) is still fully transmitted ($T_B^{\mathrm{i}} = 1$). The transmission of gate A is determined similarly.

Two samples with different spacings between the gates A and B, 200 and 14 μm, have been measured. They are denoted in the following with sample 1 and sample 2.

5.3 Measurement

5.3.1 Positive Cross Correlations

The settings for the gates in order to measure positive cross correlations are sketched in Fig. 5.2(a)): Gate A is tuned such that the first (i) edge state is transmitted completely ($T_A^{\mathrm{i}} = 1$) while the second (ii) edge state has an arbitrary transmission $0 \leq T_A^{\mathrm{ii}} \leq 1$. This leads to current fluctuations

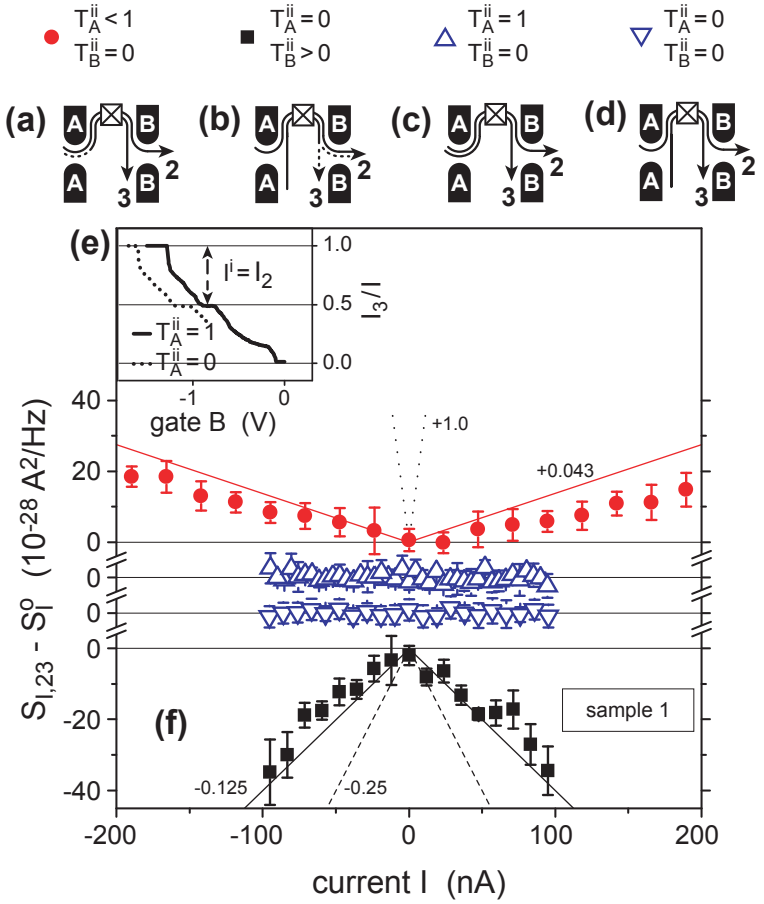

Figure 5.2: Sample 1 (Spacing between gates A and B: $\cong 200\mu$m). (a)-(d): Different settings for the gates A and B with the corresponding correlation measurements (f). Occupation of the two edge channels is not dependent on transmission of gate A, indicating the equilibration in reservoir 4.

ΔI^{ii} in this edge state which are characterized by their power spectral density $\langle(\Delta I^{\mathrm{ii}})^2\rangle_\omega = 2G_0 T_A^{\mathrm{ii}}(1-T_A^{\mathrm{ii}})\mu_1$. Gate C is open and both edge states enter the floating reservoir 4 with many modes. Due to inelastic scattering, current as well as current fluctuations are *equilibrated* between the two transport channels, i. e. the current fluctuations of the incoming, second edge state $\Delta I_{\mathrm{in}}^{\mathrm{ii}}$ are equally redistributed to both of the outgoing edge states

resulting in $\Delta I^{\rm ii}_{\rm in}/2 = \Delta I^{\rm ii}_{\rm out} = \Delta I^{\rm i}_{\rm out}$. In this configuration (Fig.5.2(a)) Gate B is adjusted such that it separates the two edge states (i) and (ii) and leads them to the contacts 2 and 3, respectively. The current fluctuations in the edge states (i) and (ii) stem from the same scattering process at gate A. Hence, the cross correlation between them is expected to be positive. Its power spectral density $\langle \Delta I_2 \Delta I_3 \rangle_\omega = \langle \Delta I^{\rm i}_{\rm out} \Delta I^{\rm ii}_{\rm out} \rangle_\omega = 1/4 \langle (\Delta I^{\rm ii}_{\rm in})^2 \rangle_\omega$ divided by the Poissonian value $2e|I|$ (Fano factor) gives [10]:

$$\frac{\langle \Delta I_2 \Delta I_3 \rangle_\omega}{2e|I|} = \frac{1}{4} \frac{\langle (\Delta I^{\rm ii}_{\rm in})^2 \rangle_\omega}{2e|I|} = +\frac{1}{4} \frac{T^{\rm ii}_A (1 - T^{\rm ii}_A)}{1 + T^{\rm ii}_A}. \tag{5.1}$$

$I = G_0 (1 + T^{\rm ii}_A) \mu_1 / e$ is the total current through the device (injected at contact 1 and led away at contacts 2 and 3).

Let us have a look on the measured data on sample 1 for gate C open. The results are shown in Fig. 5.2(f). Gate A is set in the way that the second edge state is transmitted with transmission $T^{\rm ii}_A \cong 1/2$. According to Eq. (5.1) the positive correlations have their maximal possible value for $T^{\rm ii}_A = \sqrt{2} - 1 = 0.414$, see also the discussion part (Sec. 5.4). We see indeed positive cross correlations (solid red circles in Fig. 5.2(f)). The solid line indicates the the maximal possible value given by Eq. 5.1 for $T^{\rm ii}_A = 0.41$. The dotted line in the same figure indicates the values for Poissonian noise $S_P = 2e|I|$.

5.3.2 Negative and Zero Cross Correlations

With the other three settings for the gates A and B, indicated in Fig. 5.2(b-d), the cross correlation between the reservoirs 2 and 3 can be changed to zero or negative values. Finite transmission of the second edge state at gate B ($0 < T^{\rm ii}_B < 1$) leads to negative correlations due to the fermionic particle nature [6, 8] of the electron (Fig. 5.2(b)). The maximal negative value $-\frac{1}{8} \cdot 2e|I|$ results for $T^{\rm ii}_B = 0.5$ and $T^{\rm ii}_A = 0$ or 1 (see also Eq. (5.2) in the discussion part). This is indicated in Fig. 5.2(f) with the solid black line, while the measured data are the solid black squares.

For transparencies $T^{\rm ii}_A, T^{\rm ii}_B \in \{0, 1\}$ (Fig. 5.2(c,d)) we always get zero cross correlations. The corresponding measurements are the blue triangles in

Fig. 5.2(f). The fully occupied edge states are either completely transmitted or completely reflected and hence, no fluctuations are induced. This indicates that inelastic scattering between two edge states alone does not introduce any noise in the system.

5.3.3 Switching the equilibration On and Off

It is interesting to ask what happens when gate C is closed and contact 4 is pinched off from the sample. This would prevent the two edge states from equilibrating therein. In Fig. 5.2(e) the current reflected from gate B to contact 3 is shown for gate C closed for sample 1 (with a spacing between gates A and B of 200 μm). It does not matter if gate A transmits one or two ($T_A^{\mathrm{ii}} = 0$ or 1) edge states, in any case we see a plateau at 50 % of the total current where gate B pinches off the second edge state. This is a strong indication for current redistribution between the two edge states along this path and it is in agreement with detailed studies on equilibration lengths in the quantum Hall regime [62, 63]. I. e. independently of pinching off reservoir 4 or not, there is always an equilibration between the two edge states for sample 1.

Therefore, a second device (sample 2) has been made where the distance between the two QPC's is much shorter (14 μm). For gate C closed no equilibration between the edge states takes place anymore. This has been measured the following way: In Fig. 5.3(a) gate C is open and the two edge states can *equilibrate* in contact 4 and carry the same current, independently of T_A^{ii}. In Fig. 5.3(b) gate C is closed and the edge states *cannot equilibrate* and the current in the second edge state (between gates A and B) depends on the transmission of gate A. This is seen again by measuring the reflected current in contact 3 for closing gate B. The position of the plateau correlates with the distribution of the total current I to the two edge states (after gate A).

This equilibration that shows up in the transport should also be visible in the noise. Fig. 5.3(d) presents measurements with $T_B^{\mathrm{ii}} = 0$ (edge states are separated at gate B and $T_A^{\mathrm{ii}} = 0.41$ (fluctuations are introduced at the second edge state). With equilibration in contact 4 (gate $C = 0.0\,\mathrm{V}$), the correlations are positive (solid red circles) and in good agreement with the

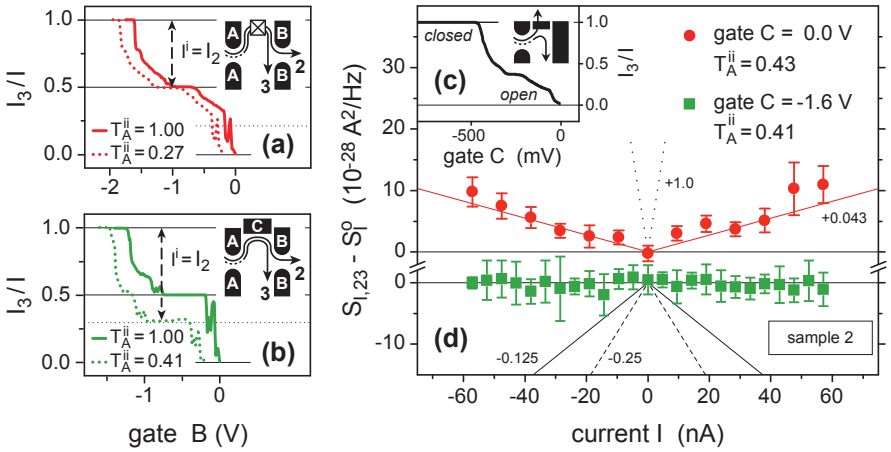

Figure 5.3: Sample 2 (Spacing between gates A and B: $\cong 14\mu$m): With the additional gate C the reservoir 4 can be pinched off (b) or not (a). Thus equilibration between the two edge states can be controlled and is seen in the occupation of the two channels (a, b) as well as in the current fluctuations (d).

maximal positive correlation. If gate C is closed, the first edge state remains noiseless ($\Delta I^{\mathrm{i}} = \Delta I_2 = 0$) and the correlator $\langle \Delta I^{\mathrm{i}} \Delta I^{\mathrm{ii}} \rangle_\omega = \langle \Delta I_2 \Delta I_3 \rangle_\omega$ vanishes (solid green squares). We thus have a "knob" which allows us to turn on and off the positive correlations.

5.4 Discussion

For zero temperature, $k\theta = 0$, the cross correlations between contacts 2 and 3 are described by (for a derivation, see Appendix A):

$$\frac{S_{I,23}}{2e|I|} = -\frac{\sum T_B^{\mathrm{n}}(1-T_B^{\mathrm{n}})}{2} + \frac{(\sum T_B^{\mathrm{n}})(2-\sum T_B^{\mathrm{n}})}{4} \cdot \frac{\sum T_A^{\mathrm{n}}(1-T_A^{\mathrm{n}})}{\sum T_A^{\mathrm{n}}}. \quad (5.2)$$

The first term describes the negative contributions due to partitioning the beam at gate B. They are maximally negative with $-1/8 \cdot 2e|I|$ for $T_{A/B}^{\mathrm{i}} = 1$ and $T_A^{\mathrm{ii}} = 0$ or 1 and $T_B^{\mathrm{ii}} = 1/2$. On the other hand we get the maximally positive value of $+(3/4 - 1/\sqrt{2}) \cdot 2e|I| \cong +0.043 \cdot 2e|I|$ for $T_A^{\mathrm{i}} = T_B^{\mathrm{i}} = 1$

(first edge state fully transmitted) and $T_B^{\mathrm{ii}} = 0$ (first and second edge state separated at gate B) and $T_A^{\mathrm{ii}} = \sqrt{2} - 1 = 0.414$.

5.4.1 Positive Correlations

In Fig. 5.4(a) an overview over the results for positive correlations are shown for the two samples 1 (solid boxes) and 2 (open boxes). The solid (red) line indicates the expected cross correlations for $T_B^{\mathrm{ii}} = 0$, which means that the edge states are completely separated at gate B. This can actually be set quite accurate by measuring the reflected current and setting the gate to the plateau. But already a small transmission of the second edge state at gate B can reduce the positive correlation drastically. As shown in the figure, a transmission of 2% ($T_B^{\mathrm{ii}} = 0.02$) leads to a reduction of 23% of the maximally positive value while for $T_B^{\mathrm{ii}} = 0.04$ we get a reduction of 45 % and for $T_B^{\mathrm{ii}} > 0.09$ the positive correlations vanish completely. This very sensitive dependence on the transmission of the second edge state at gate B might explain the deviations from theory.

If we assume that the first edge state is not fully transmitted at gate A e. g. with $T_A^{\mathrm{i}} = 0.96$ while the second edge state is nevertheless transmitted with $T_A^{\mathrm{ii}} = 0.41$ one can even get more positive correlations of $0.051 \cdot 2e|I|$.

5.4.2 Negative Correlations

Figs. 5.4(b) and (c) give an overview over the measurements of negative correlations. In Fig. 5.4(b) both edge states are transmitted at gate A, while for Fig. 5.4(c) it is only the first one, i. e. for $T_A^{\mathrm{i}} = 1$ or 0. The solid line indicates the result expected by the theory (Eq. 5.2 with $T_A^{\mathrm{i}} = 1$). As for the positive correlations the measured data does not exactly agree with theory. The dashed curves denote the changes that would occur due to additional scattering at the first QPC A, yielding a small positive contribution to the negative correlations [8]. However, the transmission at A equals 0 or 1 (open gate) with quite high precision ($\Delta T_A^{\mathrm{ii}} \leq 0.03$), and we think that the deviations observed here are related to nonequal transmissions of the two spin-polarized parts in the second edge state. The dotted lines in Figs. 5.4(b) and (c) are the negative correlations for 20%,

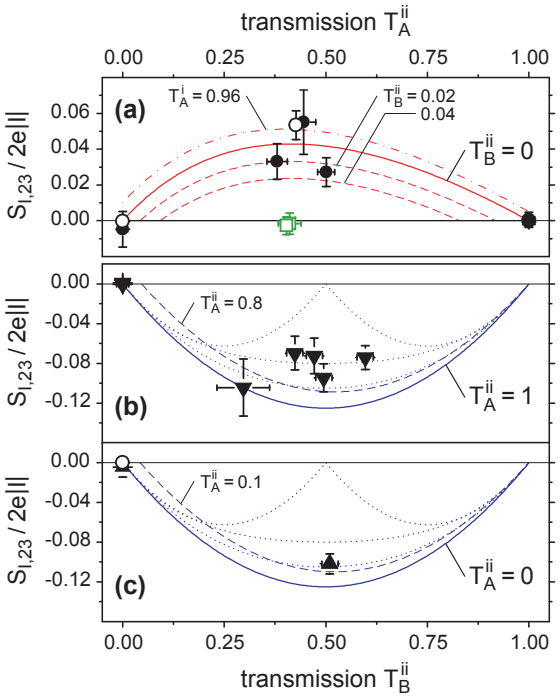

Figure 5.4: Discussion of the results for the two samples with spacing between the gates A and B of $\cong 200\,\mu$m (solid symbols) and $\cong 14\,\mu$m (open symbols). (a): Positive correlations can be reduced for not completely separating the two edge channels at gate B and even enhanced for a not fully transmitted first edge state at gate A (while the second one is transmitted with $T_A^{ii} = 0.41$). (b) and (c): Reduction of negative correlations due to an additional scattering at gate A or non-equal transmissions of the spin-polarized parts in the second edge state.

40%, and 100% unequal transmission (from bottom to top). For one spin-polarized edge state totally transmitted and the other totally reflected, the correlations would be zero for $\langle T_B^{ii} \rangle = 0.5$. From the data, we estimate that the differences between the two transmissions are on the order of 20% - 40% of $\langle T_B^{ii} \rangle$.

6 Electronic Mach-Zehnder Interferometer

6.1 Two-electron interferometer

In the previous two chapters we mentioned the experiments from Hanbury Brown and Twiss [1, 2] which introduced an intensity-interferometer that allows to determine the angular diameter of stellar objects. Let us remember the basic principle of a HBT-interferometer: The intensity of particles emitted by two independent sources are recorded in two detectors and then correlated. There are two effects based on the same fundamental background, i. e. the symmetry of a multi-particle wave function under exchange of indistinguishable identical particles [12]: (i) there is a two-particle interference effect in the intensity-intensity correlations which is not seen in the intensity itself. (ii) The sign of the correlation depends on the statistics the particles obey. Bosonic statistics gives positive intensity correlations which is often labeled as "bunching" while Fermionic statistics leads to "anti-bunching".

Around 40 years after the optical HBT-experiments which where published in 1956, electronic equivalents have been realized in a solid state environment (2DEG) [6–8] and a few years later in a free electron beam from a field emission source [9].

In these experiments an "anti-bunching" was measured due to the Fermionic statistics but *no* two-electron *interference* pattern. Using the building blocks of the successful realization of an electronic (single-particle) Mach-Zehnder interferometer with edge states by Ji et al. [13][1], Samuelsson et al. [12] proposed a two-electron interferometer (see Fig. 6.1). As in the Mach-Zehnder-interferometer, edge states in a 2DEG (Sec. 2.5.3) serve as electron beams

[1] For more details see Sec. 6.2.2 and Fig. 6.2

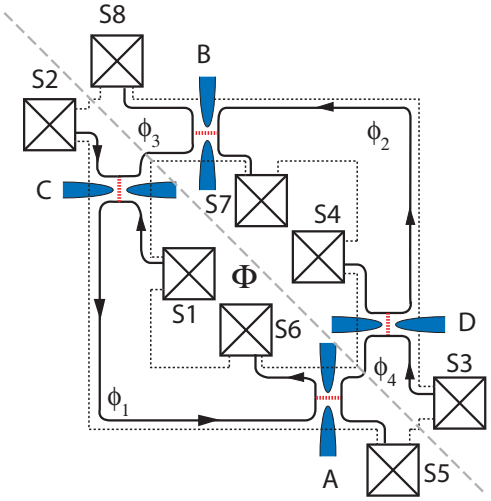

Figure 6.1: Two-electron interferometer after a proposal of Samuelsson et al. [12]. It principally consists in a combination of two Mach-Zehnder interferometers (Sec. 6.2.2 and Fig. 6.2), as indicated by the grey dashed line.

and the half-silvered mirrors[2] which serve as beam splitters in optical experiments are replaced by quantum point contacts (Sec. 2.3.2).

In Fig. 6.1 the proposal of Samuelsson et al. [12] is shown for the measurement of two-electron interference. It can be implemented in a 2DEG in the integer quantum Hall regime and consists in a combination of two electronic Mach-Zehnder interferometers which will be discussed in more detail in the next Sec. 6.2. In the proposed structure (Fig. 6.1), particles injected at contact α and leaving the device at contact β can take only one single path, *in contrast to* single-particle interferometers. In such a configuration *no* single-particle interference can be measured. The conductance G_{52} from contact 2 to contact 5 is simply given by the transmission probabilities of the beam splitters A and C, $G_{52} \propto T_A T_C$. On the other hand, the zero frequency cross-correlation $S_{\alpha\beta}$ of the current fluctuations ΔI_α and ΔI_β shows a *two-particle interference* pattern: For currents injected at the two sources $S2$ and $S3$, while all other reservoirs are set to ground and the QPC's have a transmission of $1/2$, it is given by ([12])

$$S_{58} = -(e^2/4h)|eV|[1 + \cos(\phi_1 + \phi_2 - \phi_3 - \phi_4)]. \tag{6.1}$$

[2] A glass-plate coated with a very thin metal layer such that 50 % of the intensity is transmitted and reflected.

ϕ_a denotes the phase accumulated along path $a = 1, 2, 3, 4$. For a simultaneous detection of one electron at contact 5 and another one at contact 8, two quantum-mechanically indistinguishable two-electron processes contribute: (i) One electron from 2 to 8 and one from 3 to 5 or (ii) one electron from 2 to 5 and one from 3 to 8. The amplitudes of these two processes are proportional to $\exp[i(\phi_3 + \phi_4)]$ and $\exp[i(\phi_1 + \phi_2)]$ which gives rise to the cosine-term in Eq. (6.1). Their phase difference can also be changed by a variation of the enclosed magnetic flux leading to a two-particle Aharonov-Bohm effect.

In a Mach-Zehnder interferometer, interference effects are already seen in the conductance while for the two-electron interferometer they only show up in intensity correlations. Compared to conductance measurements, correlation measurements are much more complex. The signal is much smaller which leads to time consuming averaging processes. In order to produce such a two-source electron interferometer the same technical challenges have to be overcome as for a single-particle Mach-Zehnder interferometer. These are e. g. the small working Ohmic contacts in the middle of the sample or the free-standing bridges (Sec. 3.3 and 3.4.2). Hence, in this thesis a Mach-Zehnder interferometer has been produced in a first step before realizing a two-source electron interferometer, which has meanwhile been implemented successfully by Neder et al. [55].

6.2 Optical and Electronic Mach-Zehnder Interferometers

6.2.1 Optical Mach-Zehnder Interferometer

Following the historical development we start with optical Mach-Zehnder interferometers, which owe their name to their inventors. The first Mach-Zehnder interferometers were build independently in the years 1891 and 1892 by Zehnder [64] and Mach [65]. A schematics is shown in Fig. 6.2. A monochromatic light beam emitted in source $S1$ is split up by a beam splitter[3] (A) in a transmitted and reflected part. These two beams are guided by additional mirrors ($M1$, $M2$) to a second beam splitter (B)

[3] E. g. a half-silvered mirror.

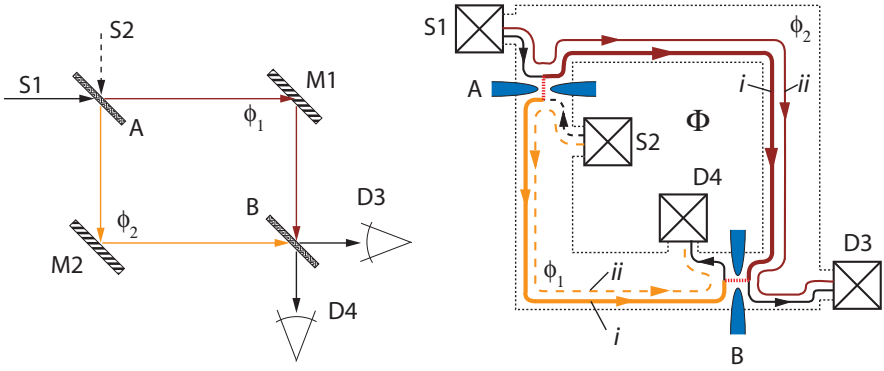

Figure 6.2: *Left*: Schematic view of an optical Mach-Zehnder interferometer. The monochromatic light beam emitted from source $S1$ is divided by the beam splitter A into a transmitted and reflected part. Guided by mirrors ($M1$, $M2$) the two parts are recombined at the second beam splitter B and again partitioned into the detectors $D3$ and $D4$. The intensity in $D3$ and $D4$ depends on the difference of the phases $\phi_{1,2}$ accumulated along the two paths. *Right*: Corresponding electronic Mach-Zehnder interferometer setup implemented in a two-dimensional electron gas defined within the dashed lines. Chiral edge states serve as electronic beams, quantum point contacts as beam splitters. Additionally, the sample is penetrated by a magnetic flux Φ leading to an additional Aharonov-Bohm phase [24] difference between the two paths. The situation is shown for filling factor $\nu = 2$ where interferometer is based on the outer edge state while the inner one is fully occupied in the upper arm and completely empty in the lower one.

where they are recombined. Finally, the intensity $I = |\psi|^2$ is measured in either detector $D3$ or $D4$. The complex amplitude ψ of the wave passing the interferometer is, in the coherent case, the sum over the amplitudes of the two paths 1 and 2. The scattering process at the beam splitters A and B can be described by the following unitarian scattering matrix (for the scattering approach also see Sec. 2.4.3) which links the two in- and

outgoing beams of the splitter[4]:

$$s_k = \begin{pmatrix} \sqrt{T_k} & i\sqrt{R_k} \\ i\sqrt{R_k} & \sqrt{T_k} \end{pmatrix}, \tag{6.2}$$

where T_k and $R_k = 1 - T_k$ are the transmission and reflection probabilities at beam splitters $k = A, B$. The amplitudes for the scattering processes from source $S1$ to detector $D3$ resp. $D4$ are given by the superposition of the two scattering processes through the paths 1 and 2:

$$\begin{aligned} s_{31} &= \sqrt{T_A T_B} e^{i\phi_1} - \sqrt{R_A R_B} e^{i\phi_2} \\ s_{41} &= i\sqrt{T_A R_B} e^{i\phi_1} + i\sqrt{T_B R_A} e^{i\phi_2}. \end{aligned} \tag{6.3}$$

The intensity respectively the particle current in the detectors is proportional to the total transmission. I. e. we get

$$I_{D3} \propto T_{31} = s_{31}^* s_{31} = T_A T_B + R_A R_B - 2 \cdot \sqrt{T_A T_B R_A R_B} \cos(\phi_1 - \phi_2) \tag{6.4}$$

and

$$I_{D4} \propto T_{41} = s_{41}^* s_{41} = T_A R_B + T_B R_A + 2 \cdot \sqrt{T_A T_B R_A R_B} \cos(\phi_1 - \phi_2). \tag{6.5}$$

Hence, the intensity in $D3$ and $D4$ is dependent on the difference of the phases accumulated along the two paths while the total intensity $I_{\text{tot}} = I_{D3} + I_{D4}$ is constant due to current conservation. In other words, by modulating the phase difference, an interference pattern in the intensity is measured.

6.2.1.1 Visibility of the Interference Pattern

The describing quantity of the interference pattern is its *visibility* $\hat{v}$, which is typically defined as the difference between the maximal and the minimal

[4]The formalism of the scattering matrices can be used for the half-silvered mirrors of the optical interferometer as well as for the quantum point contacts of the electronic version presented in Sec. 6.2.2.

signal divided by their sum. For a signal with a functional dependence as $I(\Delta\phi) = I_{\mathrm{mean}} + A \cdot \cos(\Delta\phi)$ we get:

$$\hat{v} = \frac{I_{\max} - I_{\min}}{I_{\max} + I_{\min}} = \frac{2 \cdot A}{2 \cdot I_{\mathrm{mean}}}. \tag{6.6}$$

Using Eqs. (6.4),(6.5) and (6.6), we get for a fully coherent interferometer the following visibilities in the detectors $D3$ and $D4$:

$$\hat{v}_{D3} = \frac{4\sqrt{T_A T_B R_A R_B}}{2 \cdot (T_A T_B + R_A R_B)} \quad ; \quad \hat{v}_{D4} = \frac{4\sqrt{T_A T_B R_A R_B}}{2 \cdot (T_A R_B + T_B R_A)}. \tag{6.7}$$

Using the definition of the visibility given above, i. e. dividing two times the amplitude A of the fluctuation part of the current by two times its mean value I_{mean}, gives the unsatisfactory result that we get different visibilities for the same interferometer when measuring the current in different detectors $D3$ or $D4$ due to their in general different mean current[5] but not due to any decoherence process.

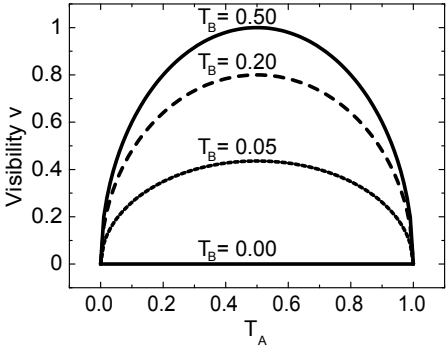

Figure 6.3: The visibility of a coherent interferometer as a function of the transmissions of the point contacts: $v = 4\sqrt{T_A T_B R_A R_B}$. Around its maximal value for $T_A = T_B = 1/2$ the visibility is relatively stable compared to the fast decay for nearly open or closed point contacts.

That is why we divide *in the following* two times the amplitude A of the fluctuating part of the signal by the total *injected* current $I_{\mathrm{tot}} = I_{\mathrm{mean},3} + I_{\mathrm{mean},4}$ in order to get a detector independent visibility of the interferometer:

$$\begin{aligned} v(T_A, T_B) = v_{D3} = v_{D4} &= \frac{4 \cdot \sqrt{T_A T_B R_A R_B}}{T_A T_B + R_A R_B + T_A R_B + T_B R_A} = \\ &= 4 \cdot \sqrt{T_A T_B R_A R_B}. \end{aligned} \tag{6.8}$$

[5] Only if one of the two beam splitters has transmission $T = 1/2$, the mean currents are equal.

The dependence of the visibility of a *coherent* interferometer $v(T_A, T_B)$ on T_A and T_B is shown in Fig. 6.3. Even the visibility of a *coherent* interferometer is *reduced* for transmissions of the beam splitters $\neq 1/2$.

However we are interested in *degree of coherence* of the MZ-interferometer. Hence, in order to study an interferometer which is not fully coherent we define a measured visibility v^*, which is the product of the visibility $v(T_A, T_B)$ of a coherent interferometer and a factor η describing any kind of loss of coherence due to e. g. an applied DC bias V_{DC}, temperature θ, etc.

$$v^* = v(T_A, T_B) \cdot \eta(V_{DC}, \theta, ...). \tag{6.9}$$

We call this factor η the *intrinsic visibility*.

6.2.1.2 Historical Comment

The aim of Zehnder and Mach was to build an interferometer where they could study the change of the refraction index for different states of matter. They needed a spatial separation of the two paths such that e. g. their temperature can be set independently. This was not possible at that time with the interferometer of Jamin [66] which consists basically in two thick, parallel glass plates where the light is reflected on both sides of the plates (Fig. 6.4). The distance of the two paths depends on the thickness of the glass plates. Increasing its size makes the experimental realization more and more difficult. This problem has been overcome in the design of the Mach-Zehnder interferometer.

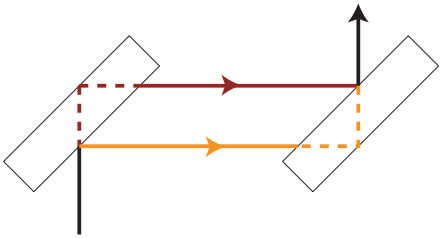

Figure 6.4: The Jamin Interferometer [66] consists basically in two thick, parallel glass plates where the light is reflected on both sides of the plates. The distance d of the two paths depends on the thickness of the glass plates.

6.2.2 Electronic Mach-Zehnder Interferometer

An electronic version of a Mach-Zehnder interferometer [13] serving the condition that the electrons traverse the interferometer only once is shown schematically in Fig. 6.2 and in a scanning electron microscope picture in Fig. 6.5. The edge states in a 2DEG at the interface of a GaAs/GaAlAs-heterostructure in a strong perpendicular magnetic field (Sec. 2.5.3) are the electronic equivalent to the light beams in the optical implementation. For the beam splitters, the half-silvered mirrors are replaced by quantum point contacts defined with split gates (Sec 3.2). Ohmic contacts to the 2DEG serve as electron sources and detectors (S1, S2, D3, D4) (Sec 3.3). They can be viewed as electron reservoirs with many modes coupled to this few mode conductor in the edge state regime.

Unlike the optical version, the electronic one with an area A perpendicular to a magnetic field B, is penetrated by the magnetic flux $\Phi = BA$. Increasing or decreasing the flux by one flux quantum h/e changes the phase difference between the two paths enclosing the area A exactly by 2π (Sec. 2.6 and Ref. [24]). This gives the possibility to study the interference pattern by smoothly changing the magnetic flux. The dimension of an electronic Mach-Zehnder interferometer is in the range of several microns. That is why changing the flux by h/e would require a control over the magnetic field in the range of the resolution of the current power supply of the magnet[6]. Hence two other methods were used to vary the flux: (i) a small change of the area induced by a *modulation gate* or (ii) using the decay of the magnetic field in the persistent mode which changes the flux in the range of h/e per hours. Method (i) is used to study the visibility of the oscillations while method (ii) is much too slow and serves mainly to connect the oscillations to the magnetic flux.

[6] For an area $A = 36\mu\text{m}^2$ a change of the magnetic field of $100\,\mu\text{T}$ varies the flux by one flux quantum h/e. Taking 100 points per oscillation would require a control of the magnetic field around 1 μT.

6.2.2.1 An Electronic Mach-Zehnder interferometer at Filling Factor $\nu = 2$.

All measurements in this chapter are carried out at filling factor $\nu = 2$, i. e. in a configuration with two spin-polarized edge channels. As in the previous chapter 5, the inner channel is labelled by (ii) and the outer one by (i). Oscillations have only been observed for partitioning the outer channel while this was not the case for partitioning the inner one. In this range both QPC's show up many resonances (Fig. 6.6).

The current, injected at contact 1 (I_1) and measured at contact 3 (I_3), has been detected by a bias modulation technique (see als 3.6.2) and can be written as follows where $\mu_1 = eV$ is the potential at contact 1 respect to ground ($\mu_3 = \mu_4 = 0$):

$$dI_1 = \frac{2e^2}{h}\frac{d\mu_1}{e} = \frac{2e^2}{h}dV \tag{6.10}$$

$$dI_3 = T_{31}dI_1 = \frac{2e^2}{h}\underbrace{(\frac{T_{31,i} + T_{31,ii}}{2})}_{T_{31}}dV \tag{6.11}$$

with $(x = i, ii)$

$$T_{31,x} = T_{A,x}T_{B,x} + R_{A,x}R_{B,x} - 2 \cdot \sqrt{T_{A,x}T_{B,x}R_{A,x}R_{B,x}}\cos(\Delta\phi). \tag{6.12}$$

In other words, the transmission T_{31} is calculated from the differential conductance $\frac{dI_3}{dV}$ as following:

$$T_{31} = \frac{T_{31,i} + T_{31,ii}}{2} = \frac{h}{2e^2} \cdot \frac{dI_3}{dV} \tag{6.13}$$

One QPC completely closed

In the specific case for completely closing one QPC, e. g. QPC B ($T_{B,i} = T_{B,ii} = 0$) we get $T_{31,i} = 1 - T_{A,i}$, $T_{31,ii} = 1 - T_{A,ii}$, i. e.

$$T_{31} = \frac{1}{2}(T_{31,i} + T_{31,ii}) = 1 - \frac{(T_{A,i} + T_{A,ii})}{2} = 1 - T_A. \tag{6.14}$$

The situation when QPC A is completely closed is described by exchanging A and B.

Partitioning the outer edge channel i, pinching off the inner edge channel ii

In the specific case for partitioning the outer channel i while pinching off the inner one ($T_{A,ii} = T_{B,ii} = 0, T_{31,ii} = 1$) we get

$$\langle T_{31,i} \rangle = T_{A,i}T_{B,i} + (1 - T_{A,i})(1 - T_{B,i}) \quad (6.15)$$

$$T_{31,i} = 2 \cdot T_{31} - 1. \quad (6.16)$$

This is the configuration for all measurements in this chapter.

6.2.2.2 Loss of Phase Coherence

A decrease or a loss of phase coherence due to interactions with the environment is equal to an averaging over the phase and has an influence on the interference term of the intensity. The averaging depends on the frequency of the perturbation. We deal with *phase averaging* if the single transmission events are still coherent, but the relative phase is randomized between them. In such a regime, the measurement in Ref. [16] are carried out. A random change of the phase difference $\delta\phi$ results in random fluctuations of the signal with the same magnitude as without phase averaging, hence a "visibility" can still be defined.

On the other side, we have complete *dephasing* or *decoherence* if the phase difference is not defined for a single transmission event.

The paths of our interferometer have a length L of approximately $15\,\mu$m. The drift velocity v_D in edge states is around 50'000 m/s [67]. The dwell time τ_d of an electron in the interferometer is $\tau_d = L/v_D \approx 0.3$ ns. This corresponds to a frequency of $\tau_d^{-1} = 3.3$ GHz. The measurement is however much slower. The averaging of the lock-in amplifier is given by the chosen time constant of 100 ms, we average over $300 \cdot 10^6$ electrons for one measurement point.

6.2.3 Visibility of a Asymmetric Coherent Interferometer

The assumption of a completely monochromatic beam of electrons is not realistic. Finite temperature and bias always result in electrons with energies E away from the Fermi level E_F (see Ref. [68]). Such electrons acquire an additional energy dependent phase $\Delta\phi \approx (L_\mathrm{i}/\hbar v_D)E$ along each path L_i, where v_D stands for the drift velocity of the electrons. For an interferometer with a path length difference ΔL this results in a dependence of the phase difference on applied bias eV and temperature θ. That is why, even for a fully coherent interferometer, a reduction in the visibility is expected with finite bias and temperature. The characteristic energy scale on which a decay of the visibility is seen is related to the path length difference, $E_c = \hbar v_D/\Delta L$. The decay of the visibility for a fully coherent MZ-interferometer with path length difference ΔL is given by [68]:

$$\hat{v} = \frac{4\cdot\sqrt{T_A T_B R_A R_B}}{T_A R_B + T_B R_A} \times \underbrace{k_B\theta\pi \sinh^{-1}\left(\frac{k_B\theta\pi}{E_c}\right)}_{\to E_c \quad (\text{for } \theta\to 0)} \underbrace{\frac{1}{eV}\left|\sin\left(\frac{eV}{2E_c}\right)\right|}_{\to \frac{1}{2E_c} \quad (\text{for } V\to 0)}. \quad (6.17)$$

For a completely symmetric interferometer, where $E_c \gg k_B\theta, eV$, no reduction of the visibility is expected and Eq. (6.17) equals Eq. (6.7). Additionally, the differential visibility is expected to be independent on the applied bias.

In the calculations in Ref. [68] the loss of phase coherence is introduced theoretically by a dephasing voltage probe [37, 69–71]. It results in a multiplication of Eq. (6.17) with a bias independent factor that is 1 for no dephasing and 0 for complete dephasing.

6.3 Sample

In Fig. 6.5 an experimental realization of the theoretical proposal in Fig. 6.2 is shown. We use a two-dimensional electron gas at the interface of a GaAs/$Al_{0.3}Ga_{0.7}$As-heterostructure. It is situated 120 nm below the surface[7].

[7] The 2DEG has been provided by J. Weis from MPI Stuttgart, Germany

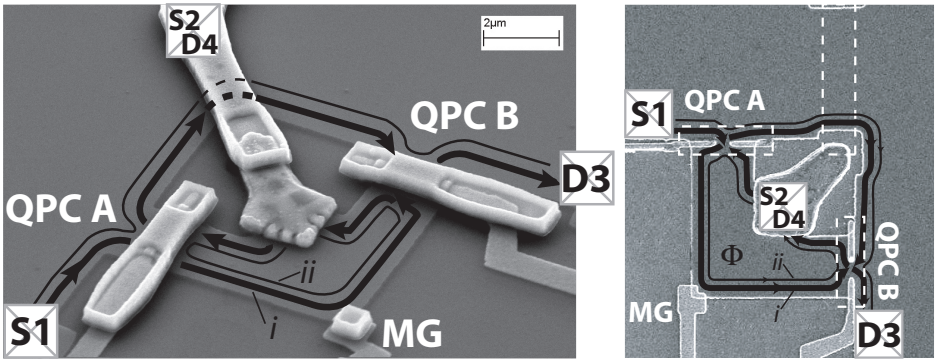

Figure 6.5: Scanning electron microscope picture of an electronic Mach-Zehnder interferometer realized in a two-dimensional electron gas. For a schematic figure see Fig. 6.2. *Left*: Side view with free-standing bridges. *Right*: Top view before evaporating the bridges (indicated by the dashed line). The two quantum point contacts A and B consisting in split gates connected by a free-standing bridge serve as beam splitters. Detector $D4$ is a small Ohmic contact in the center of the interferometer which is set to ground via another bridge. The area of the interferometer is slightly modulated by gate MG resulting in an magnetic flux dependent phase difference between the two paths.

The electron density is $1.6 \cdot 10^{11}\,\mathrm{cm}^{-2}$ and the mobility $1.7 \cdot 10^{6}\,\mathrm{cm}^2/\mathrm{Vs}$ at 4.2 K without illumination.

6.3.1 Ohmic Contacts and Mesa Definition

The 2DEG is connected to the measurement setup by Ohmic contacts (Sec. 3.3). Source $S1$ and detector $D3$ have a "conventional" size of $150 \times 200\,\mu$m where it is feasible to bond on (Sec. 3.1.6). Source $S2$ and detector $D4$ are situated in the center of the interferometer. They are realized by a single contact with a size of one micron. The production of reliable working contacts of this size is much more dependent on process parameters than bigger Ohmic contacts in the size of hundreds of μm (see also Sec. 3.3). Another challenge is to connect this small contact to the measurement setup. In order not to touch and influence the surrounding two-dimensional electron gas, this connection is established with a free-standing gold bridge

(see Sec. 3.4.2 and Fig. 6.5). The mesa has been defined by usual wet-etching technique (Sec. 3.1.5).

6.3.2 Gates

Beam splitters A and B have been realized by split gates or so called quantum point contacts, i. e. two metal electrodes that electrostatically form a barrier with a tunable transmission (Sec. 2.3.2). In order to apply the same potential on both sides of the split gates, they have been connected by a free-standing bridge (Sec. 3.4.2) made by the same technique and in the same step as the one connecting the small inner Ohmic contact (Sec 3.3).

The size of the area that is penetrated by the magnetic field is controlled by the modulation gate MG that slightly shifts the edge states. Changing the gate voltage by several millivolts alters the magnetic flux by h/e which corresponds to a full oscillation in the transmission of the interferometer.

6.4 Measurement

6.4.1 Quantum Point Contacts

A Mach-Zehnder interferometer consist basically in two beam splitters A and B. While the first one splits up the incoming beam into two parts, they are recombined again in the second one.

6.4.1.1 Characterization of the Quantum Point Contacts

In order to correctly adjust the quantum point contacts, their transmissions T_A and T_B has been measured independently (Fig. 6.6). The current is always injected in contact $S1$ while $D3$ and $D4$ are set to ground. For both QPC's open or closed, the total injected current directly flows from $S1$ to $D3$. On the other hand, for one QPC closed while keeping open the other one, the total injected current is directed from $S1$ to $D4$.

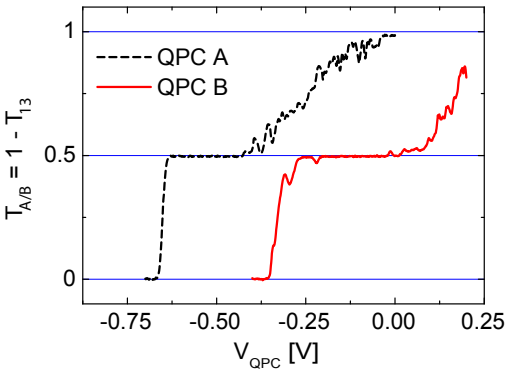

Figure 6.6: Transmission of the individual QPC's at filling factor $\nu = 2$. The transmission T_{31} from source to drain is recorded for either QPC A or B closed an connected to the individual transmissions by Eq. (6.14): $T_{A/B} = \frac{1}{2}(T_{A/B,i} + T_{A/B,ii}) = 1 - T_{31}$. On the plateau the inner (ii) spin polarized edge state is pinched off while the outer (i) one is transmitted. QPC B does not completely open for zero gate voltage.

Thus measuring the transmission T_{31} for either QPC A or B closed, gives the possibility to identify the individual transmissions of the QPC's. The determination of T_A for completely closed QPC B ($T_{B,i} = T_{B,ii} = 0$) follows from (Eq. 6.14): $T_A = 1 - T_{31}$. For QPC B the procedure is analogue. See Fig. 6.6.

In Fig. 6.7 the transmission of the QPC's is plotted only in the range were the inner channel is already reflected ($T_{A/B,ii} = 0$). Thus, the transmission of the gate corresponds with the transmission of the interferometer by $T_{A/B,i} = 1 - T_{31,i}$.

6.4.1.2 Dependence of Transmission of the Quantum Point Contacts on DC bias

The transmission of the two QPC's A and B is affected differently by an additional DC bias. (for the experimental setup see Sec. 3.6.2). QPC A is completely *independent* of the DC bias as shown in Fig. 6.7(a). On the other hand, the transmission of QPC B is *dependent* on the DC bias, as shown in Fig. 6.7(b). However, this dependence is constant over time as discussed in the next section.

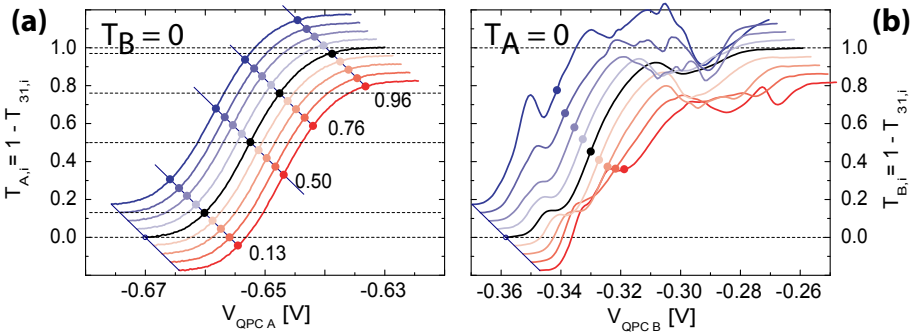

Figure 6.7: *(a)*: $T_{A,i}$ for different values of the DC bias between -40 (blue) and $+40$(red) μV in steps of 10 μV, indicating no DC dependence of QPC A. The curves are offset for clarity. *(b)* Same color scheme of $T_{B,i}$ for different DC bias voltages, again the curves are offset. Note that different to QPC A the transmission for a fixed gate voltage is *DC bias dependent*.

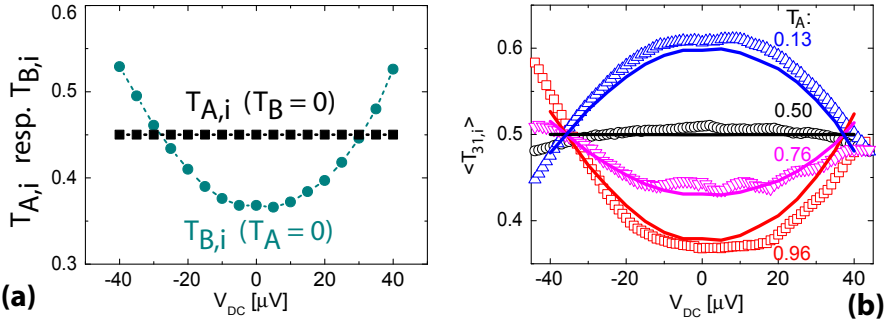

Figure 6.8: *(a):* Energy dependence of $T_{A,i}$ at $V_{QPCA} = -0.65$ V and $T_{B,i}$ at $V_{QPCB} = -0.33$ V. This values are determined from the data in Fig. 6.7. *(b):* Scattered symbols: Mean transmission $\langle T_{31,i} \rangle$ through the MZI as a function of bias voltage with the gate voltage of QPC B fixed to $V_{QPCB} = -0.33$ V and for different settings of QPC A corresponding to the transmissions T_A = 0.13, 0.5, 0.76 and 0.96. Solid lines: Calculated values using the data in Fig. 6.7(a) and (b) and Eq. 6.15.

6.4.1.3 Single QPC-Transmissions versus Mean Transmission of the Interferometer

In order to measure an interference pattern, both QPC's have been set to transmissions of the outer edge state $T_{A,i}$ and $T_{B,i}$ between 0 and 1. Doing so, we have no direct access anymore to the individual transmissions $T_{A,i}$ and $T_{B,i}$, but only to the mean transmission $\langle T_{31,i}\rangle = T_{A,i}T_{B,i} + (1 - T_{A,i})(1 - T_{B,i})$ as given in Eq. (6.15).

Hence we have to check the validity of Eq. (6.15) for various transmissions of the QPC's as well as for different DC biases. The procedure was the following:

1. The QPC's have been characterized by recording the individual transmissions $T_{A,i}$ as a function of gate voltage and applied DC bias while QPC B was closed followed by the analogue procedure for $T_{B,i}$ (as described in Sec. 6.4.1.1). The relation between transmission and applied gate voltage was DC bias independent for QPC A (Fig. 6.7(a)) while it was not the case for QPC B (Fig. 6.7(b)). This DC bias dependence of T_B for a fixed gate voltage of $V_{QPCB} = -0.33\,\mathrm{V}$ is exemplified in Fig. 6.8a. Please be aware that in Fig. 6.7 the transmission is plotted versus gate voltage while in Fig. 6.8 it is plotted versus DC bias!

2. In Fig. 6.8b the mean transmission $\langle T_{31,i}\rangle$ is plotted as a function of DC bias for four different transmissions of QPC A while the gate voltage of QPC B was held constant (-0.33 V). The scattered symbols are the measured $\langle T_{31,i}\rangle$ while for the solid lines the transmissions T_A and T_B have been separately determined (Fig. 6.7) and then combined by $\langle T_{31,i}\rangle = T_{A,i}T_{B,i} + (1 - T_{A,i})(1 - T_{B,i})$, showing clearly that the relation between gate voltage and transmission is defined even for gate settings ($0 < T_{A/B,i} < 1$) where we have no direct access to the individual transmissions.

   After doing so we have a simple way to access the transmission of QPC B for non-zero DC biases: $T_{B,i} = (\langle T_{31,i}\rangle - 1 + T_{A,i})/(2 \cdot T_{A,i} - 1)$.

6.4.2 Interference Pattern

Please note that in the following the inner edge channel (*ii*) is always pinched off and the gates are always set such that the transmissions for the outer edge channel (*i*) are $0 \leq T_{A/B,i} \leq 1$.

6.4.2.1 Oscillations in the Transmission of the Interferometer

The current in the outer edge state (*i*) of a completely coherent electronic MZ-interferometer is proportional to $I_{D3,i} \propto T_{31,i} = T_{A,i}T_{B,i} + R_{A,i}R_{B,i} - 2 \cdot \sqrt{T_{A,i}T_{B,i}R_{A,i}R_{B,i}} \cos(\Delta\phi)$, hence the transmission from $S1$ to $D3$ is a function of the phase difference $\Delta\phi$ between the lower and the upper arm. This phase difference depends on the geometry and on the magnetic flux enclosed by the two arms. A small variation of the modulation gate MG (see also Fig. 6.5) slightly shifts the edge state in the lower arm. This reduces the area A that is enclosed by the two interferometer arms and therefore the magnetic flux $\Phi = BA$ penetrating this area. For filling factor $\nu = 2$ the corresponding field is 3.55 T. The area A is approximately $37.5\,\mu\text{m}^2$ which gives a total flux of $BA = 1.33 \cdot 10^{-10}\,\text{Tm}^2$. The number of flux quanta h/e that contribute to the flux is $BA/(h/e) \approx 32000$. The area of one flux quantum at 3.55 T is $h/(eB) \approx 1200\,\text{nm}^2$. The transmission of the interferometer from $S1$ to $D3$ versus sweeping the modulation gate is shown in Fig. 6.9, top left. The period of one oscillation is about 35 mV.

The oscillations in the transmission are measured as a function of the modulation gate MG. In principle, the oscillations could also be due to an effect that only depends on a change of the electro-statical environment around the gate and not on a change of the magnetic flux itself. Not a proof but a strong hint that indeed the magnetic flux is changed, is the time evolution of the phase of the oscillations. This is shown Fig. 6.9, bottom, where the oscillations as a function of the modulation gate have been repeatedly measured for hours. The only quantity that alters slowly during this time is the magnetic field of the superconducting magnet in the persistent mode, which slowly decays in time. This leads to a slow change of magnetic flux and finally to a change of the phase of the interference pattern. A shift of the phase of 2π which corresponds to a reduction of the magnetic flux

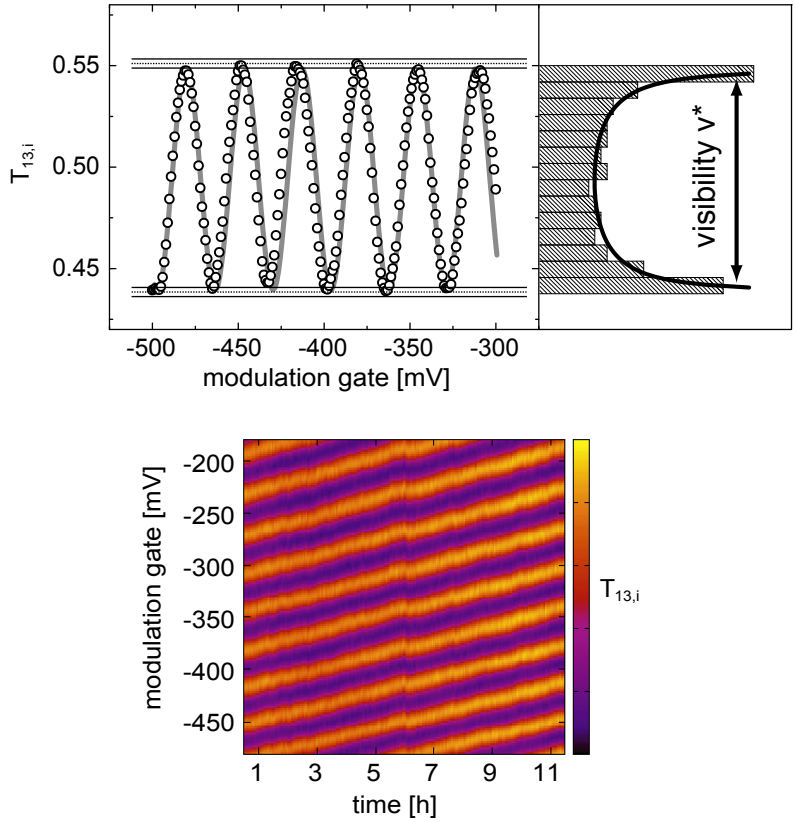

Figure 6.9: *Top, left*: Oscillations in the transmission in the outer edge state (i) from source $S1$ to detector $D3$ as a function of the modulation gate MG that decreases the enclosed magnetic flux between upper and lower arm of the interferometer and therefore changes the phase difference. One period is around 35 mV. *Top, right*: Determination of the amplitude of the oscillations. The histogram of the oscillating part of the current $I(x) = A \cdot \sin(x)$ is proportional to $h(y) = 1/(2\pi\sqrt{1-(y/A)^2})$ (red solid line). *Bottom*: Oscillations as a function of modulation gate *and* time. The slight shift in time corresponds to the decay of the magnetic field of the magnet in the persistent mode and is one flux quantum h/e (resp. a shift in the phase difference of 2π) per 6 hours. The phase of the interferometer is stable for hours.

by h/e takes approx. 6 hours. The magnetic field has to be changed by $h/(eA) \approx 110.2\,\mu$T in order to add or subtract a flux quantum. Hence, the

decay of the magnetic field is $18.4\,\mu T/\mathrm{h}$ which is a relative decay per day of $\Delta B/B = 1.24 \cdot 10^{-4}$. In Ref. [13] the decay rate was $120\,\mu T/\mathrm{h}$ at a field of 5.5 T while in Ref. [15] $20\,\mu T/\mathrm{h}$ at a field of 3.27 T has been reported.

6.4.2.2 Determination of the Visibility v^* of the Oscillations

Several methods have been tested in order to determine the amplitude of the oscillations in an automatic and systematic way. A first method was a least mean square fit of a sine function into the data. However, a least mean square fit is very sensitive to the starting values of the fitting parameters. Bad starting conditions make the fitting process very time consuming. In addition, a slight increase of the period of the oscillations due to a slight change of "effectiveness" of the modulation gate, i. e. the relation between gate voltage and change of the area of the interferometer, makes a fit even more difficult.

The second method used was fast Fourier transform (FFT). Its advantage is that it is very fast, however it requires a stable phase. Phase jumps or a slight change of period broadens the peak in the Fourier space which disturbs the determination of the amplitude. In addition, the number of recorded oscillations was often to small in order to get a sharp FFT-signal.

The most stable method in order to get the amplitude of the oscillations was to make a histogram of the oscillating part of the current $I(x) = A \cdot \sin(x)$. This gives the following form of the histogram:

$$h(y) \propto C \cdot \mathrm{d}(\arcsin(y/A))/\mathrm{d}y = C/(2\pi\sqrt{1-(y/A)^2}). \tag{6.18}$$

Fitting this formula into the histogram of the measurement data with fitting parameters C and A returns the amplitude A of the oscillations. Two times the amplitude A divided by the total AC current injected in one edge state, $I_{AC,\mathrm{tot}} = h/e^2 \cdot V_{AC}$ results in the measured visibility $v^* = 2A/I_{AC,\mathrm{tot}}$. See also Sec. 6.2.1.1.

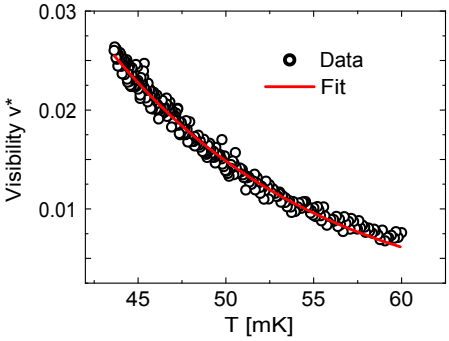

Figure 6.10: Fit of Eq. (6.17) onto the data of the dependence of the visibility on temperature. The fit results in a characteristic energy of $E_c = 4.1 \cdot 10^{-25}\,\mathrm{J} = 2.6\,\mu\mathrm{V} = 30\,\mathrm{mK}$.

6.4.2.3 Visibility versus Temperature

In Fig. 6.10 the temperature dependence of the amplitude of the oscillations is shown including a fit of Eq. 6.17 into the data. The applied AC bias has been fixed to $1\,\mu$V. However, increasing the AC bias up to $10\,\mu$V, the result for the characteristic energy was the same: $E_c = 4.1 \cdot 10^{-25}\,\mathrm{J} = 2.6\,\mu\mathrm{V} = 30\,\mathrm{mK}$. This would correspond to a path length difference [68] between $\Delta L = \hbar v_D / E_c = 2.6\,\mu\mathrm{m}$ ($v_D = 10'000\,\mathrm{m/s}$) and $13\,\mu\mathrm{m}$ ($v_D = 50'000\,\mathrm{m/s}$) [67].

6.4.2.4 Visibility versus DC Bias

Decay of Visibility v^* with Time at Positive DC Bias

In order to characterize the stability of the visibility v^* it has been measured as a function of time for constant DC biases. For positive DC bias voltages over $+40\,\mu$V the visibility decayed for staying at the DC voltage for a certain time (Fig. 6.11, left). This decay is enhanced for higher DC voltages. So all measurements versus DC bias have been done in the following way: Starting with $V_{DC} = 0\,\mu$V the DC bias has been changed symmetrically around $0\,\mu$V: 0, -1, +1, -2, +2, ..., -60, $+60\,\mu$V. After every measurement of visibility the DC voltage has been driven to $0\,\mu$V. The reason might be a heating effect or a change of T_A or T_B with time.

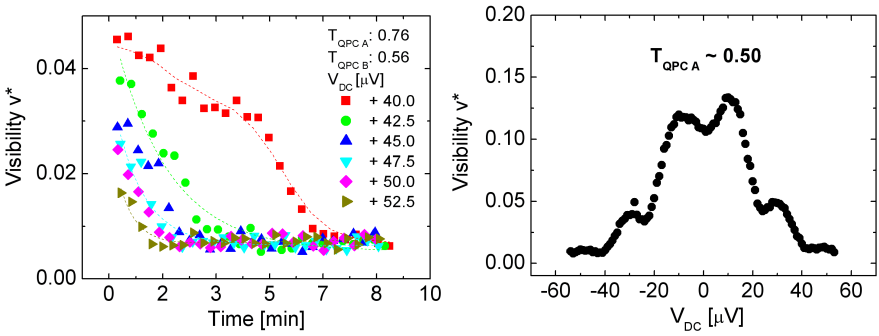

Figure 6.11: *Left:* For DC bias values higher than $+40\,\mu$V the visibility started to decrease with time. *Right:* DC bias dependence has been measured as follows: Starting with $V_{DC} = 0\,\mu$V the DC bias has been changed symmetrically around $0\,\mu$V: 0, -1, +1, -2, +2, ..., -60, $+60\,\mu$V. After every measurement of visibility the DC voltage has been driven to 0.

Decay of Visibility v^* with DC Bias

In Fig. 6.11, right side, a typical dependence of the measured visibility v^* on a symmetrically changed DC bias is shown. v^* decays with increasing negative and positive DC bias similar to the measurements reported in Refs. [13, 14, 72]. In Ref. [13], the decay of v^* with DC bias has no additional features. In Ref. [14], additionally to the decay, v^* shows a lobe structure, i. e. goes several times to zero and reappears again. In Ref. [72], v^* only one lobe has been seen. In our measurement there is an "attempt" of a lobe structure between 20 and $30\,\mu$V. In addition, v^* is not maximal for $V_{DC} = 0$. In order to study this behavior in more detail, we measured the dependence of v^* not only at transmissions $T \approx 1/2$ but in a wider range (Sec. 6.4.3).

Shift of Phase of the Oscillations with DC bias

In Fig. 6.12, a color plot of the oscillations as a function of DC bias is shown. The transmission of the point contacts was $T_A \approx 0.50$ and $T_B \approx 0.56$. For an increasing DC bias the phase of the oscillations shifts to lower values of the modulation gate. Different from Neder et al. [14], no phase jumps of

π are seen. This dependence of the phase shift on the DC bias does not change for different transmission of T_A. The phase is shifted by 2π for an change of DC bias of approx. $20\,\mu$V.

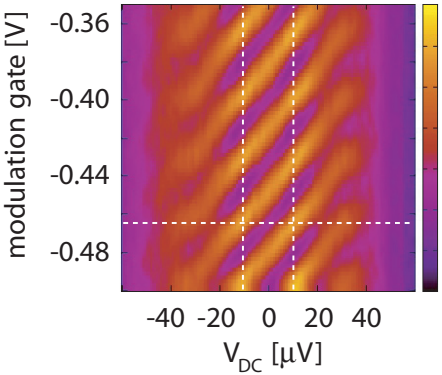

Figure 6.12: Color plot of the oscillations as a function of DC bias. Different from Neder et al. [14], no phase jumps of π are seen. The phase is shifted by 2π for an change of DC bias of approx. $20\,\mu$V. This dependence of the phase shift on the DC bias does not change for different transmission of T_A.

We can understand this as an electrostatic gating from the inner edge state to the outer one. The inner edge-state *ii* in the outer arm of the MZI is also biased to V_{DC} and electrostatically influences the chemical potential in the outer edge-state *i*, which is the one taking directly part in the interference. The electrostatic phase is the given by $\alpha 2eV_{gate}L/\hbar v_D$, where V_{gate} equals V_{DC}, $v_D = 10^4 - 5 \cdot 10^4\,\mathrm{m/s}$ is the drift velocity[67], $L = 15\,\mu$m the arm length of the interferometer, and α the gate coupling efficiency. With the measured values, our experiment is consistent with $\alpha = 0.14...0.75$ depending on the exact (but unknown) drift velocity. Because of the close-proximity of the edge states, a large coupling is plausible. The strong electric coupling between the edge-states may provide a channel for dephasing as proposed by Levkivskyi and Sukhorukov [73]. In their theory the excitations are dipolar and charged edge magnetoplasmons. This theory results in a dephasing rate which is inversely proportional to the temperature θ, which was confirmed recently [74]. A similar dependence was also derived for a single channel when screening was taken into account in a self-consistent manner [75]. In the latter model, dephasing is caused by intrinsic phase fluctuations, driven by the thermal bath. A related concept of intrinsic dephasing in a single channel has been put forward in two other papers recently [76, 77].

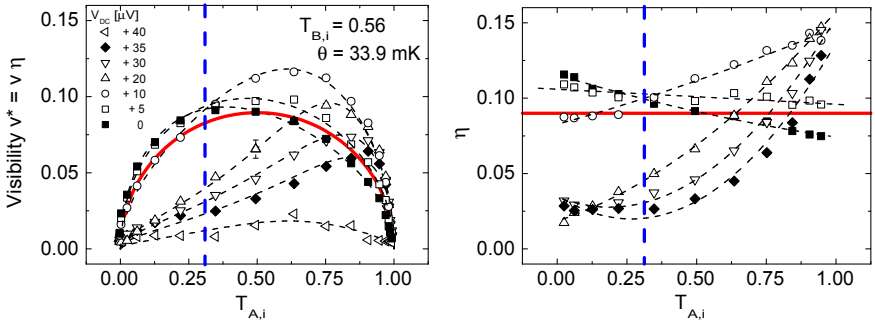

Figure 6.13: *Left*: The visibility v^* as a function of transmission of the first QPC $T_{A,i}$ and DC bias. QPC B was hold fixed at a transmission of $T_{B,i} = 0.56$. The red line (half circle) corresponds to a visibility $v(T_{A,i}, T_{B,i}) \propto \sqrt{T_{A,i}(1-T_{A,i})}$ and a constant intrinsic visibility η. The data is in qualitative agreement for 0 and $\pm 5\,\mu$V. For higher biases the maximum is shifted to the more open side of QPC A. A second feature is that also the *absolute* maximum of the visibility is higher for biases around $\pm 10\,\mu$V than at $0\,\mu$V. *Right*: The intrinsic visibility $\eta = v^*/v(T_{A,i}, T_{B,i})$ as a function of transmission $T_{A,i}$ and DC bias. The red line corresponds to the one in the left figure. η is increased in respect to the zero bias value for transmissions $T_{A,i}$ close to 1 (open QPC) and decreased for $T_{A,i}$ close to zero (closed QPC).

6.4.3 Dependence of the Oscillations on DC bias and Transmission of the QPC's

6.4.3.1 "Half circle"

The visibility v^* of the oscillations has been measured for different transmissions and DC biases. One QPC was held fixed while sweeping the transmission T of the other one from 0 to 1. This has been done for different DC voltages. One would expect a behavior of the visibility $v \propto \sqrt{T(1-T)}$ as shown in Fig. 6.3. In other words, one would expect a *constant* $\eta(T_{A,i}, T_{B,i})$ as a function of the QPC transmissions. However, QPC A and B behave differently. QPC B shows nearly the half-circle structure in v^* respectively an almost constant $\eta(T_{A,i}, T_{B,i})$ (Fig. 6.14). QPC A however shows such a dependence only for small biases. Increasing the bias shifts the maximum of the visibility from $T_{A,i} \approx 1/2$ to higher transmissions.

What do the two point contacts differ in? Taking into account the chirality of the edge states, QPC A is the first QPC which determines the occupation of the two interferometer arms. QPC B, on the other hand, determines how the current is partitioned into the detectors $D3$, resp. $D4$ (together with QPC A). Is this asymmetry a feature of a single QPC or it is a feature of a different dephasing in the two interferometer arms? A simple check is to reverse the magnetic field which changes the direction of transport in the edge states, which is done in the following subsection.

Another source of dephasing can be excluded: There might be an equilibration (heating) process for higher biases at the small inner contact $D4$ destroying the phase coherence. However, such a process would depend in the amount of current flowing into $D4$. But the dependence of the visibility on DC bias and QPC A qualitatively does *not* depend on the transmission of the second QPC B, as shown in Figs. 6.13 ($T_{B,i} = 0.56$), 6.15 ($T_{B,i} = 0.35 - 0.40$) and 6.16 ($T_{B,i} = 0.75$). I. e. it does *not* depend on the current flowing into the small inner detector $D4$.

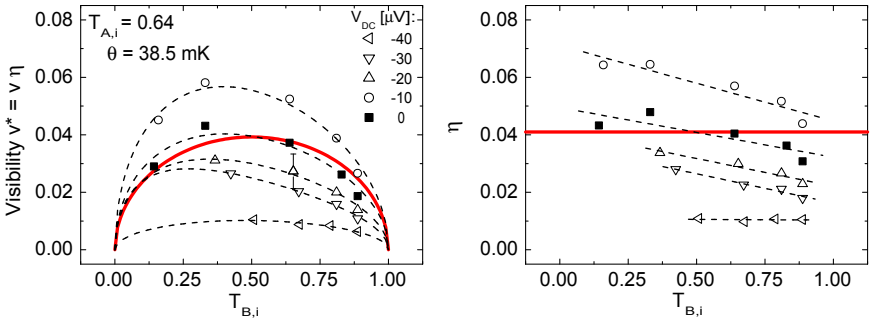

Figure 6.14: *Left*: The visibility as a function of the transmission the second QPC $T_{B,i}$ and DC bias. *Right*: The corresponding intrinsic visibility η.

Reversing the Magnetic Field

By driving the magnetic field from $+3.55\,\mathrm{T}$ to $-3.55\,\mathrm{T}$, transport is still governed by two spin-polarized edge states (filling factor $\nu = 2$). However, due to the chirality of the electron transport in magnetic fields, the k^+- and

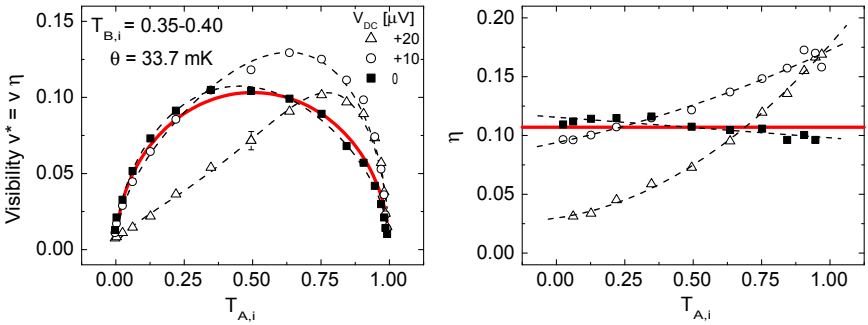

Figure 6.15: Corresponding measurements to the ones shown in Fig. 6.13, but with $T_{B,i} = 0.35 - 0.4$. The asymmetry of QPC A does *not* depend on the settings of QPC B.

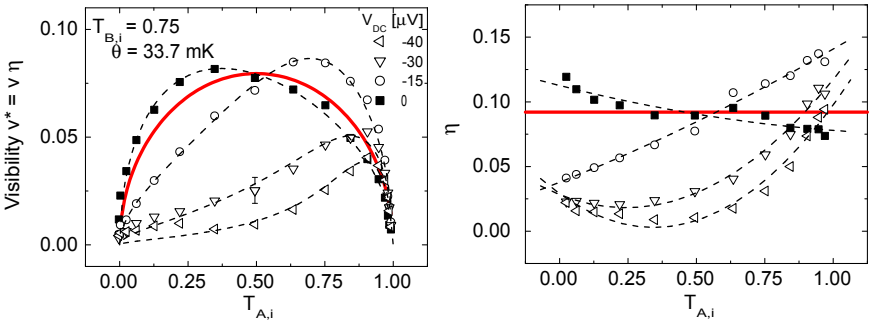

Figure 6.16: Corresponding measurements to the ones shown in Fig. 6.13, but with $T_{B,i} = 0.75$. The asymmetry of QPC A does *not* depend on the settings of QPC B.

k^--states have switched the side of the sample. In Fig. 6.2 the detector $D3$ and source $S1$ contact are now inverted. The DC bias is applied to $D3 = S3$ and the current leaving the interferometer is detected at $S1 = D1$. In both configurations the small inner contact $D4$ is held on ground potential.

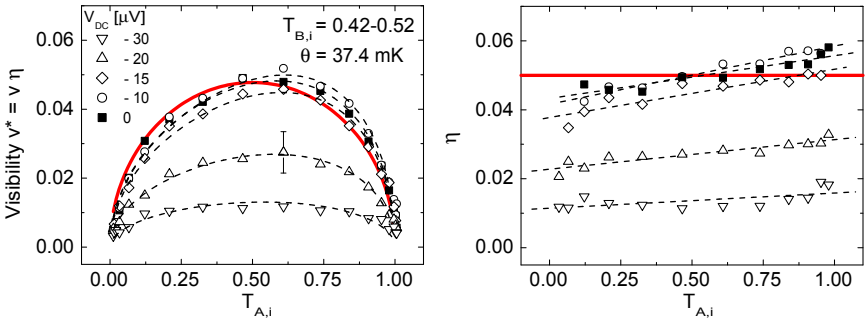

Figure 6.17: The same measurement as shown in Fig. 6.13 in reversed magnetic field. Formerly been the "first" beam splitter at +3.55 T with an *asymmetric* dependence of the visibility versus transmission, QPC A is now the "second" one at -3.55 T with an almost *symmetric* half-circle.

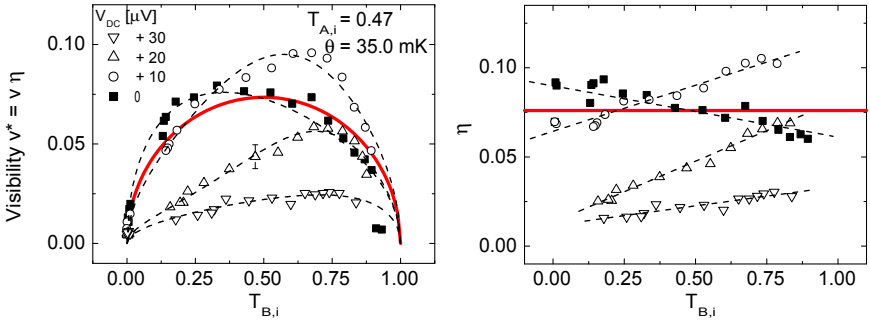

Figure 6.18: The same measurement as shown in Fig. 6.14 with reversed magnetic field. Formerly been the "second" beam splitter at +3.55 T with an *symmetric* dependence of the visibility versus transmission, QPC B is now the "first" one at -3.55 T with a deviation of the half-circle dependence.

In order to prevent confusion, the *labeling of the two beam splitters* QPC A and QPC B is *not changed* for the reverse magnetic field. In the previous measurements for $B = +3.55$ T, QPC A is the "first" one which determines

the occupation of the two paths, $T_{A,i}$, resp. $1 - T_{A,i}$. The "second" QPC B controls[8] the current that flows into the detectors $D3$ and $D4$, as given by Eqs. (6.4) and (6.5). In a reversed magnetic field, $B = -3.55\,\mathrm{T}$, the function of the QPC's is consequently changed. Now, QPC B determines the occupations of the two paths while QPC A has only an influence on the partition of the current to the two detectors.

In the previous measurements for $B = +3.55\,\mathrm{T}$ the two beam splitter behave differently. While variation of the "first" QPC A shows a deviation of the expected half-circle behavior (Fig. 6.3) for finite DC bias (Fig. 6.13), this is *not* the case for the "second" QPC B (Fig. 6.14). In a reversed magnetic field, the roles of the QPC's change and QPC B is now the "first" one while QPC A is the "second" one.

Figs. 6.17 and 6.18 represent the data of the same type of measurements of the visibility and intrinsic visibility as shown in Figs. 6.13 and 6.14 but in reversed magnetic field. As observed previously, a variation of the "first" QPC, now QPC B, results in a deviation from the expected half-circle structure while this is not the case for the second one, now A. We can thus conclude that this deviation is *not* a feature of a single QPC but an *intrinsic property of the interferometer*. Independent from the direction of the magnetic field, in both cases it is the "first" QPC (regarding the direction of transport in the edge states) that gives rise to an unexpected asymmetry in the dependence of the visibility on the QPC transmission at finite DC bias.

As it is the first QPC which determines the occupation of the two arms of the interferometer, one should consider the question if there could be an asymmetry in the two arms. At filling factor $\nu = 2$ where two spin-polarized edge states run in parallel, only the outer edge state is partitioned by the first QPC and recombined by the second one. The inner edge state, however, is pinched-off by both QPC's. Thus, in the upper arm the inner edge state is always fully occupied and on potential eV which is applied to source $S1$ while in the lower arm the inner edge state is empty and on the potential of the inner contact $S2/D4$ (see Fig. 6.2 and 6.5).

[8] Together with QPC A.

For non-zero DC bias the intrinsic visibility η increases when the QPC is changed from 1/2 to values close to 1. With a transmission close to 1 the outer edge state of the lower arm is fully populated. In case that the transmission is very low, a decrease of η is observed for non-zero DC bias. In this situation it is the outer edge state of the upper arm which is fully occupied. In other words: for almost both edge states in the upper arm completely occupied and both edge states in the lower arm completely empty, the visibility of the interferometer is lowest, while the visibility is maximal in the case that the outer and inner egde-states are unequally occupied.

6.4.3.2 Dependence of the Visibility on DC-Bias

By plotting the visibility v^* as function of DC bias for different QPC transmissions, we can point out in a more pronounced way the fact that the measured visibility v^* as well as the intrinsic visibility η increase for non-zero DC bias for values of an *almost open first QPC* (Fig. 6.19). In several publications the visibility v^* is measured against V_{DC} or V_{AC} for a transmission of the QPC's of 1/2 [13–16]. In this regime the measured visibility v^* is a measure of the intrinsic visibility η of the interferometer because $v = 4\sqrt{T_A T_B R_A R_B} = 1$ (see Eqs. 6.8 and 6.9), which is not the case for transmissions $\neq 1/2$. It is interesting to compare v^* and η as done in Fig. 6.19 where the second QPC B was held constant around $T_{B,i} \approx 0.5$ while the transmission of the first QPC A an the DC bias were varied. While the main features as the dip at zero DC bias or the side peaks around $30\,\mu$V remain, the curves are rescaled for η. As it can be seen in the lower left part of Fig. 6.19, the intrinsic visibility η at zero DC bias is independent of the QPC transmissions. When the DC bias is increased the intrinsic visibility rises for an open first QPC while it decreases for small transmissions.

6.5 Discussion

In this chapter an electronic Mach-Zehnder interferometer implemented with edge states in a 2DEG has been presented. The measurements have

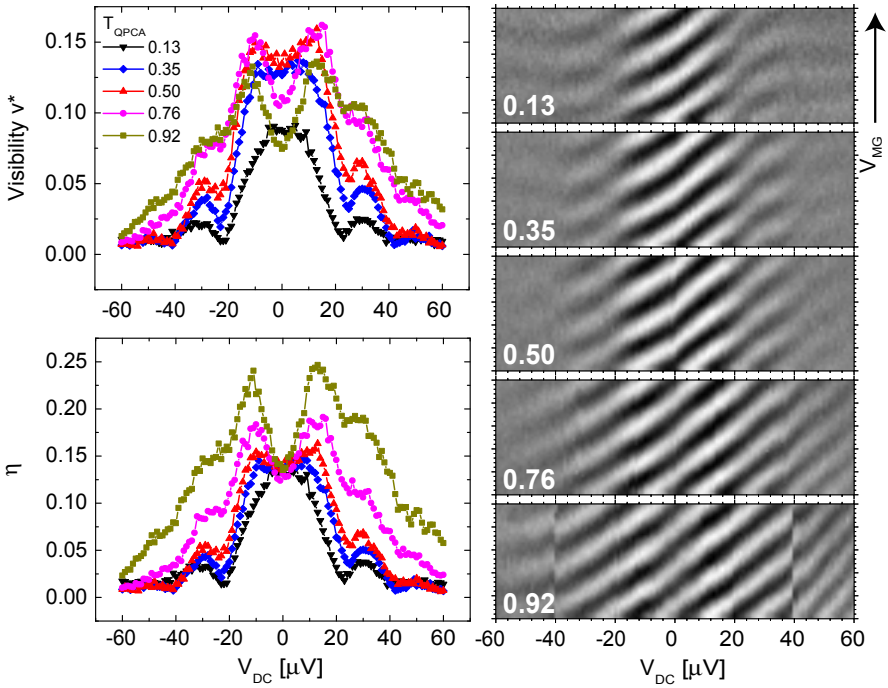

Figure 6.19: *Upper and lower left:* Measured visibility v^* and intrinsic visibility η as a function of DC bias for different transmissions of the first QPC A while the second QPC B was fixed to transmission $T_{B,i} \approx 0.5$. η at zero DC bias is independent of the QPC transmissions. *Right:* The measured differential transmission through the MZI as a function of V_{DC} for the corresponding transmissions of QPC A. The phase evolution of the oscillations is clearly visible.

been carried out at filling factor $\nu = 2$ and the measured visibility v^* has been studied for the full range of transmissions T of the QPC's A and B and different DC bias.

The visibility dependence on the QPC-transmission is different for the first A and second QPC B. For the second one, which has no influence on the occupation of the interferometer arms, the measured visibility v^* is proportional to $\sqrt{T(1-T)}$ which corresponds to a constant, transmission independent intrinsic visibility η (Eq. (6.9)). In contrast, the measured visibility

v^* as a function of the transmission of the first QPC shows a deviation from this half-circle dependence for DC biases higher than $V_{DC} = \pm 5\,\mu$V. This deviation is independent of the sign of the DC bias. The intrinsic visibility η is not constant as for QPC B, but decreased for small transmissions and increased for transmissions close to 1. Note that the first QPC controls the occupation of the outer edge state in both arms: For transmission 0 the upper arm is completely filled and its electro-chemical potential equals the one of source $S1$. The lower one is empty and on ground potential. For transmission 1 it is the other way round. In summary, the intrinsic visibility η is higher for different potentials between inner and outer edge-state compared to the case that the two edge states are on equal potentials.

The reason for such a behavior is not understood at the moment. In a model proposed in [78] for filling factor $\nu = 2$, time dependent fluctuations (noise) in the inner edge state decrease the visibility of the interferometer based on the outer edge states. These fluctuations are maximal for a half-filled inner edge state but zero for an empty or fully occupied inner edge state. In our case the inner edge states are always completely filled (upper arm) or empty (lower arm) and therefore noise-free. Hence, in this model they should not destroy the phase coherence at all.

The discussed behavior of the intrinsic visibility η can also be plotted differently, i. e. versus DC bias for different transmissions of the first QPC while the transmission of the second one is kept constant (Fig. 6.19). The intrinsic visibility as a function of DC bias reveals for small transmissions of the first QPC a lobe-type structure qualitatively similar to the ones reported in [14, 16], where the QPC's were always adjusted to transmission 1/2. By increasing the transmission of the first QPC above 1/2, like we did here, the intrinsic visibility at finite DC bias ($\pm 10 - 15\,\mu$V) rises above the value at zero DC bias.

The visibility of an electronic Mach-Zehnder interferometers is very sensitive to the surrounding environment. Provided they are understood in more detail and there is no "unexpected behavior" anymore, they will be nice sensor devices to probe the physics of edge states. In addition, they might be coupled in a controlled way to other phase coherent systems in order to study their decoherence.

Appendix A

Scattering Matrix for the Positive Cross Correlation Experiment presented in Chapter 5

In this appendix a derivation of the power spectral density for the case of inelastic scattering (Eq. 10 and finally Eq. 12 in Texier and Büttiker [10]) is given. It follows [10] but the calculations are carried out in detail.

The current at contact α can be written as $I_\alpha = (1/e)\int dE \sum_\beta G_{\alpha\beta} f_\beta + \delta I_\alpha$. δI_α is called the intrinsic part of the fluctuation, e. g. by partitioning at the point contacts. The mean current can be written with the help of the average distribution functions $\bar{f}_\beta$ as $\langle I_\alpha \rangle = (1/e)\int dE \sum_\beta G_{\alpha\beta}\bar{f}_\beta$ and the conductance as $G_{\alpha\beta} = (e^2/h)(N_\alpha \delta_{\alpha\beta} - \mathrm{Tr}\{s^\dagger_{\alpha\beta} s_{\alpha\beta}\})$. The assumption in [10] is that for the floating contact 4 the mean current $\langle I_4 \rangle$ as well as the fluctuating current ΔI_4 are zero. Hence we can write following equation:

$$I_4 = \underbrace{\langle I_4 \rangle}_{0} + \underbrace{\Delta I_4}_{0} = 0 = \underbrace{\frac{1}{e}\int dE \sum_\beta G_{4\beta} f_\beta + \delta I_4}_{I_4} = \underbrace{\frac{1}{e}\int dE \sum_\beta G_{4\beta}\bar{f}_\beta}_{\langle I_4 \rangle} + \underbrace{0}_{\Delta I_4}. \tag{A.1}$$

This leads immediately to

$$\delta I_4 = -\frac{1}{e}\int dE \sum_\beta G_{4\beta}(f_\beta - \bar{f}_\beta) = -\frac{1}{e}\int dE G_{44}(f_4 - \bar{f}_4) = -\frac{1}{e}(\mu_{44} - \bar{\mu_{44}}). \tag{A.2}$$

An analogue calculation leads to Eq. 8 of [10]:

$$\begin{aligned} \Delta I_\alpha = I_\alpha - \langle I_\alpha \rangle &= \frac{1}{e}\int dE \sum_\beta G_{\alpha\beta} f_\beta + \delta I_\alpha - \frac{1}{e}\int dE \sum_\beta G_{\alpha\beta}\bar{f}_\beta = \\ &= \delta I_\alpha - \frac{1}{e}\int dE \sum_\beta G_{\alpha\beta}(\bar{f}_\beta - f_\beta) = \delta I_\alpha - \frac{1}{e} G_{\alpha 4}(\bar{\mu_4} - \mu_4) = \\ &= \delta I_\alpha - \frac{G_{\alpha 4}}{G_{44}}\delta I_4. \end{aligned} \tag{A.3}$$

With the help of A.3 we now easily write down Eq. 10 of [10]:

$$\begin{aligned} S^{\text{in}}_{\alpha\beta} &= \langle \Delta I_\alpha \Delta I_\beta \rangle = \langle (\delta I_\alpha - \frac{G_{\alpha 4}}{G_{44}})(\delta I_\beta - \frac{G_{\beta 4}}{G_{44}}) \rangle = \\ &= \underbrace{\langle \delta I_\alpha \delta I_\beta \rangle}_{S_{\alpha\beta}} - \frac{G_{\alpha 4}}{G_{44}} \underbrace{\langle \delta I_\beta \delta I_4 \rangle}_{S_{\beta 4}} - \frac{G_{\beta 4}}{G_{44}} \underbrace{\langle \delta I_\alpha \delta I_4 \rangle}_{S_{\alpha 4}} + \frac{G_{\alpha 4} G_{\beta 4}}{G_{44}^2} \underbrace{\langle \delta I_4 \delta I_4 \rangle}_{S_{44}} \end{aligned} \tag{A.4}$$

For the calculation of the specific case of S^{in}_{23} we need the spectral noise powers S_{23}, S_{24}, S_{34} and S_{44} and the conductances G_{24}, G_{34} and G_{44}:

$$S^{\text{in}}_{23} = S_{23} - \frac{G_{24}}{G_{44}} S_{34} - \frac{G_{34}}{G_{44}} S_{24} + \frac{G_{24} G_{34}}{G_{44}^2} S_{44} \tag{A.5}$$

Hence we need the scattering matrix which connects the in and outgoing scattering states (the first index describes the terminal and the second one channel (i) or (ii):

$$\begin{pmatrix} b_{1i} \\ b_{1ii} \\ b_{2i} \\ b_{2ii} \\ b_{3i} \\ b_{3ii} \\ b_{4i} \\ b_{4ii} \end{pmatrix} = S \begin{pmatrix} a_{1i} \\ a_{1ii} \\ a_{2i} \\ a_{2ii} \\ a_{3i} \\ a_{3ii} \\ a_{4i} \\ a_{4ii} \end{pmatrix} \tag{A.6}$$

$$S = \begin{pmatrix} s_{11} & s_{12} & 0 & 0 \\ 0 & 0 & s_{23} & s_{24} \\ 0 & 0 & s_{33} & s_{34} \\ s_{41} & s_{42} & 0 & 0 \end{pmatrix} = \begin{pmatrix} r_{1i1i} & 0 & t_{2i1i} & 0 & 0 & 0 & 0 & 0 \\ 0 & r_{1ii1ii} & 0 & t_{2ii1ii} & 0 & 0 & 0 & 0 \\ 0 & 0 & 0 & 0 & t_{3i2i} & 0 & r_{4i2i} & 0 \\ 0 & 0 & 0 & 0 & 0 & t_{3i2ii} & 0 & r_{4ii2ii} \\ 0 & 0 & 0 & 0 & r'_{3i3i} & 0 & t'_{4i3i} & 0 \\ 0 & 0 & 0 & 0 & 0 & r'_{3ii3ii} & 0 & t'_{4ii3ii} \\ t'_{1i4i} & 0 & r'_{2i4i} & 0 & 0 & 0 & 0 & 0 \\ 0 & t'_{1ii4ii} & 0 & r'_{2ii4ii} & 0 & 0 & 0 & 0 \end{pmatrix} \tag{A.7}$$

this corresponds to the transmissions of the two point contacts A and B:

$$S = \begin{pmatrix} \sqrt{1-T_A^i} & 0 & \sqrt{T_A^i} & 0 & 0 & 0 & 0 & 0 \\ 0 & \sqrt{1-T_A^{ii}} & 0 & \sqrt{T_A^{ii}} & 0 & 0 & 0 & 0 \\ 0 & 0 & 0 & 0 & \sqrt{T_B^i} & 0 & \sqrt{1-T_B^i} & 0 \\ 0 & 0 & 0 & 0 & 0 & \sqrt{T_B^{ii}} & 0 & \sqrt{1-T_B^{ii}} \\ 0 & 0 & 0 & 0 & -i\sqrt{1-T_B^i} & 0 & i\sqrt{T_B^i} & 0 \\ 0 & 0 & 0 & 0 & 0 & -i\sqrt{1-T_B^{ii}} & 0 & i\sqrt{T_B^{ii}} \\ -i\sqrt{T_A^i} & 0 & i\sqrt{1-T_A^i} & 0 & 0 & 0 & 0 & 0 \\ 0 & -i\sqrt{T_A^{ii}} & 0 & i\sqrt{1-T_A^{ii}} & 0 & 0 & 0 & 0 \end{pmatrix} \tag{A.8}$$

Now we have to calculate the different noise powers. For S_{23} the only non-zero contributions comes from scattering matrix elements with $\gamma, \delta \in \{3, 4\}$:

$$\begin{aligned} S_{23} &= \frac{2e^2}{h} \sum_{\gamma \neq \delta} \int_0^{eV} dE \mathrm{Tr}[s^\dagger_{2\gamma} s_{2\delta} s^\dagger_{3\delta} s_{3\gamma}](f_\gamma(1-f_\delta) + f_\delta(1-f_\gamma)) = \\ &= \frac{2e^2}{h}(\mu_3 - \mu_4)\mathrm{Tr}\left(\begin{pmatrix} \sqrt{T_B^i} & 0 \\ 0 & \sqrt{T_B^{ii}} \end{pmatrix} \begin{pmatrix} \sqrt{1-T_B^i} & 0 \\ 0 & \sqrt{1-T_B^{ii}} \end{pmatrix} \begin{pmatrix} -i\sqrt{T_B^i} & 0 \\ 0 & -i\sqrt{T_B^{ii}} \end{pmatrix} \begin{pmatrix} -i\sqrt{1-T_B^i} & 0 \\ 0 & -i\sqrt{1-T_B^{ii}} \end{pmatrix} \right) = \\ &= \frac{2e^2}{h}(-\sum_n (T_B^n(1-T_B^n)))(|\mu_3 - \mu_4|) = \frac{-2e^2}{h}(T_B^i(1-T_B^i) + T_B^{ii}(1-T_B^{ii})) \cdot \frac{T_A^i + T_A^{ii}}{2} eV. \end{aligned} \tag{A.9}$$

For S_{24} and S_{34} we get zero while for S_{44} we get in an similar calculation where the only non zero scattering matrix elements are $\gamma, \delta \in \{1, 2\}$:

$$S_{44} = \frac{2e^2}{h}(\sum_n (T_A^n(1 - T_A^n)))(|\mu_1 - \mu_2|) = \frac{2e^2}{h}(\sum_n (T_A^n(1 - T_A^n)))(eV). \tag{A.10}$$

For the conductances we get

$$G_{24} = \frac{e^2}{h}(N_2\delta_{24} - \mathrm{Tr}\{s_{24}^\dagger s_{24}\}) = \frac{e^2}{h}((1 - T_B^i) + (1 - T_B^{ii})). \tag{A.11}$$

A similar calculation gives $G_{34} = (e^2/h)(T_B^i + T_B^{ii})$ and $G_{44} = 2e^2/h$. Combining these results in Eq. A.5, we get:

$$\begin{aligned} S_{23}^{\mathrm{in}} &= -\frac{e^2}{h}\,|eV|\,((T_B^i(1 - T_B^i) + T_B^{ii}(1 - T_B^{ii}))(T_A^i + T_A^{ii}) + \\ &\quad -\frac{1}{2}((1 - T_B^i) + (1 - T_B^{ii}))(T_B^i + T_B^{ii})(T_A^i(1 - T_A^i) + T_A^{ii}(1 - T_A^{ii}))) \end{aligned} \tag{A.12}$$

With $T_A^i = T_B^i = 1$ we finally get Eq. 12 in [10]:

$$S_{23}^{\mathrm{in}} = -\frac{e^2}{h}\frac{1 - T_B^{ii}}{2}\left(2T_B^{ii}(1 + T_A^{ii}) - (1 + T_B^{ii})T_A^{ii}(1 - T_A^{ii})\right) \tag{A.13}$$

Appendix B

Recipes for Sample Preparation

This chapter is a collection of short recipes used for sample preparation.

B.1 Electron Beam Lithography

B.1.1 Hard- and Software

- Hardware: LEO Supra 35 from LEO Elektronenmikroskopie GmbH, Germany
- Software: Elphy Plus from Raith GmbH, Germany

B.1.2 Resists

- PMMA 950 K, AR-P671.09 from Allresist GmbH, Germany
- PMMA-MA, AR-P619.08 from Allresist GmbH, Germany

B.1.3 Resist Preparation

- PMMA 950 K: Diluting with chlorbenzene in order to decrease the resist thickness. Starting with a ratio of 1:1. Increasing the amount of chlorbenzene until wanted resist thickness reached
- PMMA-MA: No dilution

B.1.4 Spinning and Bake-out Single Layer

- Fixing sample on spinner
- Applying small amount of PMMA 950 K
- Starting spinning process. Parameter: Ramp: 4 s; Speed: 4000 rpm/s; Time: 40 s
- Bake-out in oven: 30 min at 175 °C

B.1.5 Spinning and Bake-out Double Layer

- Fixing sample on spinner
- Applying small amount of PMMA 950 K
- Starting spinning process. Parameter: Ramp: 4 s; Speed: 4000 rpm/s; Time: 40 s
- Bake-out in oven: 60 min at 175 °C
- Fixing sample on spinner
- Applying small amount of PMMA-MA
- Starting spinning process. Parameter: Ramp: 8 s; Speed: 8000 rpm/s; Time: 40 s
- Bake-out in oven: 60 min at 175 °C

B.1.6 Exposure

- Exposure doses for PMMA thickness 600 nm
  - Magnification M30; Writefield WF 2000 μm; Area Step Size: 160 nm; Dose: 350 μC/cm^2
  - M240; WF 250 μm; ASS: 20 nm; Dose: 250 μC/cm^2
  - M600; WF 100 μm; ASS: 20 nm; Dose: 250 μC/cm^2
- Exposure doses for PMMA thickness 200 nm
  - M30; WF 2000 μm; ASS: 160 nm; Dose: 250 μC/cm^2
  - M240; WF 250 μm; ASS: 20 nm; Dose: 160 μC/cm^2
  - M600; WF 100 μm; ASS: 20 nm; Dose: 160 μC/cm^2

B.1.7 Development

- Developer: Mixture of *4-Methyl-2-pentanone (MiBK)* and *2-propanol / isopropanol (IPA)* in a ratio of 1 : 3 (plus 1.4% of *2-butanone/ethyl-methylketone (MEK)*)
- Development time: 45 - 120 s
- Stopping Development: *Isopropanol* 30 s

B.1.8 Lift-Off

- Lift-Off in hot acetone (50 °C)
- If necessary: Smoothly flushing with a syringe.

B.2 Wet Etching

- Sample Cleaning: 3 h at 70 °C in Microposit Remover 1165 from Shipley, USA
- Rinsing in Ethanol 30 s
- Rinsing with DI-water 30 s
- Application of resist PMMA 200 nm/ Electron beam lithography / Developing Resist
- Etching with teflon tweezers in $H_2SO_4 : H_2O_2 : H_2O = 3 : 1 : 100$
- Etching rate is very dependent on temperature; From around 100 nm/min at 32 °C to around 115 nm/min at 33.5 °C.
- Etching rates are not that precise. A residual layer of PMMA or different etching rate from the cap layer (GaAs) and the donor layer (GaAlAs) might influence the result.

B.3 Reactive Ion Etching

This values are "machine-dependent". Make your own test. We used a Plasmalab 80 Plus from Oxford Instruments, UK.

- Base pressure before starting process: $3.0 \cdot 10^{-5}$ mbar
- Process pressure for plasma: 300 mTorr
- RF power 50 W
- Valve position for O_2: 16 %
- Etching rate for PMMA: 1 nm/s

B.4 Gates

- Application of PMMA 600 nm/ Electron beam lithography / Developing Resist
- Reactive Ion Etching (oxygen-plasma) to remove residual PMMA: 15 nm
- Metalization in Balzers evaporator
  - Sample holder cooled down to 0 °C by liquid nitrogen
  - Evaporation of titanium 40 Å/ gold 600 Å
- Lift-Off

B.5 Ohmic Contacts

- Wafer-Cleaning
  - approx. 5 min ultrasonic in acetone
  - rinsing with acetone
  - approx. 5 min ultrasonic in isopropanol
  - rinsing with isopropanol
- Application of PMMA 600 nm/ Electron beam lithography / Developing Resist
- Reactive Ion Etching (oxygen-plasma) to remove residual PMMA: 30 nm
- Cleaning with strong alkaline solvent (SemicoClean) 2 min / DI-Water 5 s / HCl-Dip 5 s / DI-Water 5 s
- Metalization in Balzers evaporator
  - Sample holder cooled down to 0 °C by liquid nitrogen
  - Evaporation Au/Ge/Ni
    - Cross Correlation Experiment (Ch. 5): Recipe M1
    - MZ-interferometer Experiment (Ch. 6): Recipe M3
- Lift-Off
- Annealing
  - Cross Correlation Experiment (Ch. 5): Recipe A1
  - MZ-interferometer Experiment (Ch. 6): Recipe A3

B.5.1 Metalization Recipes

Recipe M1		Recipe M2		Recipe M3	
Ni	60 Å	Ni	60 Å	Au	1460 Å
Au	500 Å	Ge	400 Å	Ge	720 Å
Ge	200 Å	Au	600 Å	Ni	545 Å
Au	600 Å	Ni	200 Å		
Ni	300 Å	Au	500 Å		

Table B.1: Different metalization recipes mentioned in Sec. 3. The materials are evaporated from top to bottom.

B.5.2 Annealing Recipes

Recipe A1		Recipe A2		Recipe A3	
300 s	120 °C	60 s	120 °C	120 s	370 °C
120 s	410 °C	60 s	400-480 °C	50 s	440 °C
30 s	490 °C			2 s	100 °C

Table B.2: Different annealing recipes mentioned in Sec. 3.

B.6 Free-Standing Bridges

- Application of double layer PMMA 200 nm – PMMA-MA (see B.1.5)
- Electron Beam Lithography: Exposing: M600; ASS 20 nm; Dose: 120 μC/cm^2 (Pillar) and 40 μC/cm^2 (Bridge)
- Metalization in Balzers evaporator
  - Sample holder cooled down to 0 °C by liquid nitrogen
  - Evaporation Titanium 25 Å; Gold 3500 Å
- Lift-Off

Publications

- S. Lindemann, T. Ihn, E. Bieri, T. Heinzel, K. Ensslin, G. Hackenbroich, K. Maranowski and A. C. Gossard, *Bouncing states in quantum dots*. In: Phys. Rev. B, **66**, 161312 (2002)
- A. Dorn, E. Bieri, T. Ihn, K. Ensslin, D. Driscoll and A.C. Gossard, *AFM-defned antidot lattices with top- and back-gate tunability*. In: Physica E, **22**, 749 (2004)
- A. Dorn, E. Bieri, T. Ihn, K. Ensslin, D. Driscoll and A.C. Gossard, *Interplay between the periodic potential modulation and random background scatterers in an antidot lattice*. In: Phys. Rev. B, **71**, 035343 (2005)
- S. Oberholzer, E. Bieri, C. Schönenberger, M. Giovannini and J. Faist, *Positive Cross Correlations in a Normal-Conducting Fermionic Beam Splitter*. In: Phys. Rev. Lett., **96**, 046804 (2006)
- E. Bieri, M. Weiss, O. Göktas, M. Hauser S. Oberholzer and C. Schönenberger, *Unexpected finite-bias visibility dependence in an electronic Mach Zehnder interferometer*, submitted (2008), *cond-mat/0812.2612v1*

Talks and Poster Contributions

- S. Oberholzer, E. Bieri, M. Giovannini, J. Faist, and Ch. Schönenberger, *Positive Cross Correlations in a Normal-Conducting Fermionic Beam Splitter*, Poster at the International Conference of Nanoscience and Technology (ICN+T) 2006, Basel, Switzerland, July 31 - August 4, 2006
- E. Bieri, S. Oberholzer and C. Schönenberger, *Noise and Interference Experiments with Edge States*, Talk at the Annual Meeting of the Swiss Physical Society, Zürich, February 20-21, 2007,
- E. Bieri, M. Weiss, O. Göktas, M. Hauser, S. Csonka, S. Oberholzer and C. Schönenberger, *Interference Experiments with Edge States: An Electronic Mach-Zehnder Interferometer*, Invited Talk at the Max-Planck Institut für Festkörperforschung, Stuttgart, November 19, 2007
- E. Bieri, M. Weiss, O. Göktas, M. Hauser, S. Csonka, S. Oberholzer and C. Schönenberger, *Interference Experiments with Edge States: An Electronic Mach-Zehnder Interferometer*, Invited Talk in the Seminar of the Departement de Physique Theorique at University of Geneva, Geneva, November 27, 2007

Folgenden Dozentinnen und Dozenten verdanke ich meine wissenschaftliche Ausbildung:

R. Allenspach, J. Bernasconi, K. Ensslin, G. M. Graf, P. Günter, W. Hunziker, H. Knörrer, J. Marti, H.-R. Ott, F. Pauss, T. M. Rice, K. Simon, E. Trubowitz, G. Wüstholz, E. Zehnder

Acknowledgment

Finally I would like to thank all the people who were supporting me in any kind and thus making it possible to realize this thesis.

First of all I would like to thank very much Prof. Christian Schönenberger for giving me the opportunity to receive a PhD in his group. I could learn a lot from his broad knowledge in and his motivation for physics. Also many thanks to Prof. J. Faist and Prof. Ch. Strunk for refereeing my thesis.

For the support with 2DEG-materials, I would like to thank Dr. Marcella Giovannini from the group of Prof. J. Faist (used in the experiments in Ch. 5) and Dr. Jürgen Weis from MPI Stuttgart (used in the experiments in Ch. 6). Many thanks also to Oktay Göktas from the group of Dr. J. Weis for fruitful discussions in realizing delicate structures in electron beam lithography.

From my group I have to thank Stefan Oberholzer for introducing me into E-beam lithography. Many thanks to Markus Weiss who ensured with his cryogenic knowledge for a working dilution refrigerator and to Szabolcs Csonka for the interesting discussions in analyzing the data.

Many thanks as well to Prof. Dominik Zumbühl for sharing his knowledge in sample preparation and cryogenic physics in helpful and interesting discussions.

Further I would like to thank all the group members in changing formation during the years for the nice working atmosphere and activities beside physics, Alexander Eichler, Andreas Kleine, Bakir Babic, Bong-Ryoul Choi, Christian Hoffmann, Dino Keller, Gunnar Gunnarsson, Jelena Trbovic, Jianhui Liao, Jürg Furer, Lucia Grüter, Matthias Gräber, Michel Calame, Roman Huber, Sangeeta Sahoo, Sense Jan van der Molen, Song-Mei Wu, Teresa Gonzalez, Takis Kontos, Zheng-Ming Wu and also Sarah Heizmann and Charulata Barge.

Also many thanks to the secretaries Barbara Kammermann and Astrid Kalt with their warm and competent handling of mostly a little bit stressed people, to the mechanical workshop, espescially to Sascha Martin, Werner Roth and Dominik Sifrig, and to the electronic workshop with Michael Steinacher, Werner Erni, Bernd Heimann.

Finally, I would especially like to thank Sanja for her patience and support over all the years.

Bibliography

[1] R. Hanbury Brown and R. Q. Twiss, Nature **177**, 27 (1956).

[2] R. Hanbury Brown and R. Q. Twiss, Nature **178**, 1046 (1956).

[3] R. J. Glauber, Phys. Rev. Lett. **10**, 84 (1963).

[4] R. J. Glauber, Phys. Rev. **130**, 2529 (1963).

[5] R. J. Glauber, Phys. Rev. **131**, 2766 (1963).

[6] M. Henny et al., Science **284**, 296 (1999).

[7] W. D. Oliver, J. Kim, R. C. Liu, and Y. Yamamoto, Science **284**, 299 (1999).

[8] S. Oberholzer et al., Physica E **6**, 314 (2000).

[9] H. Kiesel, A. Renz, and F. Hasselbach, Nature **418**, 392 (2002).

[10] C. Texier and M. Büttiker, Phys. Rev. B **62**, 7454 (2000).

[11] S. Oberholzer, E. Bieri, C. Schönenberger, M. Giovannini, and J. Faist, Phys. Rev. Lett. **96**, 046804 (2006).

[12] P. Samuelsson, E. V. Sukhorukov, and M. Büttiker, Phys. Rev. Lett. **92**, 026805 (2004).

[13] Y. Ji et al., Nature **422**, 415 (2003).

[14] I. Neder, M. Heiblum, Y. Levinson, D. Mahalu, and V. Umansky, Phys. Rev. Lett. **96**, 016804 (2006).

[15] L. V. Litvin, H.-P. Tranitz, W. Wegscheider, and C. Strunk, Phys. Rev. B **75**, 033315 (2007).

[16] P. Roulleau et al., http://arxiv.org/abs/0704.0746v1, 2007.

[17] M. A. Hermann and H. Sitter, *Molecular Beam Epitaxy*, Springer, Berlin, 1989.

[18] R. Dingle, H. L. Störmer, A. C. Gossard, and W. Wiegmann, Appl. Phys. Lett. **33**, 665 (1978).

[19] G. L. Snider, I.-H. Tan, and E. L. Hu, J. Appl. Phys. **68**, 2849 (1990).

[20] Poisson-Schrödinger solver: `http://www.nd.edu/~gsnider/`.

[21] C. W. J. Beenakker and H. van Houten, Solid State Physics **44**, 1 (1991).

[22] S. Datta, *Electronic Transport in Mesoscopic Systems*, Cambridge University Press, Cambridge UK, 1st edition, 1995.

[23] E. Hall, American Journal of Mathematics **2**, 287 (1879).

[24] Y. Aharonov and D. Bohm, Phys. Rev. **115**, 485 (1959).

[25] S. Kogan, *Electronic noise and fluctuations in solids*, Cambridge University Press, Cambridge UK, 1st edition, 1996.

[26] W. Schottky, Ann. Phys. (Leipzig) **57**, 541 (1918).

[27] M. Büttiker, Phys. Rev. Lett. **65**, 2901 (1990).

[28] M. Büttiker, Phys. Rev. B **46**, 12485 (1992).

[29] J. B. Johnson, Phys. Rev. **29**, 367 (1927).

[30] H. Nyquist, Phys. Rev. **29**, 614 (1927).

[31] J. B. Johnson, Phys. Rev. **32**, 97 (1928).

[32] H. Nyquist, Phys. Rev. **32**, 110 (1928).

[33] X. Jehl, P. Payet-Burin, C. Baraduc, R. Calemczuk, and M. Sanquer, Phys. Rev. Lett. **83**, 1660 (1999).

[34] R. de Picciotto et al., Nature **389**, 162 (1997).

[35] L. Saminadayar, D. C. Glattli, Y. Jin, and B. Etienne, Phys. Rev. Lett. **79**, 2526 (1997).

[36] R. A. Jalabert, J. L. Pichard, and C. W. J. Beenakker, Europhys. Lett. **27**, 255 (1994).

[37] C. W. J. Beenakker and M. Büttiker, Phys. Rev. B **46**, 1889 (1992).

[38] S. Oberholzer et al., Phys. Rev. Lett. **86**, 2114 (2001).

[39] A. H. Steinbach, J. M. Martinis, and M. H. Devoret, Phys. Rev. Lett. **76**, 2778 (1996).

[40] R. J. Schoelkopf, P. J. Burke, A. A. Kozhevnikov, D. E. Prober, and M. J. Rooks, Phys. Rev. Lett. **78**, 3370 (1997).

[41] M. Henny, S. Oberholzer, C. Strunk, and C. Schönenberger, Phys. Rev. B **59**, 2871 (1999).

[42] H. Ibach and H. Lüth, *Festkörperphysik*, Springer, Berlin Heidelberg, 5th edition, 1999.

[43] D. C. Look, *Electrical Characterisation of GaAs Materials and Devices*, John Wiley & Sons, Chichester UK, 1988.

[44] R. P. Taylor et al., J. Appl. Phys. **76**, 7966 (1994).

[45] F. Pobell, *Matter and Methods at Low Temperatures*, Springer-Verlag, Berlin Heidelberg New York, 2nd edition, 1996.

[46] E. Schrödinger, Die Naturwissenschaften **23**, 807 (1935).

[47] E. Schrödinger, Die Naturwissenschaften **23**, 823 (1935).

[48] E. Schrödinger, Die Naturwissenschaften **23**, 844 (1935).

[49] A. Stern, Y. Aharonov, and Y. Imry, Phys. Rev. A **41**, 3436 (1990).

[50] G. Baym, Acta Physica Polonica B **29**, 1839 (1998).

[51] E. Brannen and H. I. S. Ferguson, Nature **178**, 481 (1956).

[52] R. Feynman, *Theory of Fundamental Processes*, W.A. Benjamin, Inc., New York, 1961.

[53] T. Martin and R. Landauer, Phys. Rev. B **45**, 1742 (1992).

[54] T. Jeltes et al., Nature **445**, 402 (2007).

[55] I. Neder et al., Nature **448**, 333 (2007).

[56] E. Bieri et al., submitted to PRB (2008).

[57] M. Büttiker, Science **313**, 1587 (2006).

[58] Y. Chen and R. A. Webb, Phys. Rev. Lett. **97**, 066604 (2006).

[59] D. T. McClure et al., Phys. Rev. Lett. **98**, 056801 (2007).

[60] O. Sauret and D. Feinberg, Phys. Rev. Lett. **92**, 106601 (2004).

[61] A. Cottet, W. Belzig, and C. Bruder, Phys. Rev. Lett. **92**, 206801 (2004).

[62] B. J. van Wees et al., Phys. Rev. Lett **62**, 1181 (1989).

[63] B. W. Alphenaar, P. L. McEuen, R. G. Wheeler, and R. N. Sacks, Phys. Rev. Lett. **64**, 677 (1990).

[64] L. Zehnder, Zeitschrift für Instrumentenkunde **11**, 275 (1891).

[65] L. Mach, Zeitschrift für Instrumentenkunde **12**, 89 (1892).

[66] J. Jamin, J. C. R. Acad. Sci. Paris. S. **482** (1856).

[67] S. Komiyama, H. Hirai, S. Sasa, and S. Hiyamizu, Phys. Rev. B **40**, 12566 (1989).

[68] V.-W. Chung, P. Samuelsson, and M. Büttiker, Phys. Rev. B **72**, 125320 (2005).

[69] M. Büttiker, Phys. Rev. B **33**, 3020 (1986).

[70] M. Büttiker, IBM J. Res. Dev. **32**, 63 (1988).

[71] M. de Jong and C. Beenakker, Physica A **230**, 219 (1996).

[72] P. Roulleau et al., http://arxiv.org/abs/0704.0746v2, 2007.

[73] I. P. Levkivskyi and E. V. Sukhorukov, Phys. Rev. B **78**, 045322 (2008).

[74] P. Roulleau et al., Phys. Rev. Lett. **100**, 126802 (2008).

[75] G. Seelig and M. Büttiker, Phys. Rev. B **64**, 245313 (2001).

[76] I. Neder and E. Ginossar, Phys. Rev. Lett. **100**, 196806 (2008).

[77] S.-C. Youn, H.-W. Lee, and H.-S. Sim, Phys. Rev. Lett. **100**, 196807 (2008).

[78] I. Neder, F. Marquardt, M. Heiblum, D. Mahalu, and V. Umansky, Nature Physics **3**, 534 (2007).